ESTIMATING UNSATURATED FLOW PROPERTIES IN COARSE CONGLOMERATIC SEDIMENT

by

Michael James Thoma, Jr.

A dissertation

submitted in partial fulfillment

of the requirements for the degree of

Doctor of Philosophy in Geosciences

Boise State University

May 2014

BOISE STATE UNIVERSITY GRADUATE COLLEGE

DEFENSE COMMITTEE AND FINAL READING APPROVALS

of the dissertation submitted by

Michael James Thoma, Jr.

Dissertation Title: Estimating Unsaturated Flow Properties in Coarse Conglomeratic Sediment

Date of Final Oral Examination: 21 November 2013

The following individuals read and discussed the dissertation submitted by student Michael James Thoma Jr., and they evaluated his presentation and response to questions during the final oral examination. They found that the student passed the final oral examination.

Warren Barrash, Ph.D.	Chair, Supervisory Committee
John H. Bradford, Ph.D.	Member, Supervisory Committee
Michael M. Cardiff, Ph.D.	Member, Supervisory Committee
James P. McNamara, Ph.D.	Member, Supervisory Committee
Jodi Mead, Ph.D.	Member, Supervisory Committee
T. P. A. Ferre, Ph.D.	External Examiner

The final reading approval of the dissertation was granted by Warren Barrash, Ph.D., Chair of the Supervisory Committee. The dissertation was approved for the Graduate College by John R. Pelton, Ph.D., Dean of the Graduate College.

DEDICATION

This work is dedicated to my family and especially my parents, who never pushed me to do anything but always let me go my own way. They subtly instilled in me the confidence to know that whatever I decided to do, I would figure it out, I would be okay, and I always had their support. This is also dedicated to Noel, who has been by my side through the entire experience and has been nothing but supportive and understanding. I could not, and would not, have done this without her. She is my Aloha! I also thank Noel's family, who have become a family to me.

ACKNOWLEDGMENTS

I would like to thank the entire Geosciences Department at Boise State University, including several former members, for their support through my Masters Degree and Doctorate Program. Special thanks to my advisor Dr. Warren Barrash, my committee members Dr. John Bradford, Dr. Jim McNamara, Dr. Jodi Mead, and Dr. Michael Cardiff, as well as the external reviewer Dr. Ty Ferre. I would also like to especially thank Brady Johnson, Dr. Bwalya Malama, Dr. Molly Gribb, and Dr. Kerry Keen for their contribution to my professional and personal development. Also, a special thanks to Liz Johanson, Terry Lobb, Peggy Medley, Tracy Anderson, and Lisa Cox for all their hard work; nothing could have gotten done without them. Finally, to my friend Perm, a mild thanks. Hydrology would not have been as fun without him.

Funding for this work was provided by the U.S. Army RDECOM ARL Army Research Office under grant W911NF-09-1-0534 and the Boise State University Research Initiative and Graduate College. I would also like to thank Brady Johnson, Josh Ekhoff, Pam Aishlin, and Andreas Meyer for help during the experiment and, and Dr. Joel Hubbell of the Idaho National Laboratory and Jerry Noe of Electronic Engineering Innovations for assistance with design modifications, tuning, and installation of Advanced Tensiometers. Any reference to specific equipment types or manufacturers is for information purposes and does not represent a product endorsement or recommendation.

ABSTRACT

Our ability to model and predict unsaturated hydrologic processes in coarse, conglomeratic material is limited by the unconsolidated nature of these materials, the large grain sizes present (often gravel to cobble size), and the scale of heterogeneity that is typical of coarse, conglomeratic sediment (both within single layers at the grain-size scale and between interbedded lenses). Additionally, the nature of flow and specifically the effects that large cobbles have on infiltration and soil moisture (θ [-]) – tension (ψ [L]) – hydraulic conductivity (K [L t^{-1}]) relationships are not well understood for conglomeratic sediment. In this dissertation I address the lack of knowledge of unsaturated flow in coarse, conglomeratic sediment by determining if functional θ-ψ-K relationships, specifically van Genuchten-Mualem (VGM) relationships, developed to predict unsaturated flow in relatively fine-grained sediment can be directly applied to coarse, conglomeratic sediment. I also provide insight into the effects that cobbles have on flow and moisture content under infiltration conditions.

In the summer of 2011 a field-scale infiltration test was conducted at the Boise Hydrogeophysical Research Site, an alluvial gravel bar composed of coarse, conglomeratic sediment with interbedded fine-coarse sand lenses and minimal silt and clay. The purposes of this test were to investigate infiltration processes in conglomeratic sediment, determine if functional ψ-θ-K relationships could be applied to infiltration in coarse, conglomeratic sediment and, if so, estimate parameter values for the VGM

functions. Vertically and laterally distributed $\psi(t)$ and $\theta(t)$ measurements were made within the infiltration volume, and geophysical data and core samples were used to determine material structure and distribution for model development.

A four-material, 1D layered model was used with a Metropolis-Hastings search to fit partial $\psi(t)$ and $\theta(t)$ data and determine if VGM relationships were appropriate for unsaturated flow in coarse, conglomeratic sediment. The 1D model accurately fit the observed data for most of the system, implying that VGM relationships were applicable, and predicted low uncertainty in $\theta(\psi)$ and $K(\psi)$ curves for three of the four different materials but high uncertainty was observed in individual parameter values ($\sigma/\mu > 50$ %). High uncertainty was attributed to the inability of the model to incorporate lateral heterogeneity and the associated exclusion of the full $\theta(t)$ data. A four-material, 2D model was then constructed to incorporate variations in material thickness and to fit all $\psi(t)$ and $\theta(t)$ data. Direct-search optimization showed that fitting $\theta(t)$ and $\psi(t)$ data simultaneously was not possible due to additional, lateral heterogeneity within one of the material layers (which was evident from $K(\psi)$ curves) and a five-material, 2D model was constructed. Direct-search optimization was used to accurately fit the full $\theta(t)$ and $\psi(t)$ data sets and Latin-hypercube Sampling was used to estimate parameter uncertainty. Final results showed much less uncertainty in parameter values ($\sigma/\mu < 15$ %) with a reduction of individual parameter uncertainty up to 36% compared to the 1D model.

A method was also developed to use reflection travel-time from time-lapse ground-penetrating radar (GPR) profiles to estimate changes in θ in the vadose zone. The method was applied to the infiltration test data but failed to accurately reproduce the observed travel-time data, which was attributed to uncertainty in picking GPR reflections.

Results from both the 1D and 2D models show that unsaturated flow relationships developed for agricultural soils (e.g., the VGM models) can be used to predict flow and moisture distribution in coarse, conglomeratic sediment. This implies that cobbles do not have a significant effect at low-saturation flow rates, at least in sediment where the inter-cobble material is sand with minimal silt or clay. In this regard, the sustained high infiltration rate of the field experiment was conducted through the full 1.7 m thickness of the vadose zone at relatively low moisture contents (θ < 10 % in conglomeratic sediment layers). This indicates limited obstruction by cobbles and a very high capacity for infiltration in these types of materials under natural conditions.

TABLE OF CONTENTS

LIST OF FIGURES

LIST OF TABLES

LIST OF ABBREVIATIONS

AT	Advanced Tensiometer
BHRS	Boise Hydrogeophysical Research Site
bmp	Below Measuring Point
bls	Below Land Surface
BoR	Bureau of Reclamation
CRIM	Complex Refractive Index Method
DBMS	Database Management System
DS	Direct Search
DSm	Direct Sampling Method
DSr	Direct Search Method
ET	Evapotranspiration
GPR	Ground Penetrating Radar
ID	Inside Diameter
LHS	Latin-hypercube Sampling
MCMC	Markov Chain Monte Carlo
MDT	Mountain Daylight Time
MH	Metropolis-Hastings
REV	Representative Elementary Volume
VGM	van Genuchten-Mualem

CHAPTER 1: INTRODUCTION

Uncertainty in predicting unsaturated flow in coarse, conglomeratic sediment stems from a lack of understanding of the fundamental relationships between physical states and properties that control flow, specifically: soil moisture (θ), soil tension (ψ), and hydraulic conductivity (K). Functional relationships between θ, ψ, and K have been developed and extensively applied to relatively fine-grained sediment (particle diameter (d) < 2 mm) but have seldom been applied to coarse (d > 2 mm), conglomeratic sediment and have yet to be applied to in situ, coarse, conglomeratic sediment with natural, heterogeneous structure. This dissertation focuses on 1) determining if θ-ψ-K relationships developed for fine-grained sediment can be used to predict unsaturated flow in coarse, conglomeratic sediment in situ and 2) estimating parameters representative of these sediments. In this introductory chapter, I provide a background of unsaturated flow in the vadose zone and briefly address the current level of knowledge of unsaturated flow in conglomeratic sediment. I also provide a preview of the following chapters.

1.1 The Vadose Zone

The vadose zone describes the geologic media between the land surface and the water table (*Selker et al.* 1999). Its thickness depends on the depth of the water table and can range from being non-existent, where the water table is at the land surface, to hundreds of meters in areas that receive little rainfall (e.g., arid or semi-arid regions) or have high relief (e.g., mountainous terrain). The vadose zone can be composed of

consolidated rock, sediment, or soil, and the soil itself can possess varying levels of soil development (pedogenesis). The vadose zone is distinct from the saturated zone (i.e., zone beneath the water table) by having its pore space only partially saturated for most of the time. The partial saturation leads to one of the main state variables of the vadose zone: moisture content (θ [-]). Moisture content can be as low as zero but under natural conditions is typically limited to residual moisture content (θ_R) which accounts for water bonded to soil grains and trapped in isolated pores. When the soil is completely saturated it is referred to as saturated moisture content (θ_S), which is approximately equal to the sediment porosity (ϕ).

The vadose zone is the most extensive link between the atmosphere and the saturated zone. It is an essential part of both the natural hydrologic cycle (e.g., infiltration from precipitation) as well as the human-altered hydrologic cycle (e.g., irrigation and artificial recharge). Precipitation or irrigation on the land surface can take several paths; it can be evaporated back into the atmosphere or move as overland flow, but the majority infiltrates into the vadose zone (*Dingman* 2002). Once in the vadose zone, soil water can percolate through the full thickness of the vadose zone and become incorporated into the saturated zone (groundwater), be extracted through plant roots, or move laterally. Any surface contaminants that are dissolved in the water when it infiltrates (e.g., agricultural fertilizers, pesticides, etc.) have the potential to reach the groundwater and contaminate drinking water aquifers, or could seriously disrupt the soil ecosystem. While within the vadose zone, contaminants have the potential to become adsorbed onto soil grains, thereby becoming relatively immobile, or can be decomposed by biological activity and reduced to safe concentrations. Knowledge of the vadose zone, and particularly flow

through it, is thus essential to the overall health of the soil as well as protecting groundwater resources.

The vadose zone also plays an essential part in the routing of precipitation to streams and rivers. In montane environments, such as the western United States, winter precipitation is stored as snowpack at higher elevations. In the spring when the snowpack melts, sometimes rapidly, much of the water flows through the vadose zone or saturated zone (via the vadose zone) before recharging streams (*Smith et al.* 2011). The flow paths though the vadose zone help dampen spring flooding in montane streams and provide a source of water for vegetation. Vadose zone properties control the rate of infiltration and soil water flow and are essential components of flood forecasting models (*McNamara et al.* 2005). A better understanding of unsaturated flow in materials that make up the vadose zone in montane soils (usually unconsolidated weathered bedrock or coarse soil) is essential in streamflow prediction (e.g., *Kelleners et al.* 2010).

1.2 Unsaturated Flow in Coarse Conglomeratic Sediment

With a growing global population comes the need for better utilization of previously undeveloped or under-developed landscapes to better meet the needs of humans. This includes converting once arid soil to fertile agricultural land and developing areas that have previously been less desirable locations, such as floodplains and riparian areas. Many of these areas have thin soil layers and are composed of coarse ($d > 2$ mm), sometimes conglomeratic soil/sediment with a significant fraction of gravel ($2 \text{ mm} < d < 63$ mm) or cobble ($d > 63$ mm) sized particles. Riparian areas and floodplains generally have a very thin vadose zone and the proximity to rivers or other surface water sources (e.g., marshes and oxbow lakes) means that a quantitative

understanding of infiltration and θ distribution in these landscapes, and in coarse, conglomeratic sediment in general, is important for maintaining healthy streams and riparian areas as well as for supporting the people who inhabit those areas.

There has been a substantial amount of work in coarse, conglomeratic sediment that has focused on how the presence of cobbles affects conditions such as flow (*Cousins et al.* 2003; *Sauer and Logsdon* 2002; *Milczarek et al.* 2006) and overall moisture content or porosity (*Zhang et al.* 2011; *Bouwer and Rice* 1984), but none of this work has been on in situ sediment at the field scale. The accepted conceptual understanding is that non-porous cobbles inhibit flow by lengthening flow paths around these objects (*Bouwer and Rice* 1984; *Mehuys et al.* 1975) and reduce overall porosity because they are large zero-porosity zones. In the method developed by *Bouwer and Rice* (1984), the hydraulic conductivity (K) and moisture retention curves $\theta(\psi)$ for coarse conglomeratic sediment were determined by estimating values for the fine-grained fraction and correcting for the volume of the coarse-grained fraction. This method implies that coarse material inhibits flow in a linear (or quasi-linear) fashion and that fine-grained material has the dominant influence over hydraulic properties in the vadose zone. Other methods were developed on the same premise (e.g., *Peck and Watson* 1979). *Milczarek et al.* (2006) tested the Bouwer and Rice method against laboratory measurements of $\theta(\psi)$ and $K(\psi)$ on repacked coarse material while varying the fraction of gravel and found that the correction method led to large errors. The concept that non-porous cobbles inhibit flow in conglomeratic material because of increased tortuosity is conceptually sound, but whether these same processes apply to unsaturated flow is somewhat speculative. The Bouwer and Rice method essentially assumes that cobbles affect the entire $\theta(\psi)$ and $K(\psi)$ functions equally

across all moisture levels. At the end of this dissertation I use evidence developed in the following chapters to hypothesize that the influence of cobbles is greater at high saturation and diminishes with decreasing θ.

Several different constitutive functions have been derived to express the relationships between θ, K, and ψ and predict flow in soil under unsaturated conditions (e.g., *Brooks and Corey* 1964; *Gardner* 1958; *Kosugi* 1994; *Mualem* 1976*; van Genuchten* 1980). For the work presented in the following chapters, I use exclusively the van Genuchten-Mualem relationships (*Mualem* 1976*; van Genuchten* 1980 – see section 3.2.3 for a full description) because they are some of the more widely used functions, are continuous (e.g., $d\theta/d\psi$ and $dK/d\psi$ exist everywhere), and perform better in the modeling used in this study than other relationships (e.g., *Brooks and Corey* 1964). The van Genuchten- Mualem (VGM) relationships were derived from laboratory experiments performed on fine-grained soil cores and were aimed at describing flow and θ distribution in primarily agricultural soils (sandy loam, silty clay, etc.). Over the past few decades these constitutive relationships have been applied to nearly every type of soil/sediment and numerous studies (too many to list here) have shown that they accurately describe the complex θ-ψ-K relationships. Several authors have compiled these studies to produce "representative" VGM values for specific soil types (*Carsel and Parrish* 1998; *Rawls et al.* 1982). These compilation studies are frequently used as references in modeling manuals (e.g., in *Lapalla et al.* 1987 and *Simunek et al.* 2005) for identifying VGM values for specific soil types rather than requiring laboratory tests, and estimating VGM parameters, for each individual soil. Such extensive databases do not exist for coarse sediment as there have been few published VGM values for coarse sediment.

Characterization methods that rely on correction for the coarse fraction (e.g., *Bouwer and Rice* 1984; *Peck and Watson* 1979) are only possible if representative samples of in situ material are available (discussed in the following paragraph). The study of unsaturated flow in coarse, conglomeratic material, and characterization in general, is difficult for a number of reasons which stem from 1) the often unconsolidated nature of such material and 2) the large material grain size. A common method for studying soil/sediment is to take a sample and perform tests in a controlled laboratory environment. With such tests it is important to maintain the structural integrity of the sample (e.g., orientation, compaction, porosity) to ensure that it is an accurate representation of the in situ material. In unconsolidated material this is extremely difficult because there is little coherence between individual soil grains and samples are at risk of crumbling when extracted or transported (*Cousin et al.* 2003; *Mehuys et al.* 1975). Additionally, it is important that sediment samples are representative of the average material distribution. In coarse sediment where the largest grains can be on the order of 10 cm in diameter, it would require a sample significantly larger than that to provide a representative elementary volume (REV). Samples of such size are logistically difficult to obtain as well as to use in laboratory tests. A few studies have looked at the direct application of the VGM relationships to coarse, conglomeratic sediment (*Dann et al.* 2009*; Ma et al.* 2010; *Milczerik et al.* 2006) but have focused only on laboratory measurements made on reconstructed sediment and not in situ characterization.

Methods where vadose zone properties are measured in situ are better suited to capturing the REV and overcoming issues with consolidation, but still they have their difficulties. Soil pits are an often utilized method for measuring in situ properties of

sediments but are still burdened by issues of lack of consolidation, including the danger of collapse of the pit face. Methods where direct measurements in the soil are made (e.g., tensiometers, TDR probes) are further complicated by instrument contact (for good hydraulic continuity) and sampling volume (point measurement vs. volume measurement). With coarse sediment that contains large cobbles and potentially large pore spaces, a point measurement (e.g., tensiometer probe) could be made either within a large pore or in contact with a large cobble. Both scenarios would result in an unrepresentative value of the average properties in the sediment. Volumetric measurements (e.g., neutron moisture probes) taken near several large cobbles will result in underestimation of θ but measurements in zones with little cobble fraction will overestimate θ. Measurements taken at the REV scale would provide average values but would likely be too large to capture high-resolution data important for transient tests (e.g., infiltration). The ability to fully capture the heterogeneity at the sand – cobble scale is inherent to work in conglomeratic or bimodal material. Despite these limitations, there are methods that are well-suited for unconsolidated materials, such as the bore-and-backfill method described by *Hubbell and Sisson* (1998). This method is described in detail in Chapter 2 and was used in Chapter 3 to obtain accurate $\psi(t)$ measurements in the coarse, conglomeratic soil of the study site.

1.3 Chapter Preview

In the following dissertation I extend the current level of understanding of unsaturated flow and moisture distribution in coarse, conglomeratic sediment and indirectly investigate the influence of large cobbles on VGM relationships. I specifically focus on answering two main questions: 1) can VGM or similar constitutive relationships

that were developed for fine-grained soils be applied to coarse, conglomeratic sediment as is (i.e., without correction or separate consideration of the coarse-grained fraction)? And 2) if VGM relationships apply, what are representative values for conglomeratic sediment and are these values similar to typical fine-grained soil or to values that would be obtained from the fine-grained fraction alone? Both questions are answered through execution of an infiltration test and modeling of the observed $\theta(t)$ and $\psi(t)$ data. Furthermore, I use the results to place unsaturated behavior in context with respect to cobble influence and unsaturated processes and make suggestions for follow-up work to fill the remaining knowledge gap.

Chapter 2 provides background on the Boise Hydrogeophysical Research Site (BHRS), where the infiltration test was conducted. This chapter describes the geology and hydrology of the site and establishes it as a natural, well-characterized research site. Chapter 2 also contains information on vadose zone instrumentation and calibration. Chapter 3 presents the design and results of the infiltration test and the construction and results of the 1D modeling. It culminates with estimates of VGM parameter distributions and uncertainty and establishes that VGM relationships can be applied to the bulk coarse conglomeratic soil without correction. The information contained in Chapter 3 is also available in *Thoma et al.* (in press). Chapter 4 describes the development of the 2D model and shows how parameter optimization was used to 1) identify heterogeneity, and 2) estimate final parameter values and uncertainty. Chapter 4 results provide improved estimates of VGM parameters for BHRS vadose zone material with reduced uncertainty from Chapter 3. Chapters 3 and 4 present some of the first published $\theta(\psi)$, $K(\psi)$ relationships and VGM parameters for in situ, coarse, conglomeratic sediment. Chapter 5

addresses the main conclusions of each chapter and where future efforts and improvements can be made in understanding and quantifying vadose zone behavior in this widespread class of sediments.

CHAPTER 2: BHRS ENVIRONMENT, FIELD SITE, AND DATA COLLECTION

2.1 Introduction

In this chapter I present a brief introduction to the BHRS to familiarize the reader with the study area and the type of data collected there. An overall understanding of the BHRS environment is important to the infiltration project discussed in the following chapters because it emphasizes that the project was conducted in a well-studied aquifer in a natural field environment. Natural field sites may have uncertainty in boundary conditions (some of which are mentioned in this chapter) and material distributions, but provide a more realistic scenario for scientific testing of natural materials with natural structure (e.g., heterogeneity). The information contained in this chapter also helps establish the BHRS as a well-characterized research site with well-understood boundary conditions and shows that careful planning went into the design of the infiltration test that was the focus of this project and is described in Chapter 3.

This chapter is presented as two main sections with specific information contained in sub-sections. Section 2.2 provides an overview of the BHRS and summarizes information collected on the river and atmosphere during an extensive monitoring campaign from 2010 – 2013; this information is relevant to later chapters. Section 2.3 presents vadose zone monitoring methods and provides descriptions of installation and calibration of instruments used during the 2010 – 2013 monitoring campaign and during the infiltration test presented in Chapter 3. Much of the information

contained in Section 2.3 is from technical reports by *Aishlin et al.* (in prep) and *Johnson et al.* (2013b). All data collected during the 2010 – 2013 monitoring campaign are available in the DataBase Management System (DBMS) which can be downloaded at http://cgiss.boisestate.edu/bhrs/bhrs-data/. All data and figures taken from technical reports are used with permission from all authors.

2.2 Site Overview

The BHRS is located 15 km southeast of Boise, Idaho on a 0.036 km^2 gravel bar adjacent to the Boise River (Figure 2-1). The unconfined aquifer has been an important site for hydrologic and geophysical characterization of aquifer properties and groundwater flow in heterogeneous, coarse, conglomeratic sediment (*Barrash et al.* 1999; *Reboulet and Barrash* 2003). The BHRS gravel bar is composed of coarse alluvial material ranging in size from fine sand to large (d > 20 cm) cobbles and is primarily structured into zones of uniform fine-coarse sand lenses with high porosity (ϕ) interbedded within coarse, conglomeratic sediment units (i.e., mixed sand-gravel-cobble) with relatively low porosity (Figure 2-2) (*Barrash and Clemo* 2002). This structure and material type is typical of high-energy fluvial deposits (Figure 2-3) and represents a variable-energy depositional environment (i.e., variable annual and sub-annual discharge).

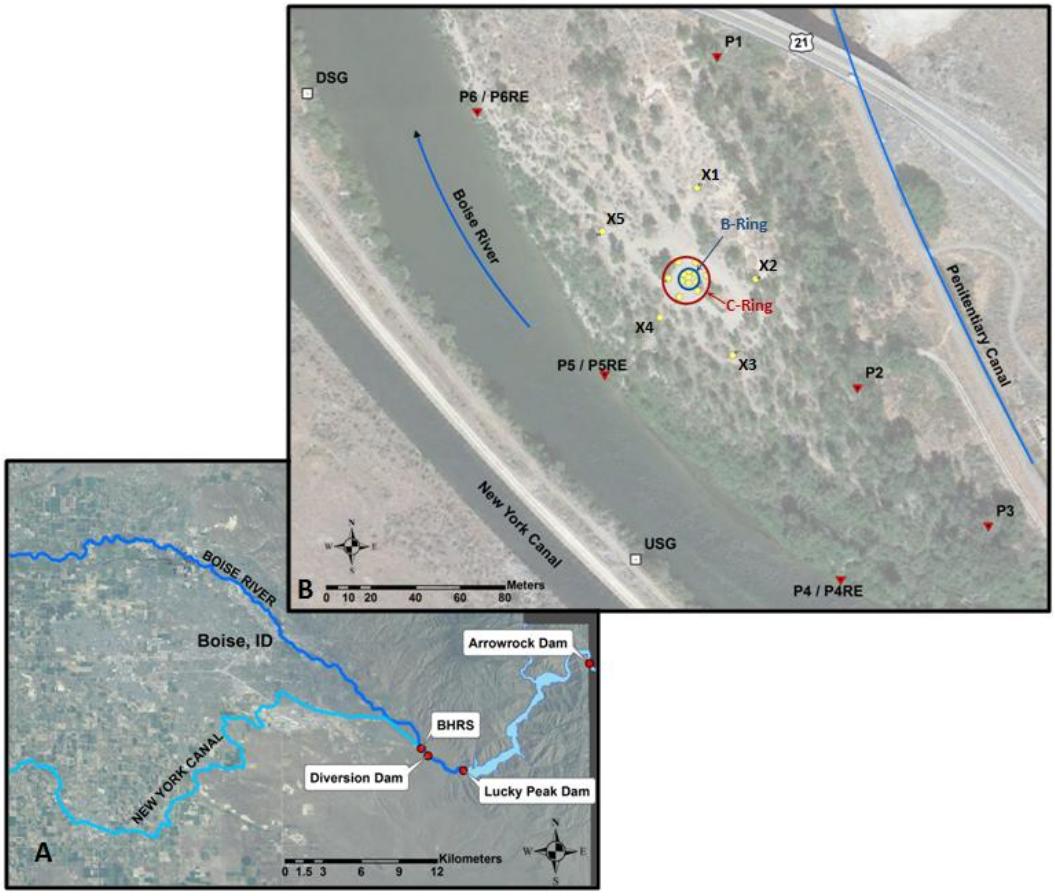

Figure 2-1: A) Overview of Boise area showing BHRS and nearby dams along the Boise River; B) BHRS and hydrologic measurement locations.

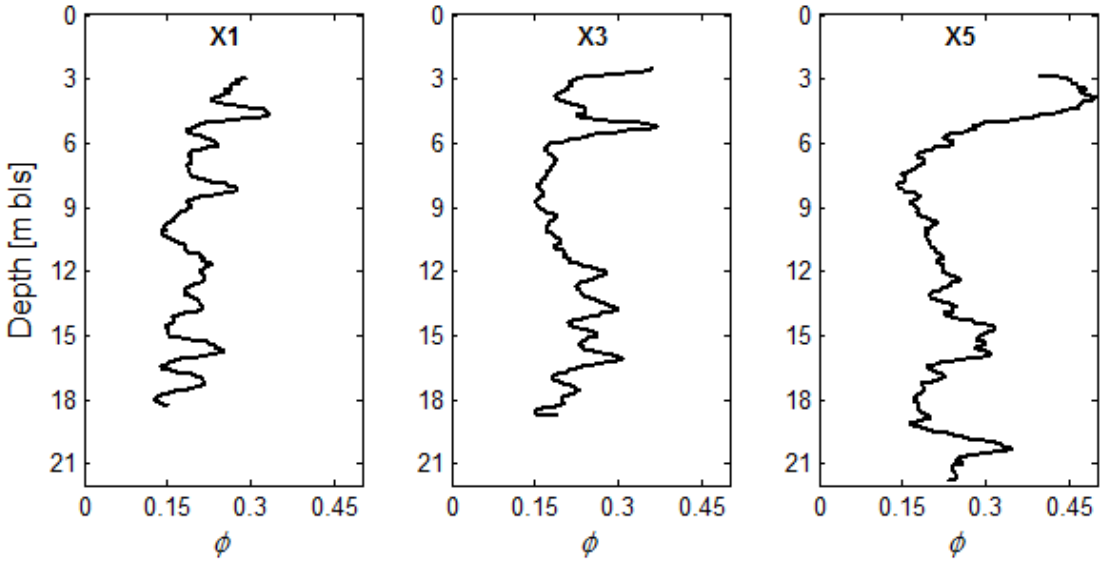

Figure 2-2: Porosity logs from selected wells at the BHRS show alternating high-porosity and low-porosity layers.

Figure 2-3: Road-cut along the Boise River near the BHRS showing typical high-energy alluvial deposit and structure (note standard-size utility van for scale).

Since establishment of the BHRS in 1997, numerous experiments and investigations have been conducted at the BHRS including pump tests and slug tests (*Barrash et al.* 2006; *Cardiff et al.* 2011; *Barrash and Cardiff* 2013; *Malama et al.* 2011), tracer tests (*Dafflon et al.* 2011; *Nelson* 2007), seismic, ground-penetrating radar, and electrical geophysical tests (*Bradford et al.* 2009; *Clement and Barrash* 2006; *Slater et al.* 2011), and most recently hydraulic tomography (*Cardiff et al.* 2012), river-aquifer interactions (*Thoma et al.* in prep), and aquifer-atmosphere investigations (*Johnson et al.* 2013a; *Malama and Johnson* 2010; *Thoma et al.* in press). Despite the efforts devoted to characterizing the subsurface, specifically the saturated zone, there remains a lack of quantitative investigation of interactions between the aquifer and adjacent Boise River (discussed below) and the aquifer and atmosphere (i.e., vadose zone). Issues with the vadose zone are addressed in this project and river-aquifer interactions are discussed in detail in *Thoma et al.* (in prep).

In the remainder of this section I highlight the Boise River hydrograph (controls water table elevation), address the climate of the BHRS, and show aquifer responses to natural precipitation.

2.2.1. Boise River

The BHRS is located downstream from a series of large dams that regulate flow in the Boise River. The nearest dam, Diversion Dam, is < 1 km upstream from the site while two larger dams, Lucky Peak Dam and Arrowrock Dam, are located 5 km and 22 km upstream, respectively (Figure 2-1). A third large dam, Anderson Ranch Dam, is located 87 km upstream from the BHRS but is not on the main Boise River and therefore is not described here. Lucky Peak and Arrowrock Dams are used primarily for flood

management, water storage for irrigation, and recreation while Diversion Dam is used to divert water from the Boise River into the New York Canal. The New York Canal provides irrigation throughout the Boise River Valley. Discharge is managed by the Bureau of Reclamation (BoR) who control the timing and volume of discharge while maintaining a balance between water needs downstream (e.g., agricultural irrigation for much of the Treasure Valley) and water supply upstream (in the Boise Mountains and Boise River Watershed).

The water table at the BHRS and the thickness of the vadose zone are directly controlled by the river stage, and the annual range of stage can produce > 2 m of change in the water table elevation during the course of a year leading to vadose zone thicknesses between ~3 m in the winter and < 1 m during the spring. The water table responds rapidly to changes in river stage but does not reach equilibrium until several days after a stage change (*Thoma et al.* in prep). In this regard, experiments that require stable water table conditions (e.g., infiltration tests) can only be conducted during certain times of the year when Boise River discharge is stable (i.e., summer or winter).

Typical hydrographs for water exiting from Lucky Peak (main control of Boise River discharge) show a stable winter period with discharge (Q) = 6 – 15 $m^3\ s^{-1}$ (210 – 530 $ft^3 s^{-1}$) from October until March or April. This is followed by a high discharge period in the spring when water is released in response to spring runoff and Q can reach > 250 $m^3 s^{-1}$ (9000 $ft^3 s^{-1}$) during high-water years. Finally, during summer months Q = 30 – 60 $m^3 s^{-1}$ (1000 – 2000 $ft^3 s^{-1}$) and is maintained for irrigation and recreation. Average winter and summer flows are comparable through the years but maximum discharge and duration of spring flows can vary drastically depending on winter snowpack and timing

of spring runoff. Discharge out of Lucky Peak and Arrowrock Dams, and diversions into the New York Canal at Diversion Dam, are strictly regulated and data are available from the BoR website (http://www.usbr.gov/pn/hydromet/). Discharge is not measured out of the bottom of Diversion Dam (the dam nearest the BHRS) and thus discharge in the Boise River at the BHRS (Q_{BHRS}) must be calculated from discharge out of Lucky Peak (Q_{LUC}) and discharge through New York Canal (Q_{NYC}) (*Thoma and Barrash* 2012). Figure 2-4 shows measured Q_{LUC}, Q_{NYC}, and estimated Q_{BHRS} for 2010 and 2011. Higher and longer-lasting spring flows in 2011 were the result of greater snowpack and heavy spring rains in the Boise Mountains. The infiltration test discussed in Chapter 3 was conducted in August of 2011 during the stable summer discharge period.

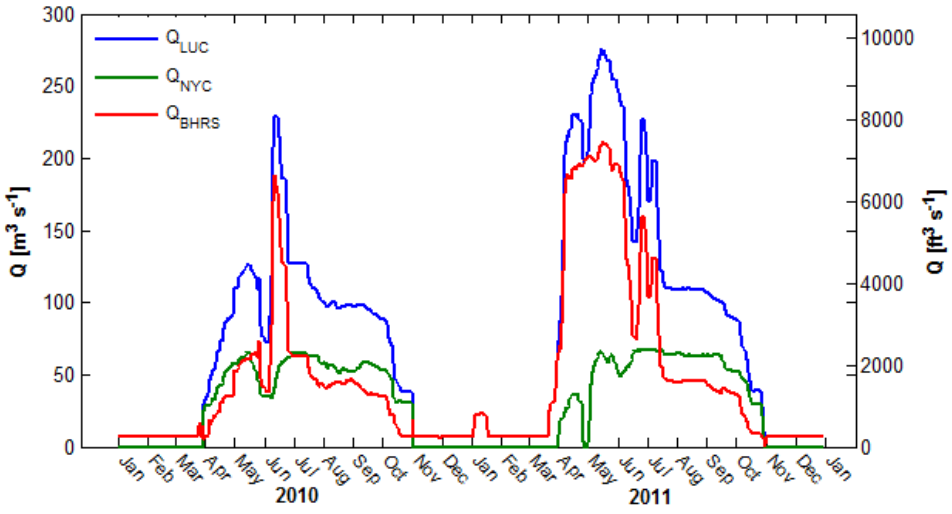

Figure 2-4: Reported Lucky Peak (Q_{LUC}) and New York Canal (Q_{NYC}) discharge, and calculated discharge at the BHRS (Q_{BHRS}) for 2010 – 2011.

2.2.2 Atmospheric Data

From 2010 – 2013 an atmospheric pressure/temperature logger was recording data at the BHRS. The purpose of this logger was to adjust submerged pressure/temperature loggers for changes in atmospheric pressure but it also provided a record of on-site air

temperature. The BHRS and the surrounding area are classified as a semi-arid climate. Average annual temperature in the Boise area is ~11 °C with an annual range in mean daily temperature of approximately ±16 °C; the area receives ~28 cm of precipitation annually, most of which falls as rain in the winter months (*Thoma et al.* 2011). Air temperatures that are measured at the BHRS with the atmospheric logger are similar to those measured elsewhere in the Boise area (Figure 2-5).

Additional weather data that are pertinent to aquifer-atmosphere and evapotranspiration (ET) studies (e.g., precipitation, solar radiation, wind speed) are not available at the BHRS but are collected at an Agrimet weather station maintained by the Bureau of Reclamation located within the city of Boise ~9 km from the BHRS. Precipitation measurements or data that are used to estimate ET (e.g., solar radiation) are of interest to BHRS studies, and are often taken from the Agrimet site and applied to the BHRS (*Johnson* 2011) with the assumption that the climate is not significantly different. Differences in mean daily air temperature (T_{air}) measured at the BHRS and at the Agrimet site are < 2 °C on average but the BHRS experiences slightly higher maximum daily temperatures (T_{max}) (Figure 2-5). Despite these small differences, these data imply considerable consistency between weather at the BHRS and the Agrimet weather site. Measurements of solar radiation made at the BHRS have also been consistent with the Agrimet site (*Johnson* 2011). The similarities between the BHRS and the Agrimet weather station are important to show because precipitation data used in Section 2.2.3 and in Chapter 3 are taken from the Agrimet site and not directly measured at the BHRS.

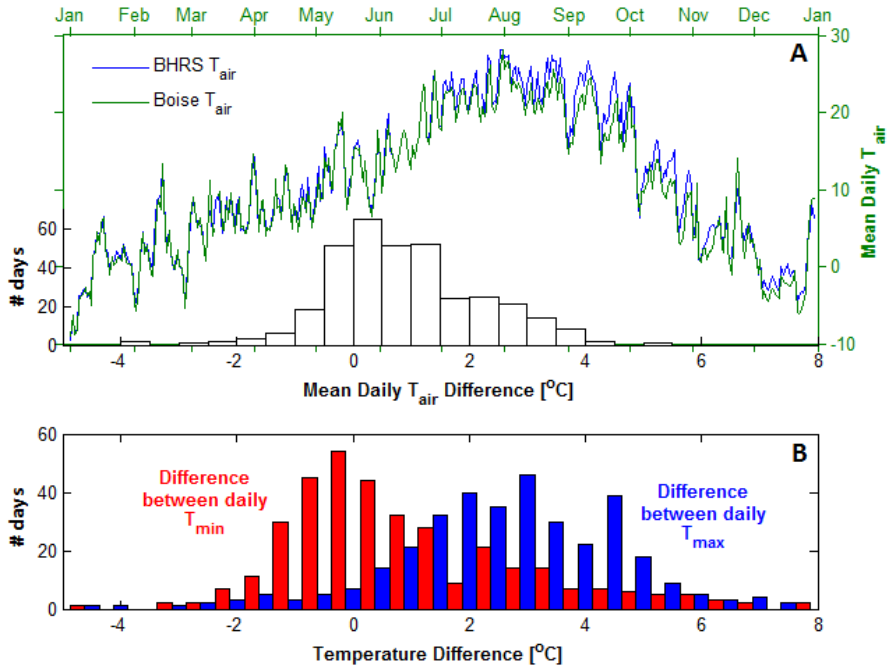

Figure 2-5: A) Mean daily T_{air} measured at BHRS and at Boise Agrimet site (right axis) and distribution of mean temperature difference (left axis); B) distribution of maximum (T_{max}) and minimum (T_{min}) daily temperature difference.

2.2.3 Well Head Response to Precipitation

Well head data have been measured nearly continuously from 2010 – 2013 in several wells and piezometers across the BHRS with the purpose of observing rapid and seasonal changes in the water table elevation caused by changes in river stage (*Thoma et al.* in prep) or due to ET (*Johnson et al.* 2013a). These data occasionally also show rises in the water table following high-intensity winter storms. During several rain events in the winter of 2011 – 2012, there was a 2 – 5 cm rise in water level in nearly all wells and piezometers across the site within a few days after the rain (Figure 2-6). These responses are observed frequently between autumn and spring when heaviest rains fall at the BHRS and ET is at a minimum, and are classic examples of the piston-flow conceptual model of infiltration. When infiltration is applied to the entire surface, it can only move downwards until it reaches the water table. Once at the water table, the low water table

gradients at the site and the full areal distribution of additional water lead to the observed, temporary rise of the water table. The magnitudes of these responses vary with precipitation rate and duration, as expected, but also with distance from the well to the river; wells/piezometers close to the river experience higher gradients towards the river during precipitation-forced water table rise and thus mounding due to precipitation is more quickly equalized in well/piezometers closer to the river (e.g., piezometers P5) than farther away (e.g., piezometer P2).

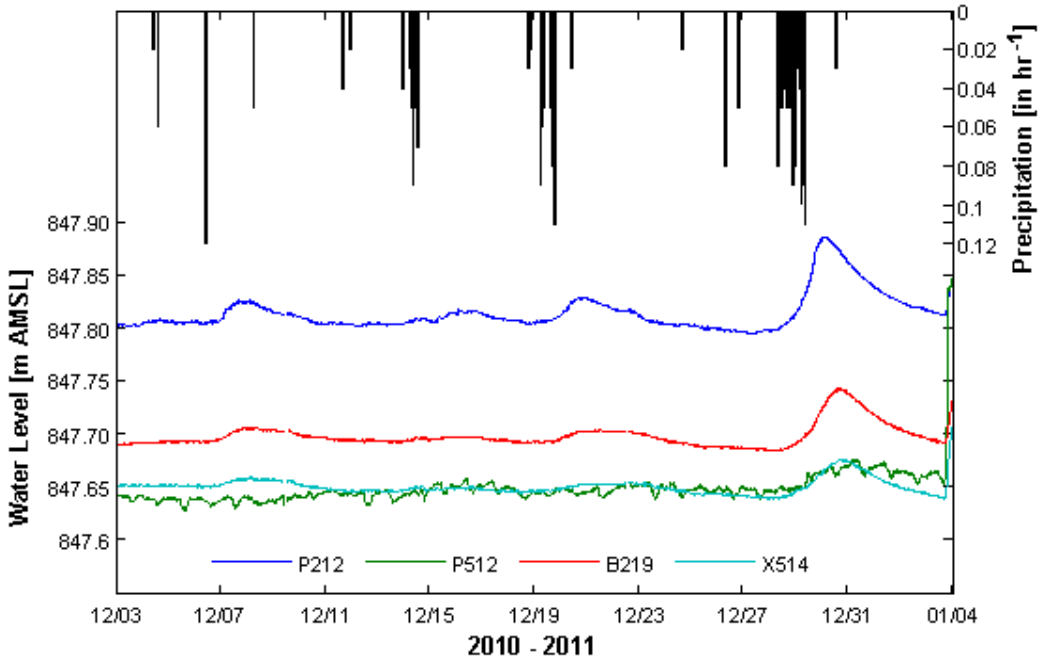

Figure 2-6: Observed water table response to precipitation (first two characters in legend values identify well location (P2 and P5 are piezometers, B2 and X5 are wells); second two identify depth of sensor in ft bmp).

The water table response to natural precipitation highlights the high conductivity nature of the BHRS vadose zone material, which is discussed in more detail in Chapters 3 and 4, and was used to help determine an appropriate precipitation rate for the infiltration test. Additionally, swelling of the aquifer in response to precipitation can cause additional uncertainty in aquifer tests at the BHRS since the water table may not fully recover prior

to responding to precipitation. If the response is not uniform across the site, it can produce uncertainty in the initial conditions of an experiment conducted shortly after rain storms (see Chapter 3).

2.3 Vadose Zone Instrumentation

In this section I present information on recent vadose zone installations and measurements, specifically tensiometer nests and neutron moisture probe access tubes. It also provides information on instrument calibration and uncertainty. Both types of data were used extensively during the infiltration test described in Chapter 3 and the modeling in Chapters 3 and 4.

2.3.1 Tensiometers

In the spring of 2010 and 2011, three nested tensiometer sets were installed at the BHRS near wells X1 and X5 (Figure 2-7). Each tensiometer set includes a shallow and deep nest each containing four (in the deep nest) or five (in the shallow nest) individual tensiometers vertically distributed between the maximum extent of the vadose zone (~ 3 m below land surface (bls) during winter) and ~0.3 m bls. Vertical distance between individual tensiometers is ~0.15 m. Each individual tensiometer is an Advanced Tensiometer (AT; *Hubbell and Sisson* 1998; *Sisson et al.* 2002) that records soil pore tension (ψ) and soil temperature (T_{soil}) at 15 min intervals from the time of installation until summer 2013.

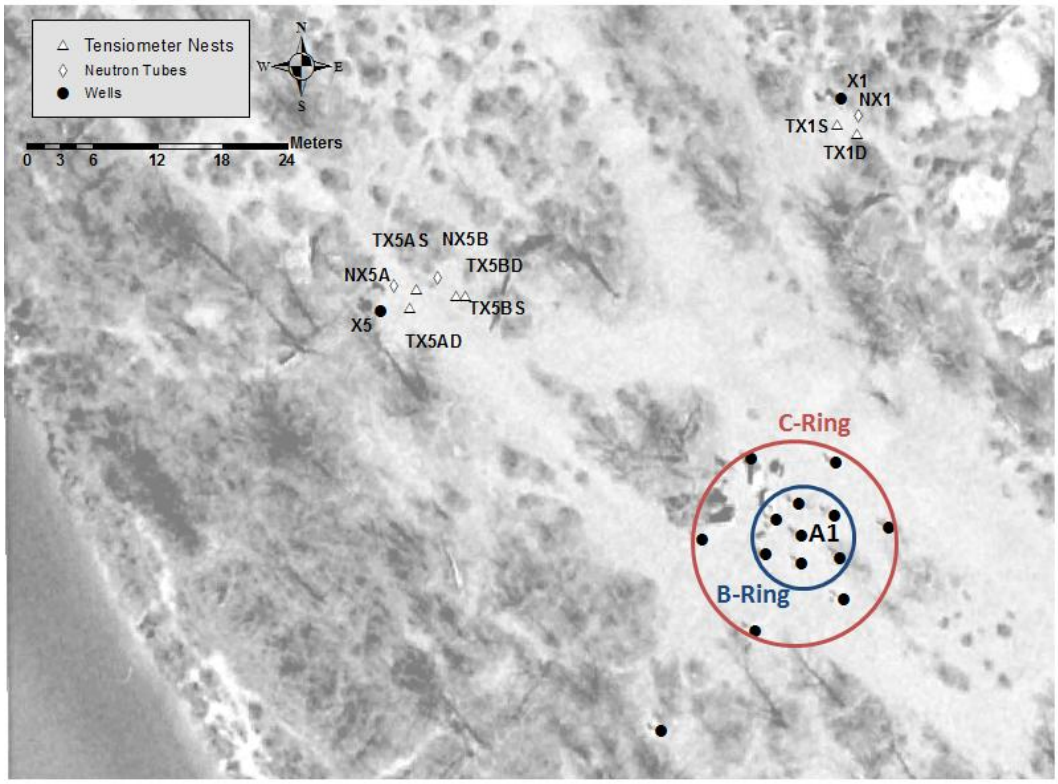

Figure 2-7: BHRS map of central well field, tensiometer nests, and neutron access tube locations.

2.3.1.1 Installation

Each tensiometer nest was installed using a bore and back-fill method which begins with a 25 cm inside diameter (ID) steel casing being driven into the vadose zone incrementally to the desired depth. The formation material is augured from the interior of the casing leaving a hollow space with the surrounding formation held back by the casing. The empty borehole is then filled with alternating layers of a fine sand/silt mixture and gravel. The sand/silt mixture is used at depths where an AT and ceramic cup (Figure 2-8) is to be placed, and gravel is used between AT depths. The former provides hydrologic continuity between the porous cup and the surrounding formation while the latter creates a barrier to unsaturated flow between vertically stratified ATs (Figure 2-9). From the time of installation until summer of 2013, AT sensors have been logging both ψ

and T_{soil} continuously at 15 min intervals. Final AT elevations for each of the tensiometer nests and detailed information on the installation and data collection process can be found in *Aishlin et al.* (in prep).

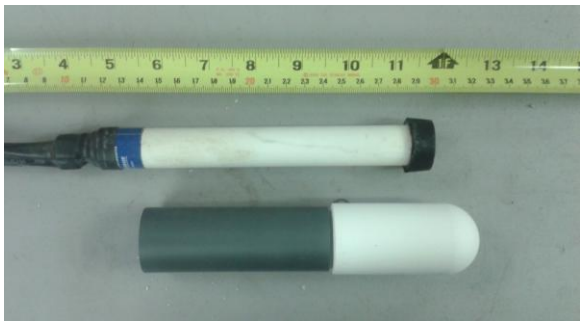

Figure 2-8: Advanced Tensiometer sensor (top) and porous ceramic cup (bottom).

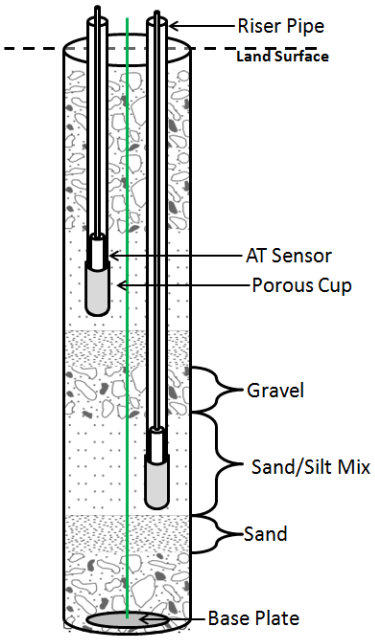

Figure 2-9: Schematic example of vertically distributed tensiometer nest.

2.3.1.2 Tensiometer Offsets

After installation of ATs, pressure data (to which individual sensor calibrations and pre-installation lab offsets were applied) were compared to actual positive pressure the ATs were under (i.e., depth of the center of the porous cup below the water table).

This comparison showed significant error between recorded pressure and actual hydrostatic pressure in several ATs and it was determined that in situ calibration and new offsets were necessary. These in situ AT offsets were determined by: 1) locating an extended time period when an individual AT was below the water table (i.e., recording positive pressure); 2) calculating AT-measured water table elevation, based on the positive pressure reading and elevation of the tensiometer; 3) calculating the actual water table elevation based on measurements made in a nearby well; and 4) calculating the difference between the AT-measured water table elevation (predicted) and well-measured water table elevation (observed). A final value of in situ offset was determined as the mean difference in water table elevation for the time period when the sensor was submerged. Only 16 of the 27 functioning ATs where submerged for sufficient time to allow calculation of in situ offsets. For sensors continuously located above the water table, offset could not be calculated with this method. AT offsets determined by this method ranged from -39.9 cm to +5.7 cm for all 16 ATs for the period of calibration (between 3 and 30 days), and variance (σ^2) in offset for any individual sensor was < 1.6 cm. As an example, I show the positive pressure data used to calculate offset for six ATs in TX5A and the calculated offsets in Figure 2-10. Full offset data procedure for all ATs can be found in *Aishlin et al.* (in prep).

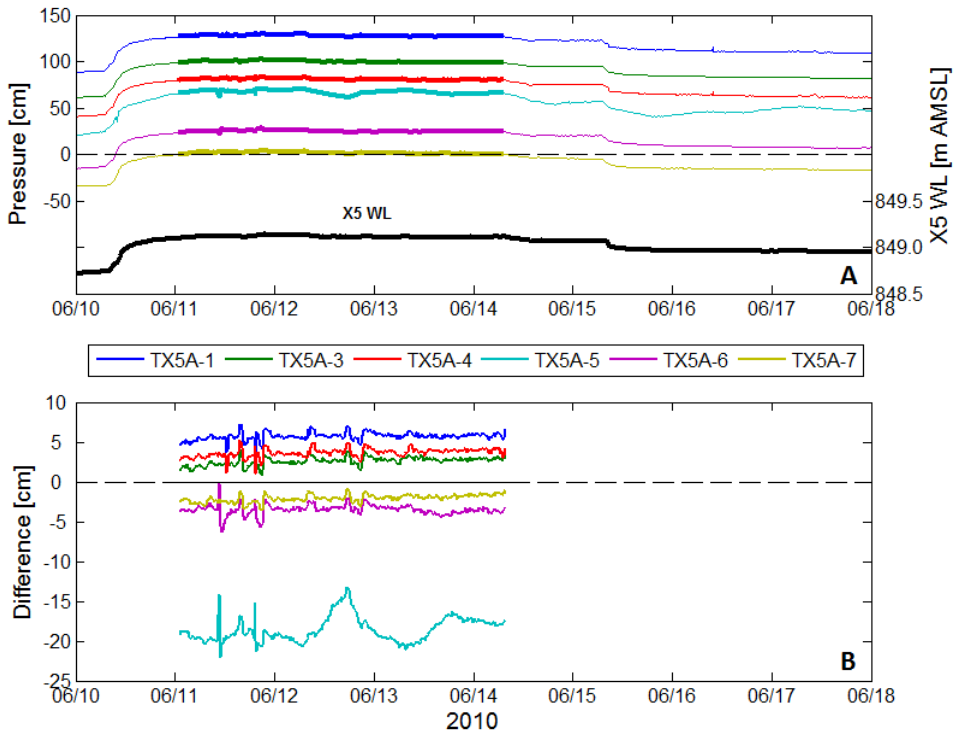

Figure 2-10: A) Submerged positive pressure data sensors from TX5A and X5 water level for time period used for calculation of in situ offsets, bold lines highlight the data used for offset calculation; B) difference between AT water level and X5 water level for stable water level period.

Although estimated σ^2 values for AT offsets were very low for the time periods used for calibration, offsets were found to vary significantly over the course of a season and the lifetime of the sensors. As an example, I show the results of offset data from TX5A-1 (i.e., AT1, which is the deepest sensor located in tensiometer nest TX5A) for the time period from installation (April 2010) through December 2011 in Figure 2-11. Calculated water table elevation data from TX5A-1 were compared to well head measured in X5 from a submerged pressure logger and offset was calculated at each data record (15 min). These "instantaneous" offsets were compared to recorded pressure and this relationship was further separated into different time periods over which AT offsets showed clear trends. In summer and autumn of 2010 when the water table was high there was a positive correlation between offset and pressure head while for similar months in

2011 the correlation was negative. In the winter months when the water table was low and stable, there does not appear to be any correlation but that may be due to the stable pressure values during these times. These relationships highlight the uncertainty inherent in the AT systems over the longer time periods but also show that offsets are quasi-stable over shorter time periods of days to weeks.

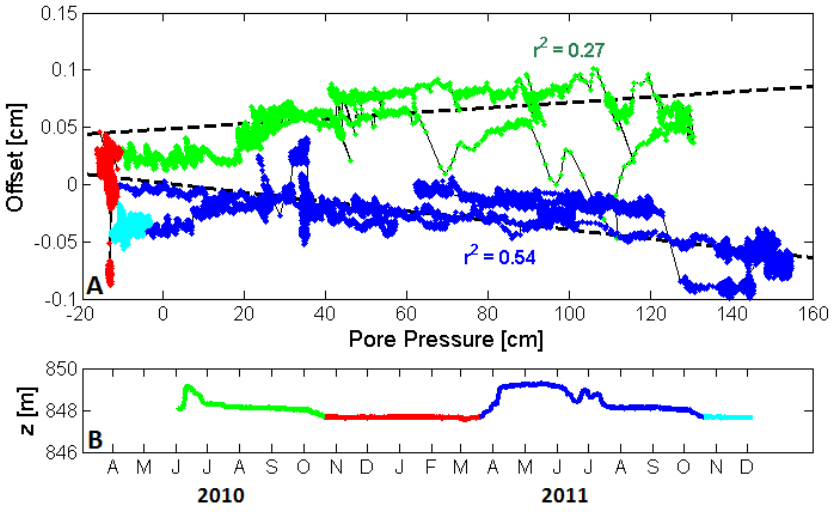

Figure 2-11: A) TX5A-1 offset as a function of pressure; colors correspond to time frames grouped by state of X5 water table elevation (pane B) (from *Aishlin et al.* (in prep)).

2.3.1.3 Seasonal Tensiometer Trends

Despite complications and uncertainty in tensiometer offsets, ATs are sufficient to measure vadose zone moisture movement in response to surface fluxes such as precipitation (both natural and artificial, see Chapter 3) and ET. This is primarily because the uncertainty in offsets is much less than the tension changes brought about by such events. In Chapters 3 and 4 I present the responses of ATs from TX5A to natural and artificial rain, and in this section I present the seasonal AT response to ET.

During the hot, dry summer months experienced at the BHRS, ET rates have been estimated at ~8 mm d^{-1} (*Malama and Johnson* 2010) and the lack of precipitation during the summer produces an extreme drying effect in the vadose zone. This drying is captured by many of the shallow ATs and an example is shown in Figure 2-12. In late June 2011, ATs began to respond to drying of the vadose zone by recording gradually lower pore pressure (higher tension) until some ATs reached the sensor limit at -400 cm. This response began at the shallowest sensors (TX5A-9, referred to as AT9 in Figure 2-12) and then was followed by sequentially deeper sensors (AT8, AT7, AT6, etc.). Later in autumn when ET diminishes and eventually shuts down and precipitation becomes more prevalent, ATs begin to respond to the additional moisture in the vadose zone by recording decreasing tension. If conditions are not so extreme during the summer that there is excessive drying or damage to the porous cup (which can damage the ATs, e.g., AT8 in Figure 2-12), the ATs will respond on their own and recover from summer dry conditions.

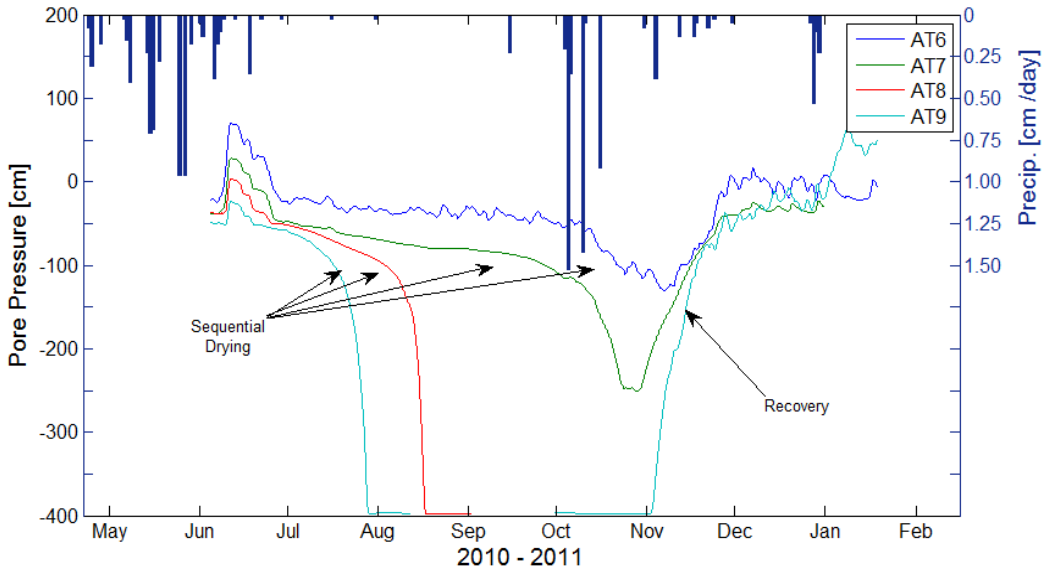

Figure 2-12: Example of sequential drying out and recovery of shallowest ATs in TX5A during summer of 2010.

2.3.2 Neutron Moisture Data

Volumetric soil moisture (θ = vol. water / total volume) was also measured at the BHRS during the 2010 – 2013 monitoring campaign. Moisture measurements were made from 2010 to 2011 using a CPN 503DR Hydroprobe (see *Evett et al.* 2003 or *Johnson et al.* 2013b for details) in six neutron access tubes (locations beginning with "N" in Figure 2-7) installed across the site. These access tubes consist of a clear plastic tube of 5 cm ID (2 in) driven into the full thickness of the vadose zone (*Johnson et al.* 2013b). The recording end of the Hydroprobe is lowered into the neutron access tube and records a neutron count at each measurement depth. The neutron count is first divided by a standard count (i.e., neutron count without the presence of soil moisture such as measured in the air) to determine a count ratio (*CR*). The *CR* is then used with a linear calibration equation to estimate θ of the material at the depth of the measurement (*Johnson et al.* 2013b). Measurements of θ have been recorded at the BHRS in five neutron access tubes

at 0.15 cm depth intervals every two weeks from May 2010 – November 2011. Data collected using the techniques described here and in Johnson et al. (2013b) were used to estimate vadose zone properties from: 1) long-term monitoring of seasonal θ data; 2) vertical profiles of θ, which identified stratigraphy within the vadose zone; and 3) coincident measurements of θ and ψ during an infiltration experiment (Chapters 3 and 4).

2.3.2.1 Neutron Probe Calibration

Calibration of the CPN 503DR Hydroprobe was determined in a controlled setting by filling a 55 gallon (0.208 m^3) plastic drum with two different sediment mixtures common to the BHRS: 1) a mixed sand and gravel sediment that was repacked to approximately the average bulk porosity (ϕ) of BHRS sediment ($\phi \approx 0.23$); and 2) uniform coarse sand, which makes up the inter-cobble space of mixed BHRS sediment layers and is also present as isolated lenses within the vadose zone and aquifer ($\phi \approx 0.44$). Repeated measurements of *CR* were taken at dry conditions ($\theta = 0$) and fully saturated conditions ($\theta = \phi$) for each material separately, and these measurements were used with a linear relationship to determine coefficients of slope and offset (*Johnson et al.* 2013b). Repeated measurements taken at the same depth under constant moisture conditions showed that measured θ values vary by ±0.03 for what is considered constant θ. This value of 0.03 was used throughout the monitoring campaign and later in Chapters 3 and 4 as standard instrument error of the neutron probe.

After performing calibration on the mixed sediment and coarse sand, and determining optimal values of slope and intercept for each sediment type separately, it was decided that due to the mixed nature of in situ material and the uncertainty in material type within the vadose zone, an average site calibration value would be more

applicable than material-specific calibration values. Average calibration values of slope and intercept were determined from fitting a linear relationship to data measured in both calibrations simultaneously (i.e., treating mixed sediment and uniform sand data as a single data set) (Figure 2-13). Average calibration values were applied to all measurements made at the BHRS. Final results for the average calibration are presented in Figure 2-13 and values of slope and intercept for individual material calibration can be found in *Johnson et al.* (2013b).

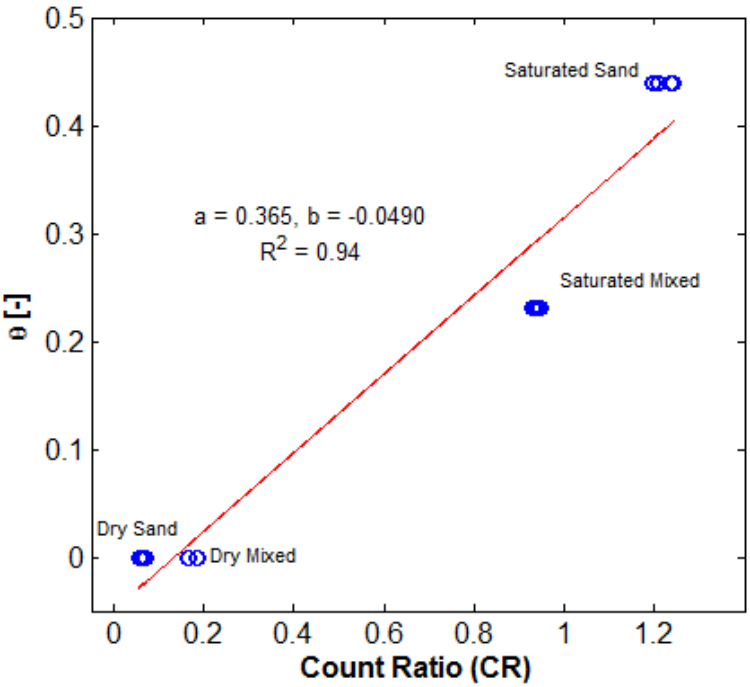

Figure 2-13: Relationship between count ratio (*CR*) and θ for dry and saturated conditions of both calibration sediments used for average site calibration (from *Johnson et al.* 2013b).

2.3.2.2 Seasonal Trends and Stratigraphy

Vertically distributed θ profiles taken throughout the year were used to identify stratigraphy in the vadose zone of the BHRS. The full θ data of the BHRS field measurement campaign can be found in *Johnson et al.* (2013b) but an example from

NX5A is provided in Figure 2-14 to highlight stratigraphy identification and seasonal trends in θ data.

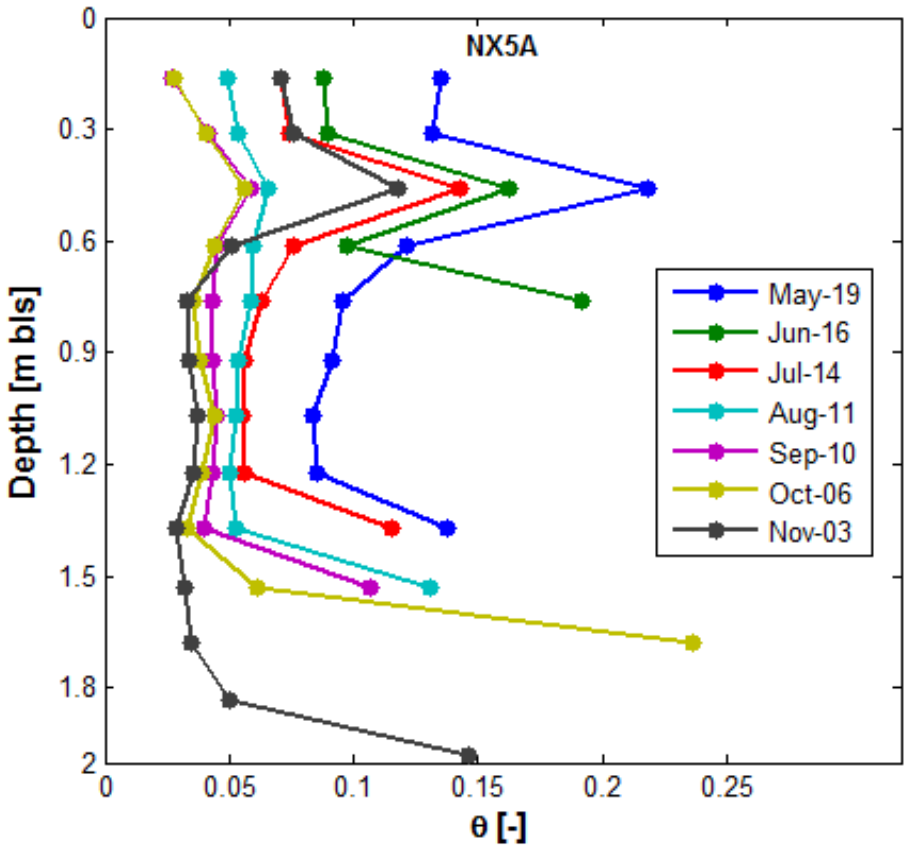

Figure 2-14: Calculated NX5A θ profiles from selected dates from May-November 2010.

Moisture data from NX5A in show evidence of stratigraphy identified from individual $\theta(z)$ profiles as well as seasonal trends from repeated profiles. Calculated $\theta(z)$ profiles recorded in NX5A between May and November 2010 show significantly greater θ at depths near 0.4 m for measurements made in the early part of the summer (May – July) than later in the fall (Figure 2-14). Greater θ at this depth was interpreted as a relatively finer material layer (e.g., coarse sand lens with higher ϕ) which holds more moisture than surrounding layers (which are interpreted as mixed sediments of lower ϕ). Indeed, a fine-medium sand layer was identified from soil cores taken near NX5A at the

same approximate depth and GPR data collected over the area confirms that this unit is continuous to NX5A (see Chapters 3 and 4).

Figure 2-14 also shows the effect of seasonal drying of the vadose zone during hot summer months. Measurements taken in May and June show slightly higher $\theta(z)$ than July and considerably higher $\theta(z)$ than August, September, and October, which represent minimum moisture conditions at the BHRS. As November approaches, $\theta(z)$ values begin to increase again with the reduction of ET and increased precipitation. These observations corroborate with what is observed in tensiometer data in Section 2.3.1.3 above.

2.4 Conclusions

In this chapter I provided a short introduction to the BHRS to establish it as a well-studied, natural research site. Additionally, this chapter provides important information on boundary conditions of the BHRS (i.e., Boise River) and background information on tension and moisture instrument installation, calibration, and seasonal trends in data. A more thorough description of the specific location of the infiltration site is presented in Chapter 3 and details of tension and moisture data collection can be found in *Aishlin et al.* (in prep) and *Johnson et al.* (2013b).

CHAPTER 3: ESTIMATION OF IN-SITU UNSATURATED HYDRAULIC FUNCTIONS OF A COARSE STONY SEDIMENT SEQUENCE FROM A FIELD-SCALE INFILTRATION EXPERIMENT, BOISE HYDROGEOPHYSICAL RESEARCH SITE

The work presented in this chapter is the basis of a research journal article submitted to Vadose Zone Journal and accepted for publication in November, 2013 with the following authors: Michael J. Thoma, Warren Barrash, Michael Cardiff, John H. Bradford, and Jodi Mead.

Thoma, M., W. Barrash, M. Cardiff, J. H. Bradford, and J. Mead. 2014. Estimation of in-situ unsaturated hydraulic functions of a coarse stony sediment sequence from a field-scale infiltration experiment, Boise Hydrogeophysical Research Site. Accepted by Vadose Zone Journal.

3.1 Introduction

In this chapter, I present the results of a field-scale infiltration experiment in a heterogeneous, conglomeratic, alluvial sediment sequence that ranges in composition from fine-medium sand to mixed sand and large cobbles (d > 10 cm). Prior information from GPR, grain-size distributions from core samples, and long-term tension (ψ) and moisture (θ) monitoring were used to build a four-material, 1D layered model. In situ soil mositure (θ [-]) and soil tension (ψ [cm]) measurements made during infiltration were used to predict parameters for the van Genuchten-Mualem soil characteristic fuctions (*van Genuchten* 1980; *Mualem* 1976). These data were used with the HYDRUS 1D unsaturated flow model (*Simunek et al.* 2005) combined with a computationally intensive

Metropolis-Hastings search algorithm to optimize parameters and estimate parameter distributions and correlation. Final parameter distributions for θ_S, α, n, and K_S for the four separate materials show high uncertainty in individual parameter values but not in VGM relationships for individual materials.

The main purposes of the infiltration test and modeling were to 1) quantitatively characterize unsaturated hydraulic properties of coarse, conglomeratic alluvial soil in situ, 2) determine whether a soil hydraulic model developed for agricultural soils, the VGM model, can be used to predict unsaturated behavior in such soil without explicitly accounting for the influence of gravel and cobbles, and 3) provide insight into parameter correlation and variance under natural field conditions given limited data. The infiltration test results show that under high, sustained infiltration rates, the coarse, conglomeratic sediments remain highly conductive, despite relatively low porosity and significant cobble fraction. The modeling results of this chapter show that VGM relationships can be applied to these sediments directly and can describe unsaturated flow behavior over the natural range of saturation.

3.1.1 Introduction to Coarse, Conglomeratic Sediment

In many arid and semi-arid regions, high-energy riparian areas, and large outwash plains, considerable portions of the surface and subsurface are covered by stony soils or coarse, conglomeratic alluvial sediments that contain significant fractions of large clasts or rock fragments with grain size diameter (d) > 2 mm (*Cousin et al.* 2003; *Miller and Guthrie* 1984). These conglomeratic alluvial soils, by which I mean alluvial sediments with composition from sand to gravel to large cobbles (d > 10 cm) and with little pedogenesis, have previously received little attention concerning unsaturated flow as they

are not well-suited for agriculture and are often present in under-developed landscapes (e.g., desert, periglacial, and floodplain environments). With recent population increases comes sprawl into regions where these alluvial soils dominate, and there has been an increasing interest in unsaturated flow properties of these materials. Additionally, these types of materials make up a substantial portion of periglacial and permafrost environments (*Lunt et al.* 2004), which are sensitive to climate change processes involving exchange of water, gas, and heat through the vadose zone.

The presence of rock fragments in soil has been linked to significant alterations to water flow mechanics and soil heat flux in the vadose zone (*Cousin et al.* 2003) with particular focus given in the fields of contamination and mine waste (*Corwin et al.* 1999; *Dann et al.* 2009; *Milczarek et al.* 2006), radioactive waste storage (*Oostrom et al.* 2009; *Oostrom et al.* 2011; *Tokunaga et al.* 2003), artificial groundwater recharge (*Hendrickx et al.* 1991), hillslope erosion (*Cerda* 2001; *Sauer and Logsdon* 2002), and geotechnical engineering (*Zhang and Chen* 2005). Several studies have also addressed the influence that stone fragments have on infiltration and available water content in stony soils. *Mehuys et al.* (1975) published some of the first research on the effects of rock fragments on unsaturated hydraulic properties and concluded that their presence strongly affects moisture content (θ) and saturated hydraulic conductivity (K_s). Since then, other studies looked at the influence of stones but primarily focused on determination of saturated parameters (e.g., K_s), or available water content (*Cerda* 2001; *Cousins et al.* 2003; *Hendrickx et al.* 1991; *Sauer and Logsdon* 2002; *Tetegan et al.* 2011). *Peck and Watson* (1979) and *Bouwer and Rice* (1984) developed pedotransfer functions for determining unsaturated hydraulic properties of stony soils based on hydraulic properties of the fine-

grained matrix ($d < 2$ mm) and the proportion of rock fraction ($d > 2$ mm). *Dann et al.* (2009) showed that parameters identified using the fine-grained material, with a correction made for gravel content, can be successfully applied to field-scale studies, but they emphasized the need for in situ studies on bulk material.

Milczerik et al. (2006) and *Ma et al.* (2010) both focused on estimating unsaturated soil parameters (particularly curve shape parameters α and n) of coarse materials (sand and gravel) using repacked soil columns while varying the proportion of rock fragments, but they could not determine a clear relationship between parameter values and rock fraction. *Ma et al.* (2010) further suggested that field experiments were essential to providing insight into parameter estimation in stony soils and other authors have also suggested that methods performed on soil samples or simulated soil structure are not sufficient to represent field conditions (e.g., *Dann et al.* 2009; *Laloy et al.* 2010; *Ritter et al.* 2003; *Wohling and Vrugt* 2011). Numerous studies have been published on obtaining in situ hydraulic properties of agricultural soils but, to our knowledge, only a few sets of unsaturated hydraulic properties have been published for coarse stony soils (e.g., *Dann et al.* 2009; *Ma et al.* 2010; *Milczarek et al.* 2006), and most have expressed the need for validation from in situ studies. Furthermore, few studies have looked at in situ properties of such coarse conglomeratic soil as I consider in this study.

Many of the previous studies involving stony soils were based on either simulated soils or experiments performed on reconstructed soil cores or columns. These methods have been preferred in unconsolidated soils because of difficulties associated with obtaining intact, representative soil samples in coarse alluvial soil. When collecting samples, it is important to capture the heterogeneity of a non-uniform soil but, because

coarse alluvial soils can range in grain size from fine sand or silt to gravel and cobble, representative sample volumes may need to be quite large, which would be logistically difficult to obtain and then perform lab tests (Dann *et al.* 2009; *Dunn and Mehuys* 1982; *Zhang et al.* 2011). Field methods eliminate sampling bias but are difficult in coarse alluvial soils because issues often arise with obtaining proper instrument contact with the soil structure, minimizing disturbance to the soil, and ensuring sensors are capturing heterogeneity caused by grain size variation (*Cousin et al.* 2003; *Edwards et al.* 1984; *Ma et al.* 2010). Also, where these soils are poorly consolidated, excavating an open pit face or borehole can be difficult and even hazardous. Despite efforts to characterize unsaturated hydraulic properties of coarse alluvial soils, there is still a lack of sufficient data to allow one to infer general relationships about hydraulic properties of these soils, specifically at field scales (*Cousins et al.* 2003; *Ma et al.* 2010), and there have not been sufficient data published to allow one to estimate property values from a literature search or from pedotransfer functions, in contrast to what is available for typical agircultural soils (e.g., *Carsel and Parrish* 1988; *Leij et al.* 1996; *Rawls et al.* 1982).

3.2 Methods

3.2.1 Experimental Setting

The setting for the infiltration experiment was the BHRS located 15 km southeast of downtown Boise, Idaho. The site covers 0.036 km^2 of a gravel bar adjacent to the Boise River (Figure 3-1). The upper 18 m of the gravel bar consist of coarse, unconsolidated mixed sand /gravel/cobble deposits with interbedded fine-coarse sand lenses and underlain by an extensive clay/basalt boundary. There is little to no

pedogenesis at the site except in low-lying areas upstream from the main wellfield and along the river edge, where the surface becomes inundated during seasonal flooding. In these areas, surface sediments are primarily sand, gravel, and cobbles but contain a thin surface layer of silt/sand and organic detritus but still no distinct soil horizons. Across the site the sediment supports vegetation which includes grasses, shrubs, and deciduous trees; hence our classification of it as an alluvial soil. Vadose zone thickness varies with topography and seasonally with river stage from ~3 m during winter to between 1.5 – 2 m during the summer, when river stage is higher.

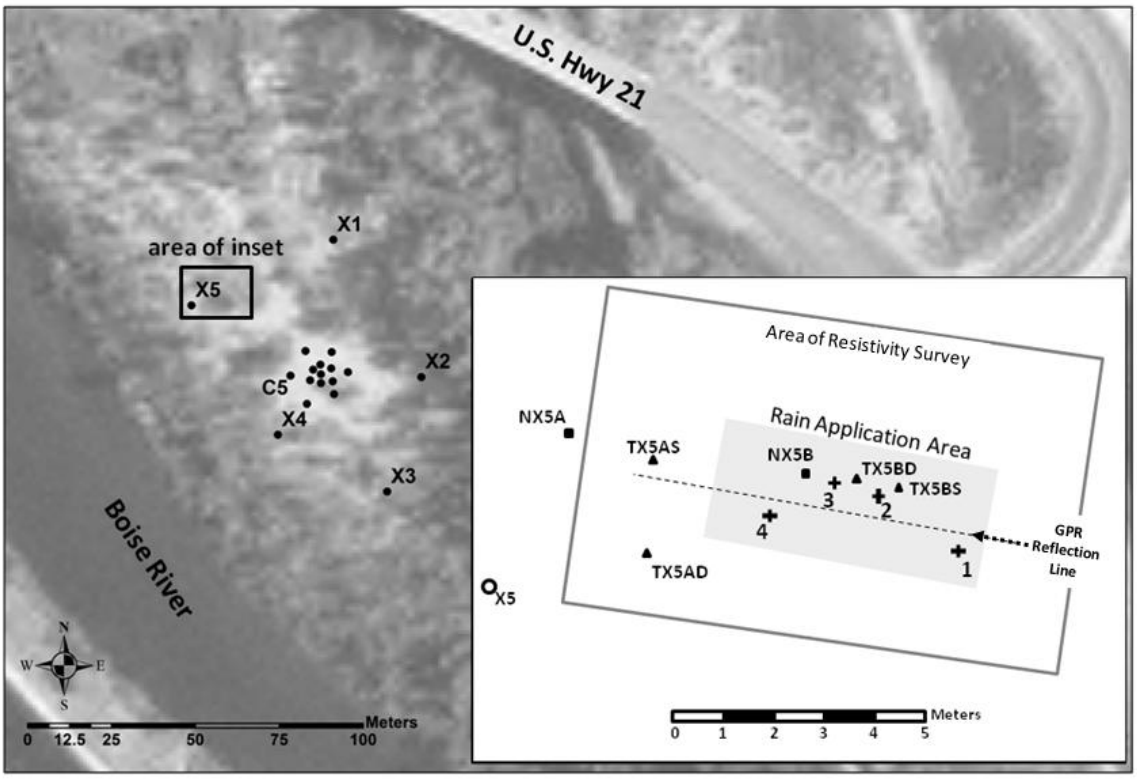

Figure 3-1: Areal view of BHRS showing water monitoring wells (•) and infiltration test area; inset shows detailed schematic of infiltration setup showing locations of hydrological and geophysical measurements (crosses correspond to rain bucket locations).

Vadose zone composition is identical to aquifer composition that has been extensively studied using numerous hydrologic and geophysical experiments which have identified layered stratigraphy within the aquifer and led to a highly characterized subsurface in terms of saturated properties and material distributions (*Barrash and Clemo* 2002; *Barrash and Reboulet* 2004; *Bradford et al.* 2009; *Clement et al.* 2006; *Clement and Barrash* 2006; *Dafflon et al.* 2011; *Moret et al.* 2006; *Mwenifumbo et al.* 2009; *Slater et al.* 2011). Porosity estimates vary across the site but are generally between 10 and 30% in stratigraphic units identified as mixed sand/gravel/cobble, and up to 50% in sand lenses (*Barrash and Clemo* 2002). A number of techniques have been used at the BHRS to estimate K_S, and average values per well or stratigraphic unit range from 0.04 cm s^{-1} to 0.16 cm s^{-1} (*Barrash et al.* 2006; *Barrash and Cardiff* 2013; *Cardiff et al.* 2011, 2012; *Malama et al.* 2011; *Straface et al.* 2011). More recently, research at the BHRS has been extended into aquifer-atmosphere interactions including investigations of evapotranspiration effects on water table drawdown (*Johnson et al.* 2013a; *Malama and Johnson* 2010) and vadose zone hydrology (e.g., this study).

Tensiometers were used to measure ψ at the BHRS and were installed as vertically distributed nests using Advanced Tensiometers (AT) (*Sisson et al.* 2002) installed with a back-fill method which results in very little disturbance of the surrounding material (similar to *Hubbell and Sisson* (1998) and *Cassel and Klute* (1986) – see Chapter 2). Each set was installed as paired shallow and deep nests consisting of four deep (AT1 – AT4) and five shallow (AT5 – AT9) ATs with vertical spacing of 0.2 – 0.3 m between sensors. Two of the three tensiometer sets (TX5B (shallow and deep) and

TX5A (shallow and deep)) were monitored in this test with TX5B located within the infiltration site and TX5A acting as a control (Figure 3-1 inset).

Previous analysis of tensiometer data has shown that the ATs require tension offsets (i.e., constant tension correction that must be applied to each sensor after installation) which are generally < 15 cm and are quasi-stable over time periods of weeks to months but can fluctuate by ± 5 cm in that same time period (*Aishlin et al.* in prep). The magnitude and variability of AT offsets are small compared to changes due to natural hydrologic events (e.g., rain, changes in water table elevation, or seasonal drying) or experienced during the test (*Aishlin et al.* in prep). Uncertainties in AT offsets are later incorporated into the test modeling as instrument errors expressed in the data covariance.

Soil moisture at the BHRS has been measured using a CPN 503DR Neutron Hydroprobe at several access tubes located across the site (Chapter 2). From the summer of 2010 until January 2012, vertical profiles of the entire vadose zone were collected at 2 wk intervals at each of the five access tubes. Moisture data show strong seasonal trends of dry soil during hot, dry summer months and wetter soil during cooler, wetter months from fall through spring (*Johnson et al.* 2013b). Two neutron sites were monitored during the experiment at 1 hr intervals: NX5B is located within the infiltration test area and NX5A is nearby to provide a control (Figure 3-1 inset).

3.2.2 Preliminary Work

Tensiometer nests TX5BD (deep) and TX5BS (shallow) and neutron access tube NX5B were installed in the spring of 2011 at a location consisting of heterogeneous stratified material. Large-scale structure was interpreted from analysis of high-resolution GPR data collected in the summer of 2010 which identified a sand channel aligned east-

west with lateral dimensions of approximately 5 m by 3 m, and thickness ranging from 0.2 – 0.5 m (Figure 3-2) with thinning to the southeast. The channel lies between coarser, mixed sand-cobble materials above and below. TX5BD, TX5BS, and NX5B were installed along the long axis of this channel with a horizontal spacing of 1 m between each installation (Figure 3-1 and Figure 3-2).

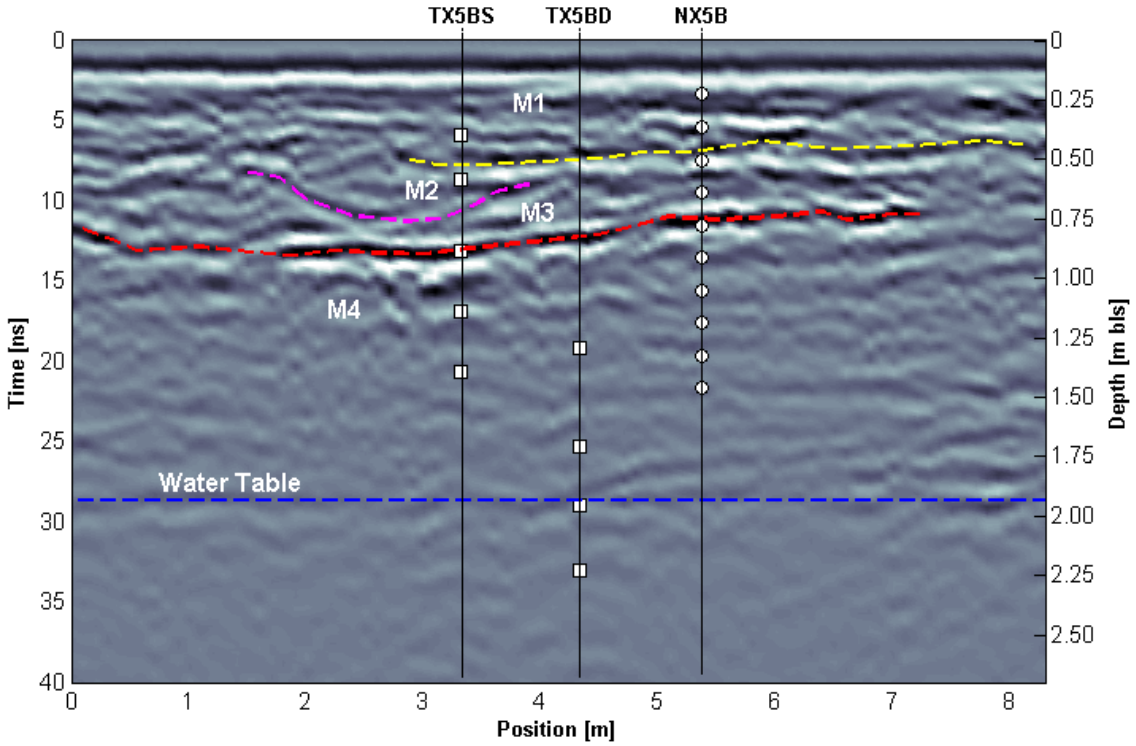

Figure 3-2: 2D GPR radar survey along long axis of channel showing reflections associated with distinct sediment transitions inferred as a depositional sand channel (dashed lines) and locations of TX5BS and TX5BD ATs (squares) and moisture measurements (circles).

Prior to installation of TX5BD and TX5BS, soil cores were extracted at these locations. Cores were separated into material samples based on visual composition breaks or, for longer sections where no clear breaks could be identified, into 15.25 cm (6 in) samples. Core samples were sieved with mesh diameters (*d*) between 190 mm and 0.0625 mm (in the method of *Reboulet and Barrash* 2003) to develop grain size distributions and

to characterize soil type (Figure 3-3). The maximum sampled grain size of these cores was limited by the diameter of the core sample (15.25 cm) but large cobbles (d > 20 cm), which constitute a major portion of the aquifer material, are ubiquitous and underrepresented by this method. Most samples ranged from 50 to 70% by weight gravel or cobble (d > 2 mm) with almost no material of silt or finer size (d < 0.0625 mm), and were characterized as mixed sand/gravel. Three samples were dominantly sand; of these, sections 5S0203 (z = 0.86 – 0.91 m bls) and 5D0202 (z = 0.73 – 0.91 m bls) from tensiometer nests TX5BS and TX5BD, respectively, were classified as fine-medium sand (80% < 2 mm) and contained only small amounts of silt (< 5 %) and gravel (< 15 %). Section 5S0202 (z = 0.66 – 0.86 m bls) from TX5BD was classified as coarse sand and contained ~20% gravel. No similar material to 5S0202 was identified in cores from TX5BS. The depths of these sand samples were all between 0.7 m and 1.0 m below land surface (bls), which corresponds to the depth of the sand channel identified from the GPR data. Similar materials from 5S0203 and 5D0202 were interpreted as a continuation of the same unit but 5S0202 was interpreted as a local lens, which is confirmed by the GPR data (Figure 3-2). Core analysis and stratigraphy from TX5BS were used to determine material distributions for the unsaturated flow model (discussed later).

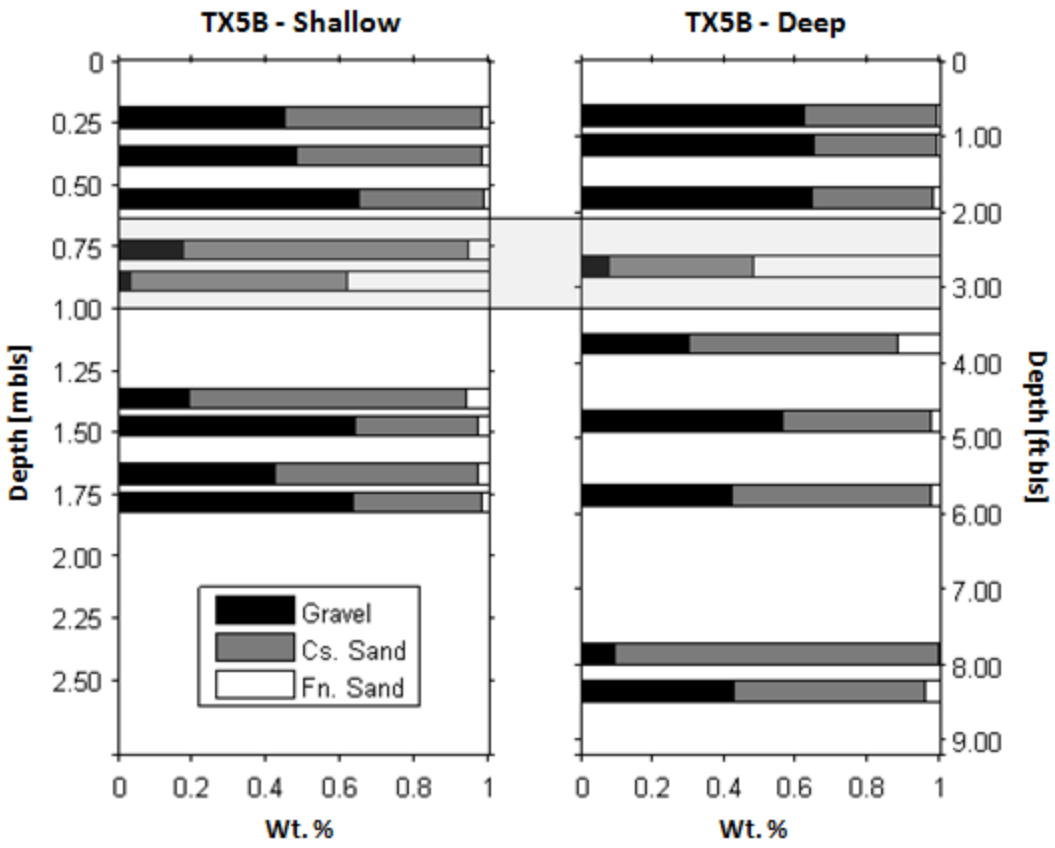

Figure 3-3: Grain size classification of TX5BS and TX5BD core samples: Gravel (d > 2 mm), Cs. Sand (d > 0.25 mm), Fn. Sand (d < 0.25 mm). Shaded regions indicate intervals of sand channel.

3.2.3 Pre-Test Simulation

Prior to the field experiment, HYDRUS 1D was used to simulate infiltration and provide first-order estimations of optimal rain application rate (P [cm hr^{-1}]) and the time required to reach steady-state with continuous flow through the entire vadose zone. The simulation model was set up as a 1D vertical model consisting of three material layers based on GPR data and soil core analysis: material 1 (M1) – mixed sand/gravel; material 2 (M2) –sand; and material 3 (M3) – mixed sand/gravel. The VGM models (Equation 3-1 thru 3-4) were used for θ, ψ, and K relationships

$$\theta(\psi) = \theta_R + \frac{(\theta_S - \theta_R)}{\left[1 + |\alpha\psi|^n\right]^m} \tag{3-1}$$

$$K(\theta) = K_S S_e^l \left[1 - \left(1 - S_e^{1/m}\right)^m\right]^2 \tag{3-2}$$

where

$$S_e = \frac{\theta(\psi) - \theta_R}{\theta_S - \theta_R} \ , \tag{3-3}$$

$$m = 1 - 1/n \ , \tag{3-4}$$

θ_R [-] is residual moisture content, θ_S [-] is saturated moisture content, α [cm^{-1}] and n [-] are empirical parameters that are linked to capillary height and pore size distribution, respectively, but often are treated as shape parameters, K_s [$cm\ s^{-1}$] is saturated hydraulic conductivity, and l [-] is related to soil pore tortuosity but is often assumed a constant value of 0.5 for most tests (*Simunek et al.* 2005), or assumed to be far less sensitive than other parameters (*Abbasi et al.* 2003). Although other mathematical formulas have been established for $\theta(\psi)$ and $K(\psi)$ relationships (e.g., *Brooks and Corey* 1964), I exclusively use the VGM relationships because they are widely used, are continuous functions, and perform well in the modeling used below.

Material properties of M1 and M3 for the test simulation were estimated from $\psi(t)$ data collected in TX5A during natural rain events in December 2010, and for M2 from lab infiltration experiments conducted on sand core sample 5D0202 (both methods discussed below). The simulation model was used to aid in test design, and to confirm

that desired P would not exceed saturated hydraulic conductivities (i.e., no ponding above any layers) and would reach steady-state in an acceptable length of time. These simulations indicated that a rate of P = 1 cm hr^{-1} would require ~24 hrs to reach steady-state and would be sufficient to allow continuous flow through the entire vadose zone at rates less than the minimum K_s of any of the layers. This optimal P is much higher than average storms for the Boise area but is not uncommon for high-intensity storms which are more likely to produce flooding and other hazardous conditions, although such storms never exceed a few hours in duration in the Boise area.

3.2.3.1 Winter 2010 Rain Modeling

In December 2010, several rain events produced observable $\psi(t)$ responses in TX5AS and TX5AD, both of which are near the infiltration test location but outside the wetted perimeter of the experiment. For these events, P was measured at the Boise Agrimet site (see Section 2.2.2) and averaged ~0.25 cm hr^{-1} and storms lasted several hours (Figure 3-4). Data from four ATs between 0.47 and 1.92 m bls were used to estimate unsaturated hydraulic properties of the soil surrounding TX5AS and TX5AD using HYDRUS 1D. 2D GPR reflection surveys collected for a different purpose near TX5AS and TX5AD show a clear, continuous reflection within the vadose zone which was inferred to be a material horizon. This led to the use of a two-layer model for simulation of the December 2010 rain responses with both layers interpreted as mixed sand/gravel, but with different VGM parameter values allowed for each. The observed tension responses from TX5A nests (Figure 3-4) were used to optimize parameters using Monte Carlo sampling along with trial-and-error adjustments. The root-mean squared error between observed and simulated $\psi(t)$ was used to determine optimal parameter

values which are shown in Table 3-1. Final optimal values were within the range expected for sandy soils (for parameters α and n) and BHRS sediments (for parameters θ_S and K_s). In-depth statistical analysis of soil parameters was not performed for these data as the goal of this modeling was to quickly provide initial estimates of vadose zone properties at the BHRS for use in the pre-test simulations.

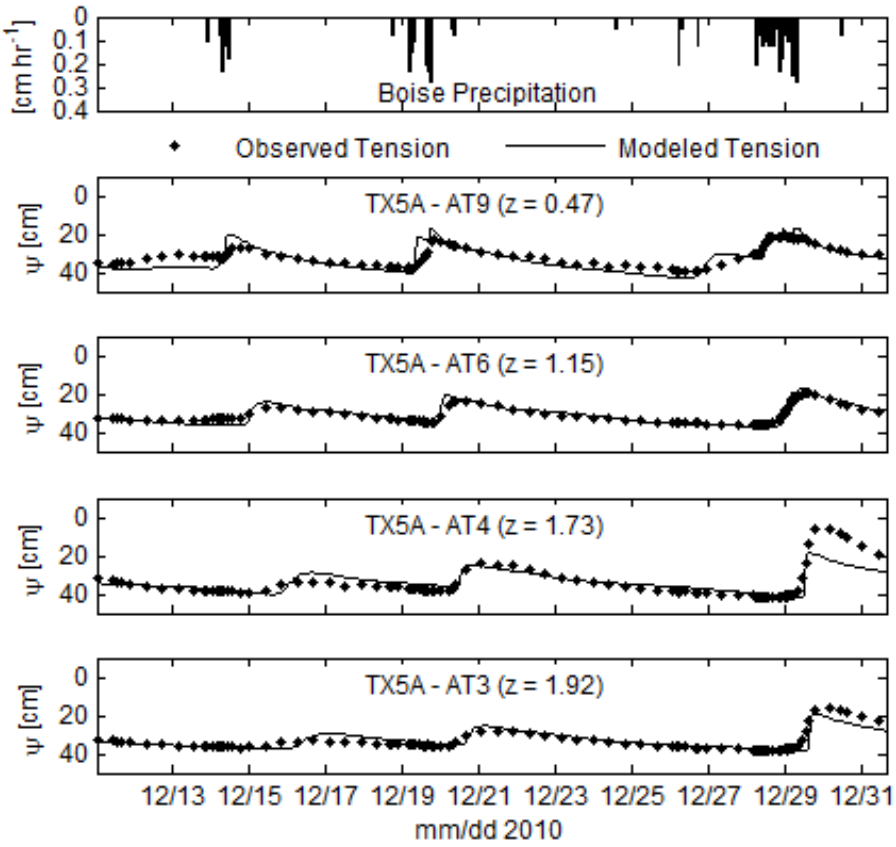

Figure 3-4: Results of modeling the winter 2010 rain events measured in TX5A showing observed and predicted tension responses to several rain events.

Table 3-1: Optimal VGM parameter values from both the winter 2010 rain modeling and core lab tests.

Material	Method	θ_S [-]	α [cm^{-1}]	n [-]	K_s [cm s^{-1}]
Material 1	Winter 2010 Rain Response	0.31	0.22	2.46	0.239
Material 2		0.27	0.22	1.72	0.150
5D0203	Core Lab Test	0.33	0.30	2.96	0.0045

3.2.3.2 Sand Core Properties

The high-resolution GPR reflection surveys conducted over the infiltration site indicated that the fine-medium sand zone did not extend into the area of TX5AD where the December 2010 rain responses were modeled. Correct simulation of the infiltration experiment thus required inclusion of the effects of this distinctly different material. To obtain an initial estimate of parameters, the fine-medium sand core sample (5D0203) was repacked into a 5.08 cm ID clear PVC tube, compacted to a length of 16 cm to achieve approximately the same volume as the original core sample, and placed under an array of greenhouse misters. The top of the core was left open and the bottom was supported with a fine mesh screen. Water was applied to the top of the tube at a rate of P = 5 cm hr^{-1} for ~1 hr, and the times when the wetting front arrived at five chosen vertical locations along the length of the tube were measured. Initial θ was assumed to be near zero for the oven dried sample, and final θ was determined by the weight of the wet soil column minus the dry sample weight (final $\theta \approx 0.36$). Core porosity was estimated from the volume of the dry material (assuming material density of 2.6 g cm^{-3} for quartz sand) divided by the volume of the intact core. Estimated porosity was 0.41, which is within the range of porosity estimates of BHRS sand zones (*Barrash and Clemo* 2002).

Parameter values for the core material were initially determined using the Rosetta Neural Network Prediction module (*Rosetta* 1999) built into HYDRUS 1D with inputs of

%sand, %silt, and %clay (85, 15, 0, respectively) and a bulk density of 1.45 g cm^{-3} as measured from the sample dry weight divided by the core volume. θ_S (i.e., effective porosity) predicted from Rosetta was within 0.01 of the estimated porosity (0.41) and parameter values predicted by Rosetta were used in HYDRUS 1D to simulate the wetting front propagation along the column. The model top boundary was set as a specified flux equal to 5 cm hr^{-1} and a free drainage boundary was prescribed at the bottom. The model-predicted times when the wetting front passed five locations (t_{wf}) were compared to the actual times measured in the lab. Calculated t_{wf} using the Rosetta-predicted values were all within 4 min of the observed t_{wf} at all measurement locations (Figure 3-5) with a correlation coefficient (R^2) of 0.98. These Rosetta-predicted parameter values (Table 3-1), though representing properties of a reconstructed core and not in situ properties, were used in the pre-test simulation and also to provide a starting point for optimization of the infiltration test. As with the December 2010 modeling, an extensive analysis of the parameters was not performed as it was not the focus of this experiment.

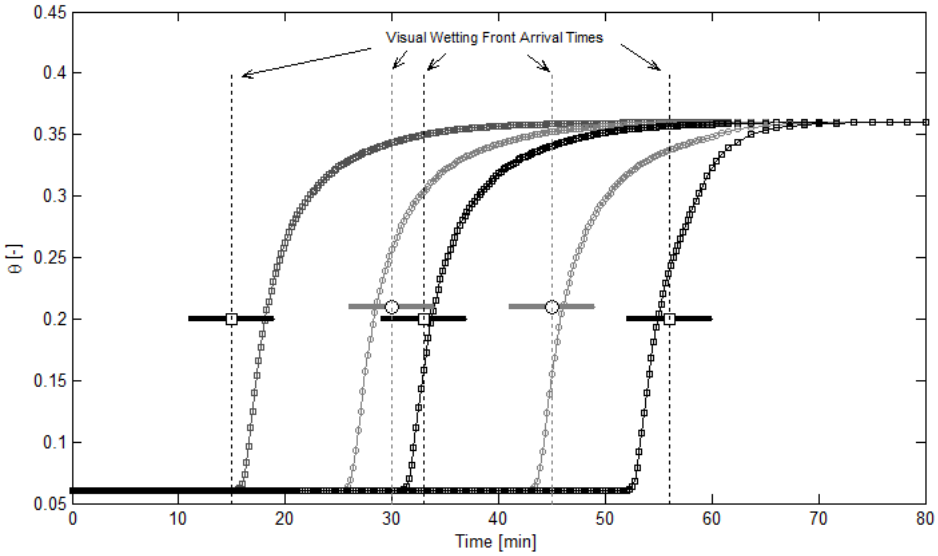

Figure 3-5: Calculated wetting curves at observation nodes and observed wetting front times from the sand core rain test performed on core sample 5D0203; tick bands show ± 4 min error.

3.3 Field Infiltration Experiment Setup

A 5 m by 2 m area surrounding installations TX5BS, TX5BD, and NX5 was used for the infiltration test (see Figure 3-1 inset); these dimensions allowed for wetting to surround the area of all three installations by ≥ 1 m. During the experiment, the infiltration site was covered with waterproof canopies and surrounded with waterproof tarps to minimize effects of evaporation and wind redistribution. Water was applied using 66 Agrifirm 0.5 GPH Turbo-Flo® Mist Nozzles placed 1.5 m above the land surface in a staggered grid pattern (0.5 m between misters on a single row and 0.35 m between rows) to provide optimal coverage. There are several advantages to using these mist nozzles over more conventional sprinklers or drip-lines: 1) small droplet size minimizes impact effects; 2) they can be placed at any height above the land surface, which allows for access beneath the misters and direct measurements of *P* at the soil surface; 3) the application rate can be easily adjusted by changing either the incoming water pressure,

the nozzle height above ground, or nozzle spacing; 4) nozzles are interchangeable and available with different flow rates, allowing for further range of application rate; and 5) they are inexpensive and can be obtained from most irrigation supply distributers. Precipitation rate was measured using four tipping buckets, calibrated prior to and after the experiment, placed on the land surface within the application area, and connected to a Campbell Scientific CR1000 data logger. Water supplied to the misters was extracted from well C6 which is 35 m from the infiltration site. With the low pumping rate (< 5 gal hr^{-1}), fully-screened well, and high K_s aquifer, water table drawdown (Δwt) near the infiltration site caused by pumping was not measurable (Δwt < 0.01 ft) during the test.

The infiltration experiment began on the morning of August 1, 2011 at 1130 MDT. Campbell Scientific CR1000 data loggers were used to record ψ in tensiometer sets TX5A and TX5B with a measurement frequency of 3 min, and full vertical θ profiles were collected every 1 hr in NX5A and NX5B. NX5A and set TX5A (consisting of nests TX5AS and TX5AD) were outside the infiltration area but within 2 m of the perimeter and were monitored to observe background changes in θ and ψ and to confirm that water was not migrating laterally beyond the application area. Water table depth was measured in well X5 (<4 m from the infiltration area) at 4 hr intervals and showed no change throughout the experiment. Tensiometer data were output in real-time to laptops set up in a tent adjacent to the test area to monitor progress. After ~19 hr, it was decided that vertical ψ and θ profiles had reached steady-state under wet conditions (pre-test simulations predicted ~24 hr), and after waiting another 4 hr the misters were turned off at 0721 MDT on August 2. For approximately 11 hr after turning off the misters, all measurements were recorded at the same time intervals and by the evening of August 3,

2011, much of the equipment was removed and θ measurements were expanded to two to three times per day until August 5, 2011. Measurements of ψ continued at 3 min intervals until August 5, 2011. Long-term ψ and θ data later showed that soil moisture did not return to pre-test values until more than 1 wk after rain application ceased.

In addition to hydrologic measurements, 2D multi-offset GPR reflection and 3D dipole-dipole electrical resistivity surveys were collected every hour during the infiltration experiment from August 1, 2011 through August 3, 2011. GPR surveys were collected along the main transect of the installations using shielded antennas and the ends of this transect extended beyond the wetted area (see Chapter 4 for incorporation of GPR data into infiltration test modeling). The resistivity survey also extended beyond the wetted perimeter in order to delimit the wetted perimeter and to observe lateral moisture migration, if any. Initial review of the 3D resistivity and 2D GPR data along with tension measurements in set TX5A and moisture measurements in NX5A (not shown) confirm that there was no observable lateral migration of water outside the application area.

3.3.1 Infiltration Test Results

The four rain buckets recorded recognizably different P within the experiment boundary (Figure 3-6). Buckets 1 and 4 showed mean P of 1.67 and 1.59 cm hr^{-1}, respectively, with standard deviations (σ) of 0.31 and 0.59 cm hr^{-1} while buckets 2 and 3 (the two buckets closest to TX5BS, TX5BD, and NX5B) showed considerably less noise in the measurements (σ < 0.14 cm hr^{-1} for both) and mean P of 0.77 and 0.92 cm hr^{-1}, respectively. Higher σ values from buckets 1 and 4 are likely the result of the buckets being jostled or becoming tilted during the experiment, as they were located closer to the edge of the application plot where there was considerable foot traffic related to

geophysical data collection and other logistics. For that reason, I use a constant *P* of 0.84 cm hr^{-1} (0.00023 cm s^{-1}) determined from the mean of buckets 2 and 3 as the upper boundary flux in the infiltration model since these two buckets were located closest to the measurement locations. Note that this rate (0.00023 cm s^{-1}) is far less than the previously estimated K_s of any of the materials (Table 3-1) but is still much greater than natural precipitation rates and durations (e.g., events described in the winter 2011 modeling section). This was an essential part of the experiment: to avoid oversaturation of sediments and ensure continuous flow through all layers.

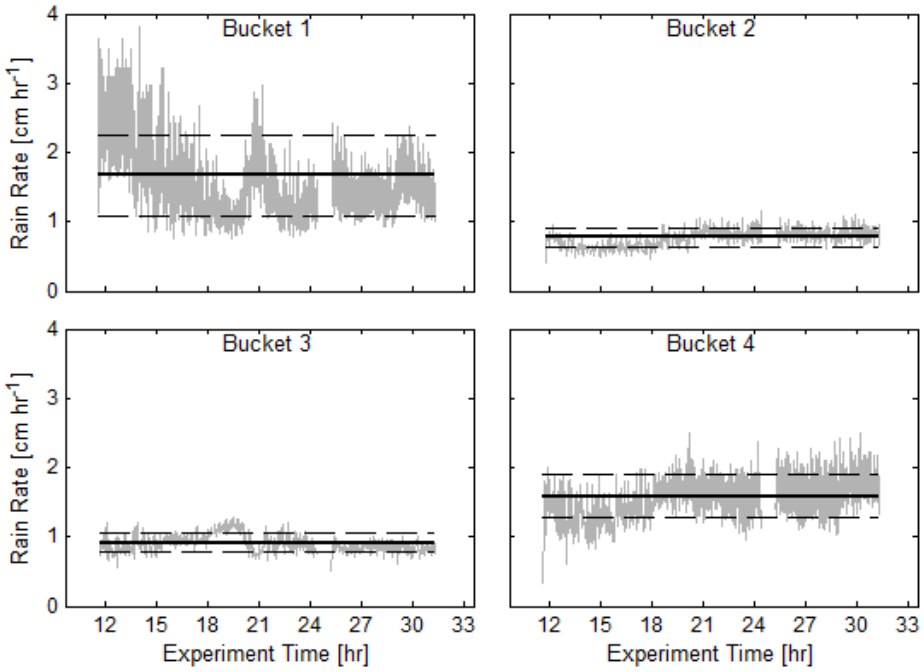

Figure 3-6: Rain application rate from the four rain buckets, solid lines, and labels are mean values and dashed lines are ±σ from all data.

Measurements of θ were taken in NX5B and NX5A from 0.15 m bls to just above the water table (~1.5 m bls) with vertical spacing of 0.15 m (0.5 ft). Four $\theta(z)$ and $\psi(z)$ profiles from selected times during the experiment are shown in Figure 3-7. Figure 3-7A shows initial $\theta(z)$ and $\psi(z)$ profiles and Figure 3-7D shows the first measurements after

steady-state was reached and prior to ending rain application. Long-term $\psi(t)$ and $\theta(t)$ data from the beginning of the experiment until several days after are shown together in Figure 3-8 for different tensiometer depths and comparable θ measurement depths (vertical differences between ψ and θ measurements in Figure 3-8 are less than 20 cm). Raw $\psi(t)$ data prior to and during the arrival of the wetting front had a σ of ~2 cm for all tensiometers but $\psi(t)$ data after steady-state had been reached became noisier and σ values increased to 12 – 14 cm for all tensiometers except AT7 and AT9. All $\psi(t)$ data were processed by averaging each data point with the previous and following points (3 measurements or 9 min window) to reduce noise. This averaging reduced σ for $\psi(t)$ data to near 2 cm for all tensiometers but did not significantly affect the timing of the arrival of the wetting front nor the shape of the transient portions of the $\psi(t)$ curves. ψ(t) measurements at AT7 are not included in the results or in the modeling due to questionable behavior prior to the start of the experiment, likely related to a damaged AT sensor or housing.

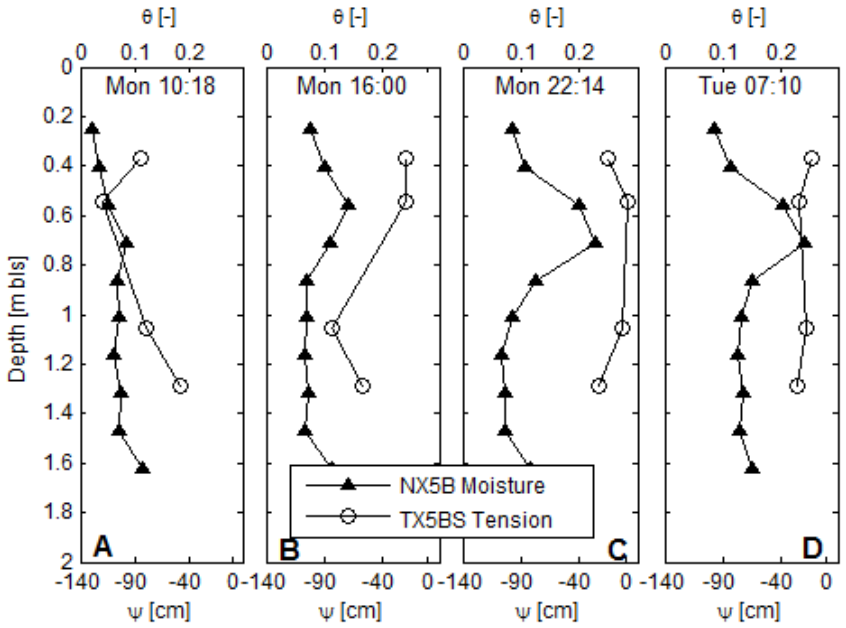

Figure 3-7: ***θ*(*z*) and *ψ*(*z*) profiles at select times during the experiment: A) initial profiles, B and C) during the test, and D) steady-state.**

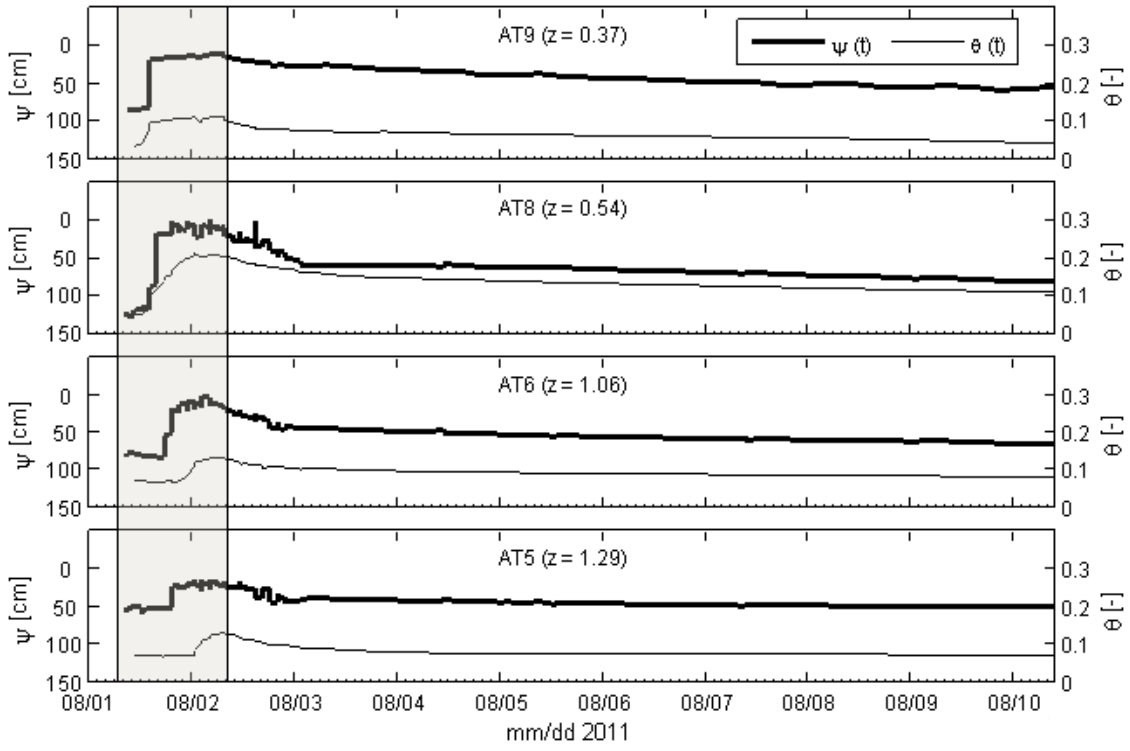

Figure 3-8: Observed *ψ*(*t*) and *θ*(*t*) data from the beginning of the experiment to 10 d after; moisture data presented are from measurement depths nearest to AT depths in NX5B; shaded region denotes modeling focus time.

Comparison of wetting front arrival times between $\psi(t)$ and $\theta(t)$ shows that there was a significant delay (~6 hr) in the $\theta(t)$ responses at depths of sensors AT6 and AT5 compared to the $\psi(t)$ responses (Figure 3-8), which is much more of a delay than would be expected by differences in depths between the two sets of measurements (< 20 cm). Although not shown, $\psi(t)$ data recorded in AT4, located slightly above AT5 but 1 m closer to NX5B (see Figure 3-2), are also delayed in arrival of the wetting front compared to AT5 by ~3.6 hrs. I suspect the progressively greater delay is due to lateral variation in material M3 thickness between TX5BS and NX5B (see Figure 3-2) since AT6, AT5, and the corresponding θ measurements are located below the fine-medium sand layer observed from core samples and GPR data. GPR data along with core samples from TX5BS and TX5BD show that the fine-medium sand section is 7 – 12 cm thicker at TX5BD than at TX5BS and that the medium-coarse sand section (5S0202) is completely absent at the location of NX5B. The variable thickness of the fine-medium sand zone between TX5BS and NX5B combined with the lower K_s of this material (see Table 3-1) are likely causing the delay in wetting front propagation between TX5BS and NX5B. The significant difference in response times between ψ and θ data at similar depths excludes the use of simpler methods of optimizing VGM parameters through direct fitting of observed $\theta(\psi)$ data as other studies have done (e.g., *Milczarek et al.* 2006; *Vrugt et al.* 2003a).

3.4 Infiltration Test Model

Albeit with recognition of the apparent lateral heterogeneity described in the previous paragraph, I modeled the infiltration experiment over TX5BS using the HYDRUS 1D model as a first approximation and base case to compare with more

detailed modeling to follow (which will include 2D distribution of materials and geophysical data). Because the heterogeneity limits the use of simultaneous ψ and θ data in a 1D model to optimize parameters, I focused on fitting $\psi(t)$ data from TX5BS and include only an initial θ measurement (prior to the start of the test: θ_{dry}) and final θ measurement (after the wetting front had passed and steady-state flow had been reached: θ_{wet}) for three θ measurement depths corresponding to separate material layers. Tension data were chosen as the primary data to fit because they provide a sharper transition from dry to wet conditions, and thus a better representation of the wetting front arrival than moisture data, and tension data errors are smaller relative to total change in tension than moisture data. Including only θ_{wet} and θ_{dry} was done to achieve better representation of the soil properties because it forces the model to find curves that pass through $\theta(\psi)$ points of the initial and steady-state observations, thus providing further constraint. In this regard, *Zou et al.* (2001) have shown that including only initial and final moisture measurements in wetting experiments can increase parameter predictability.

Material distributions for the infiltration test model were similar to the pre-test simulation model except that the infiltration test model was separated into four material layers instead of three; in addition to a fine-medium sand layer, the infiltration model included a coarse sand with gravel layer represented by core sample 5S0202 (Figure 3-9). The model geometry extended from the land surface (z = 0 cm) to z = -300 cm with material contact depths determined from GPR data and core samples (Figures 3-2 and 3-3). M1 and M4 both represent coarse, poorly-sorted, mixed sand/gravel/cobble; M2 represents medium-coarse sand with gravel (e.g., core section 5S0202); and M3 represents a uniform medium-fine sand (core section 5S0203). The model was discretized

with elements ranging in thickness from 0.54 cm to 5.4 cm and with finer discretization around M3. Initial model time (t_0) was August 1, 2011 00:00 MDT and the model was run for 24 hr, which was adequate time to reach steady-state. Time step discretization is internal to HYDRUS 1D software and is continuously adjusted to achieve convergence (*Simunek et al.* 2005). Final mass balance errors were, on average, less than 3% for all model runs.

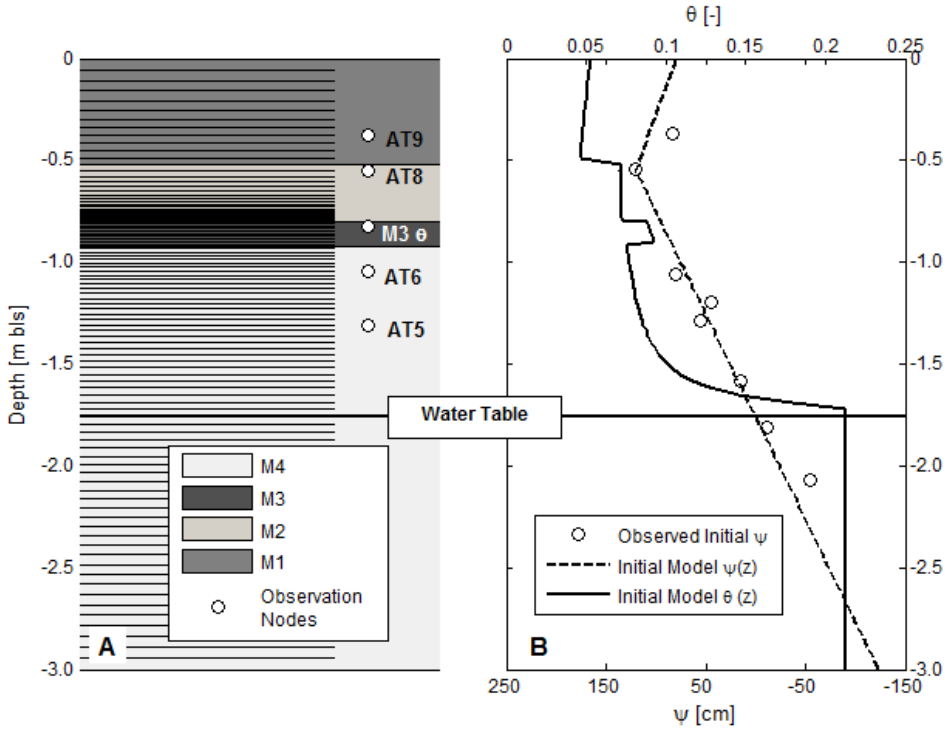

Figure 3-9: A) HYDRUS 1D model setup showing material distribution, grid discretization, and locations of measurement nodes; B) initial model ψ and θ profiles and initial observed ψ data (circles) prior to test.

Initial conditions of the model were set using the observed water table depth as ψ = 0 cm at z = -176 cm and measurements from the tensiometers immediately prior to the experiment to calculate a ψ(z) relationship from the water table to the land surface. Observed ψ increased (decreasing negative pressure) above the water table to the depth of AT8 (-55 cm) then decreased slightly between AT8 and AT9. Below the water table, ψ(z)

was set to a 1:1 function with increasing positive pressure equal to hydrostatic pressure. Initial $\theta(z)$ values were set automatically based on initial VGM parameters for the four different materials and the initial tension profile. Observation nodes were placed at depths corresponding to AT9, AT8, AT6, and AT5 with an additional observation node placed within material M3 to track θ in that material. Two nodes used for AT9 and AT5 were used to track θ in M1 and M4.

The upper model boundary was set as a variable flux boundary with P = 0.84 cm hr^{-1} (mean of rain buckets 2 and 3) for the time of rain application (from +11.6 hr to +24 hr model time) and P = 0 cm hr^{-1} otherwise. The lower boundary was set as a head-dependent flux boundary with a critical head value of 124 cm (the height of the water table above the base of the model). This condition maintains a constant water table depth and represents water being dispersed laterally upon reaching the saturated zone (i.e., no recognizable mounding).

3.4.1 Metropolis-Hastings Optimization

Optimization of VGM parameters was achieved using five independent Metropolis-Hastings (MH) sampling algorithms, with five separate initial parameter sets, each run to 10^6 samples. The MH algorithm was similar to the method described by *Cardiff et al.* (2011); below I provide a brief description of the process but refer the reader to *Cardiff et al.* (2011) for further details. The MH algorithm is a Markov Chain Monte Carlo (MCMC) type method that seeks to generate a set of samples (the Markov Chain) that is representative of the model parameters' posterior probability density. MCMC methods are advantageous for modeling in the vadose zone because models of vadose zone behavior (e.g., Richards' Equation (*Richards* 1931) and VGM relationships)

are strongly non-linear and parameters are often highly correlated, which can complicate gradient-based optimization methods (*Vrugt et al.* 2003b; *Vrugt and Bouten* 2002). The MH algorithm incorporates a downward-stepping function that always accepts parameter sets that produce higher likelihood (better fits to data), but also accepts parameter sets of lower likelihood with a certain probability. The former ensures that "peaks" of the parameters' posterior probability are discovered, while the latter allows the algorithm to explore the full parameter space and rigorously estimate parameter uncertainty. I use the MH algorithm over recently developed shuffling algorithms (*Vrugt et al.* 2003b; *Wohling and Vrugt* 2008) because the MH algorithm is statistically sound, readily available, and does not require complicated parallel computing.

The MH algorithm explores the parameter likelihood or, equivalently, the negative log likelihood (*NLL*) function

$$NLL = \frac{1}{2}\left[{d_{err}}^{T} \cdot {C_d}^{-1} \cdot d_{err}\right] \tag{3-5}$$

where d_{err} is a vector of the error between the observed and calculated data (for both $\psi(t)$ and $\theta(t)$) and C_d is the data covariance matrix, a diagonal matrix with elements equal to the estimated error, or variance (σ^2), of the data. For tension measurements, observed data error (σ_ψ) was only 2 cm but this incorporates measurement error only. Given the additional uncertainty in AT depths and material depths, as well as AT offsets mentioned earlier, σ_ψ for C_d was increased to 8 cm to incorporate all errors. For θ measurements, observed σ_θ is 0.03 based on instrument precision (*Johnson et al.* 2013b) but I used a value of twice this amount in C_d to account for uncertainty in measurement depth and sampling volume influences of the neutron data. The d_{err} vector included ~100 data

points (300 min) for each of the four ATs in TX5BS with the data centered on the times when the wetting front passed each sensor, as well as θ_{dry} and θ_{wet} for each of three materials: M1, M3, and M4 (observation nodes AT9, M3θ, and AT5 in Figure 3-9, respectively). Selection of $\psi(t)$ data in this manner eliminates large amounts of redundant and non-transient data in the optimization. The choice of θ_{dry} and θ_{wet} is described above.

VGM parameters θ_S, α, n, and K_s were optimized for each of the four materials. θ_R was set to a fixed value for each of the material layers based on the measured moisture content prior to the test (0.03 – 0.05 for all materials) since θ_R has been shown to have low identifiability in similar modeling experiments (*Inoue et al.* 1998; *Scharnagl et al.* 2011; *Simunek et al.* 1998). The starting point (initial parameter set) for the MH sampling was obtained from the results of a direct search (DS) optimization using the MATLAB *fminsearch* function. Direct search methods have been recommended by *Liu et al.* (2010) to be done prior to MH methods to provide a better starting position. Initial values for the DS optimization were obtained from the winter 2010 rain modeling for M1 and M4, and results of the lab core experiment for M3. M2 initial values for the DS method for α and n were prescribed to that of M3 (similar relatively fine material), and θ_S and K_s were set to values typical of BHRS sand layers (*Barrash and Clemo* 2002; *Barrash et al.* 2006). The DS optimization reduced the *NLL* from an initial value of 465 to 223. While the DS method did not provide very good fits to observed $\psi(t)$ and θ data, the results did provide a better initial state for the MH sampling.

The robustness of MH methods comes from the use of a large number of iterations to explore the parameter space, which makes MH algorithms computationally intense and time consuming. The larger the number of iterations (as t approaches ∞) the

more likely the algorithm is to find the optimal parameter set and the better it will predict parameter variance and joint probability density functions. *Liu et al.* (2010) and others discuss how results from a single MH chain are often insufficient in identifying optimal parameters and estimating variance and suggest that multiple chains, starting from different initial parameter sets, are better at searching the entire parameter space and achieving convergence. The first MH chain (MH_1) was started with the initial parameter set taken from the results of the DS optimization mentioned above. For the remaining chains (MH_2 through MH_5), the initial sets were chosen by picking four parameter sets from within uniform distributions, within reasonable bounds, such that the calculated initial *NLL* of the chosen set (Table 3-2) was < 1.5 times the *NLL* of the DS results.

Table 3-2: Initial parameters used in all five MH sampling runs and lower and upper bounds.

		θ_S [-]	α [cm^{-1}]	n [-]	K_S [cm s^{-1}]
M1 sand / gravel	MH_1	0.31	0.22	2.46	0.239
	MH_2	0.23	0.32	2.57	0.064
	MH_3	0.20	0.24	3.54	0.018
	MH_4	0.34	0.27	1.66	0.312
	MH_5	0.23	0.16	1.79	0.108
	Bounds	[0.15 - 0.35]	[0.04 - 0.5]	[1.0 - 4.0]	[0.002 - 0.6]
M2 cs. sand + gravel	MH_1	0.15	0.22	3.29	0.055
	MH_2	0.15	0.28	2.49	0.250
	MH_3	0.14	0.46	1.55	0.058
	MH_4	0.14	0.28	1.51	0.493
	MH_5	0.12	0.40	1.87	0.240
	Bounds	[0.10 - 0.40]	[0.04 - 0.5]	[1.0 - 4.0]	[0.002 - 0.6]
M3 uniform fine-med sand	MH_1	0.33	0.30	2.96	0.0045
	MH_2	0.37	0.12	1.38	0.044
	MH_3	0.44	0.16	3.96	0.0086
	MH_4	0.48	0.27	1.50	0.067
	MH_5	0.35	0.15	1.66	0.0033
	Bounds	[0.20 - 0.50]	[0.04 - 0.5]	[1.0 - 4.0]	[0.0003 - 0.6]
M4 sand/gravel	MH_1	0.27	0.22	1.72	0.150
	MH_2	0.19	0.25	3.24	0.089
	MH_3	0.20	0.13	3.09	0.294
	MH_4	0.30	0.26	3.51	0.240
	MH_5	0.35	0.13	3.55	0.246
	Bounds	[0.15 - 0.35]	[0.04 - 0.5]	[1.0 - 4.0]	[0.002 - 0.6]

The size of the steps taken between successive samples in the MH algorithm, or search radius, was determined by the parameter covariance matrix (C_m) which is a measure of the local σ^2 of each parameter and the covariance between parameters (*Tarantola* 2005). Parameters that have larger σ^2 will allow the MH sampler to take larger steps in that direction, which will more quickly explore the parameter space of less resolved parameters. The C_m matrix was estimated from

$$C_m = \left[J^T \cdot C_d \cdot J \right]^{-1} \tag{3-6}$$

where J is the numerical finite-difference Jacobian matrix evaluated at the current parameter set and C_d is the data covariance matrix as in Equation 3-5. In the five separate MH chains, C_m was updated every 10^5 iterations using the latest parameter set to ensure a more efficient search of the parameter space as the MH algorithm evolves.

Prior information can be incorporated into the MH algorithm by several methods (*Liu et al.* 2010) but given the nature of the infiltration experiment and associated information, I chose to enforce bounds to all parameters (Table 3-2) based on what has been observed at the BHRS for saturated parameters θ_S and K_s, or what is likely for coarse materials for unsaturated parameters α and n. Any parameter set that had one or more parameters outside these bounds returned an *NLL* well above values expected from in-range parameters. The average number of out-of-bound samples for the five separate chains was between 45% and 65%.

3.4.2 Potential Scale Reduction Factor

A scale reduction (*SR*) factor is used as an unbiased assessment of whether multiple MH chains have converged upon a single distribution (*Gelman and Rubin* 1992; *Liu et al.* 2010; *Vrugt et al.* 2003a). From *Gelman and Rubin* (1992):

$$SR = \sqrt{\frac{1-g}{g} + \frac{q+1}{q}\frac{B}{W}} \tag{3-7}$$

where g is the number of samples used, q is the number of independent chains, W is the mean of all σ^2 values from each independent chain, and B is the variance of all μ values

from each individual chain. The *SR* should reduce with evolution of the chains as each chain samples through the parameter space and statistical aspects of individual chains become similar to aspects of all chains combined (*Liu et al.* 2010). If multiple chains converge to the same parameter space with similar statistical properties, *SR* will approach 1 and the chains are said to have converged. But, as this is unlikely with uncertainty in the data, *Gelman and Rubin* (1992) suggest that a value of 1.2 is sufficient to declare convergence. I calculated *SR* with all five MH chains beginning at step $5x10^5$ and continuing to step 10^6 and I discuss the results below.

3.5 MH Results and Parameter Distributions

Probability distributions for each parameter from each of the five MH chains are shown in Figure 3-10 along with the distributions from the set of all five chains combined (MH_{all}). Parameter mode (*Mo*) and standard deviation (σ) values from MH_{all} are presented in Table 3-3 along with calculated final *SR* (after 10^6 samples). These calculations and distributions disregard the first $5x10^5$ samples as a "burn-in" period. Final *SR* for 11 of the 16 parameters was <1.2, implying convergence between chains had been reached. Initial *NLL* values from the five independent chains were: 223, 256, 232, 232, and 279 but after the first $3x10^5$ samples, *NLL* was reduced to < 45 for all chains and remained primarily between 15 and 35 for the remaining steps (Figure 3-11). The consistent range of *NLL* values within each chain and similar values between chains after the burn in suggest that all MH chains reached an optimal minimum *NLL* region which could not be reduced further.

Table 3-3: Mode and standard deviation from combined distribution of all five MH chains and Scale Reduction after 10^6 samples.

		θ_S [-]	α [cm^{-1}]	n [-]	K_S [cm s^{-1}]
M1 sand / gravel	Mo_{all}	0.349	0.085	2.567	0.133
	σ_{all}	0.060	0.021	0.285	0.074
	SR	1.58	1.55	1.11	1.67
M2 cs. sand + gravel	Mo_{all}	0.102	0.107	1.016	0.012
	σ_{all}	0.076	0.132	0.649	0.139
	SR	1.03	1.02	1.07	1.03
M3 uniform fine-med sand	Mo_{all}	0.261	0.056	1.468	5e-4
	σ_{all}	0.037	0.136	0.125	0.004
	SR	1.44	1.02	1.07	2.12
M4 sand/gravel	Mo_{all}	0.151	0.381	1.366	0.038
	σ_{all}	0.017	0.096	0.080	0.034
	SR	1.08	1.06	1.10	1.16

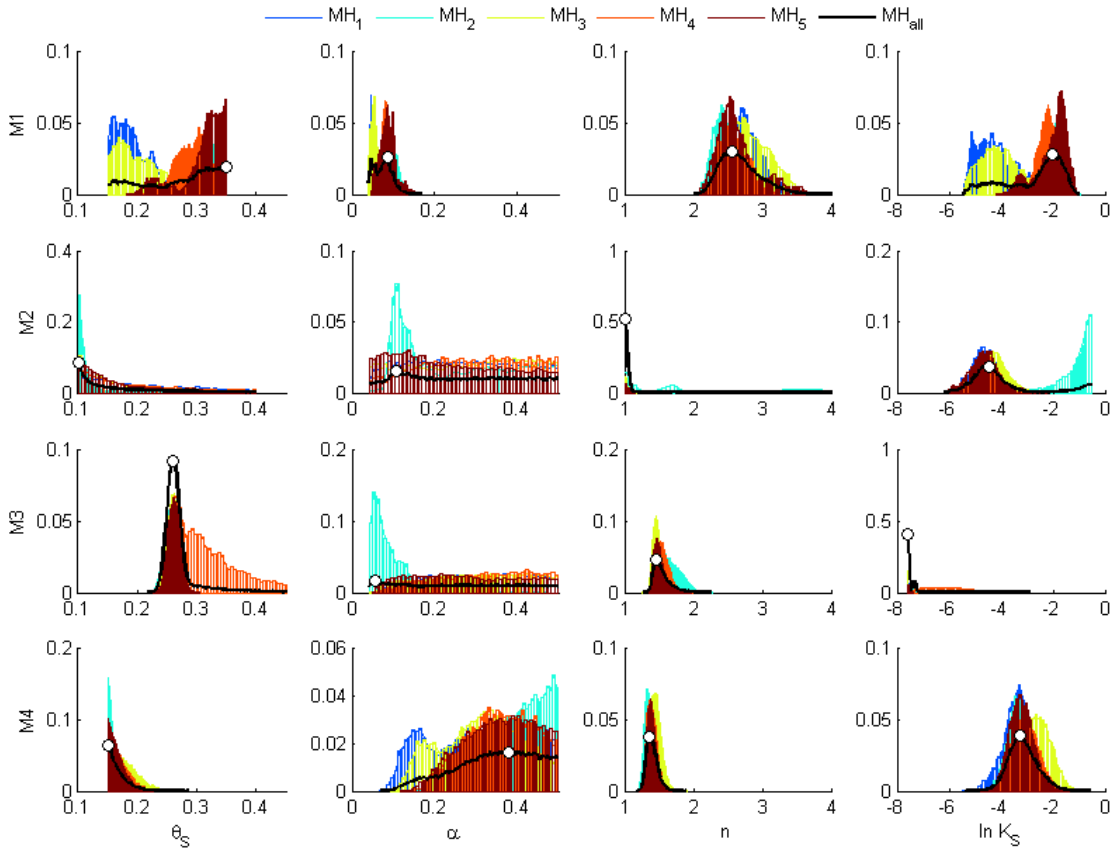

Figure 3-10: Cumulative distributions of parameters from all five independent MH chains and all chains combined (black lines); white circles are mean values from combined chains.

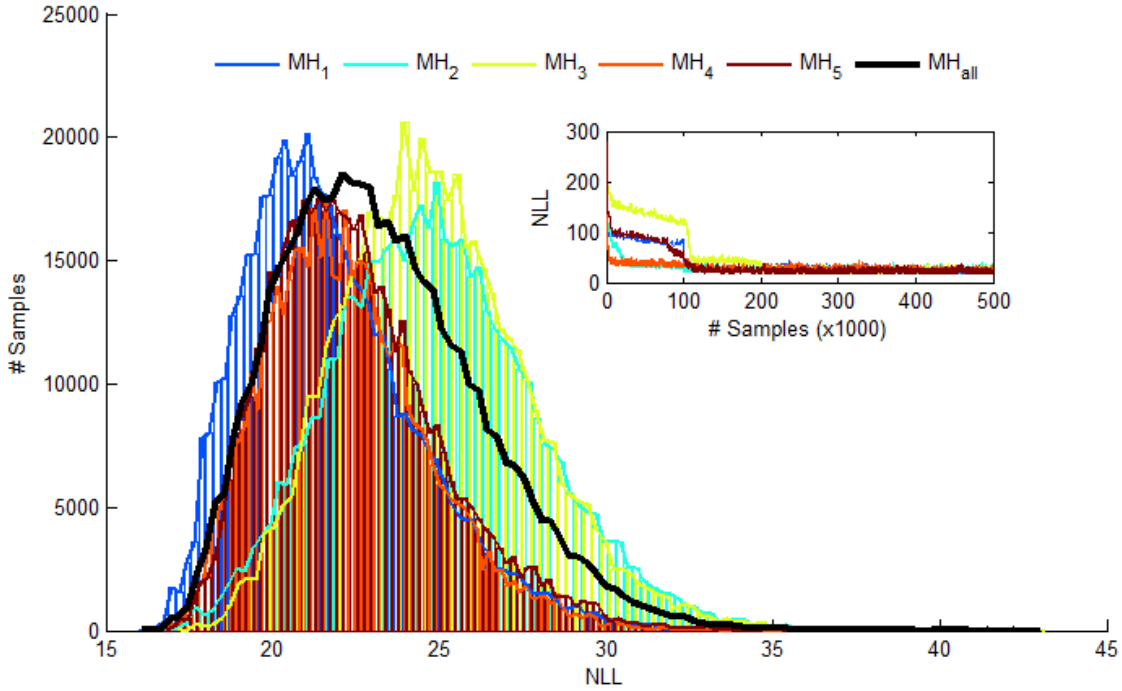

Figure 3-11: Distributions of *NLL* for all five chains excluding burn-in, thick black line is distribution from MH_{all}; inset shows *NLL* evolution of first 500K samples from individual chains including burn-in.

Important observations about the resolution of parameters and the sensitivity of the experiment and forward model to parameters can be made from the parameter distributions in Figure 3-10 and σ values in Table 3-3. 1) Several parameters appear to have converged to distributions that were near normal with clearly identifiable *Mo* values ($\theta_{S,M3}$, n_{M1}, n_{M3}, n_{M4}, $K_{S,M2}$, $K_{S,M4}$) implying convergence between chains and high resolution of those parameters with clear optimal values. 2) Distributions for $\theta_{S,M1}$, $K_{s,M1}$, and α_{M4} show little agreement between individual chains (little overlap) leading to wide distributions (high σ) for MH_{all}, which is quantified by *SR* >1.5 for all three parameters and indicates non-uniqueness. 3) Some distributions ($\theta_{S,M2}$, $\theta_{S,M4}$, $K_{S,M3}$) were strongly affected by the bounding values, which implies that optimal values may be outside the bounds (i.e., θ_S <0.15). As described above, these bounds were based on saturated tests performed in this region of the aquifer. As I will discuss below, this is likely related to

resolution of parameters and sensitivity of the model to those parameters. 4) Parameters α_{M2}, α_{M3}, and α_{M4} each converged to a single distribution ($SR < 1.1$ for all) but these distributions were nearly uniform and are thus uninformative, implying that those parameters have little influence over the model and data fit. Similarly, the fact that σ values are more than four times greater for n_{M2}, n_{M3}, and n_{M4} than n_{M1} (Table 3-3) implies that the model is most sensitive to n_{M1}. More detailed discussion of potential causes and implications of these observations will be made below.

3.5.1 Parameter Covariance and Correlation

It is widely understood that VGM parameters are often highly correlated and cross-correlation, which contributes to non-uniqueness, is ubiquitous in parameter inversion in general. In addition to looking at the 1D distributions of parameters I also looked at marginal (2D) distributions from MH_{all} and calculated correlation coefficients (R^2) between parameter pairs. Figure 3-12 shows marginal distributions from MH_{all} only but trends in distributions and cross-correlation are similar for all individual chains and even subsets of chains (e.g., only samples where $NLL < 25$). Highest R^2 values for parameter pairs within the same material were found between θ_S-K_s in M1, M3, and M4 (R^2 = 0.97, 0.91, and 0.73, respectively), α-n in M1 and M3 (R^2 = 0.74 and 0.69), α-K_s in M1 (R^2 = 0.83), θ_S-n in M4 (R^2 = 0.62), and n-K_s in M2 (R^2 = 0.80). For all other pairs, R^2 values did not exceed 0.6. I show more explicitly in the next section the effects of parameter correlation on the physical aspects of the VGM relationships and data fit.

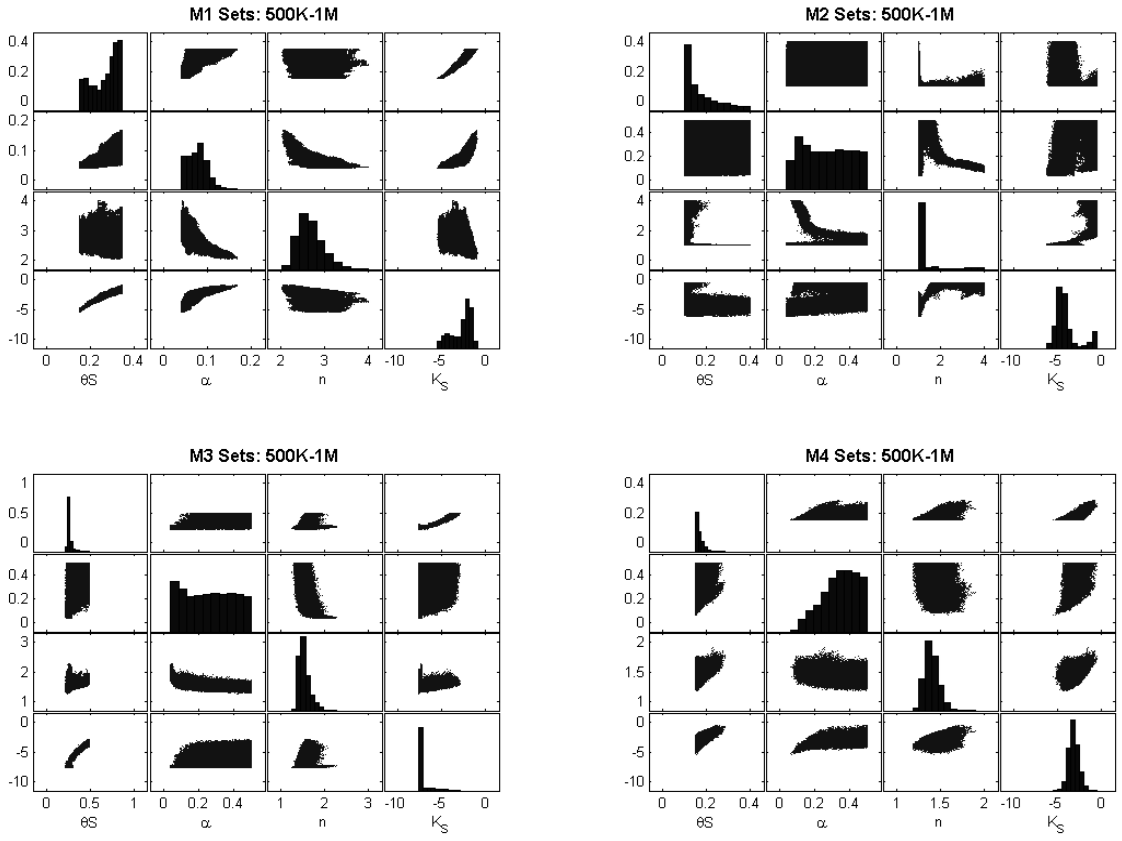

Figure 3-12: Marginal distributions from the full set of all MH chains combined for each material.

3.5.2 Parameter Relationship to Soil Characteristic Curves

Mode values presented in Table 3-3 represent only the most likely set of parameters given the data, the forward model, and the current sampling algorithm. Low *NLL* values despite wide distributions and high R^2 between parameters imply that, for many parameters, there is a range of values that will fit the data equally well. What is controlling the distribution and movement of moisture within the soil, as depicted by the model, is the shape of the VGM $\theta(\psi)$ and $K(\psi)$ functions, and individual parameters can be considered curve-fitting parameters to these functions.

To investigate the effects of parameter uncertainty on uncertainty in the $\theta(\psi)$ and $K(\psi)$ functions, I randomly chose 2000 parameter sets from MH_{all} and plotted 2000

different $\theta(\psi)$ and log $K(\psi)$ characteristic curves for each of the four materials (Figure 3-13). Despite the wide range of individual parameters chosen (σ of sets chosen were similar to σ presented in Table 3-3), we see that the relationships between parameters, whether 2D or higher dimension, combine to produce $\theta(\psi)$ and $K(\psi)$ functions that are representative of realistic VGM functions and, especially for M1 and M4, are unique and informative, with well-defined shapes that are very near curve shapes typical of standard agricultural soils (the clear exceptions being M2 functions, which indicate the model's insensitivity to that material's properties). *Stauffer and Lu* (2012) made a similar inference that curve shapes are more informative than individual parameters (due to parameter cross-correlation), and used this to reduce computation time in unsaturated flow modeling.

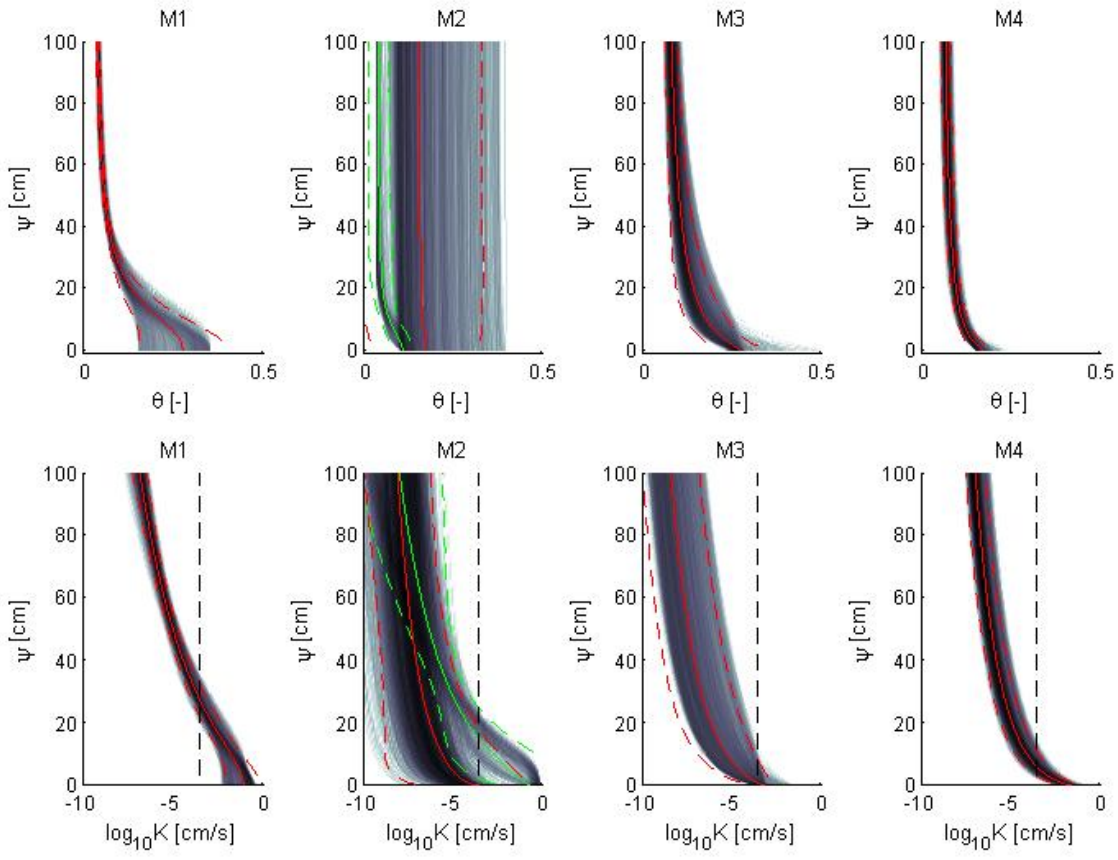

Figure 3-13: $\theta(\psi)$ and $K(\psi)$ curves produced from 2000 randomly chosen parameters sets from MH_{all}; darker shades indicate where more of the curves overlap, solid lines represent mean curve values and dashed lines represent $\pm 2\sigma$; green lines for M2 curves are from MH_2 parameter sets only.

The successful application of the VGM model and the finding that curve shapes and parameter values typical of sand soils can be used to describe in situ flow behavior of this conglomeratic alluvial soil implies that more complicated models, such as those with corrections to unsaturated soil models (e.g., *Bouwer and Rice* 1984; *Peck and Watson* 1979) or separation of the relatively fine-grained fraction from the coarse fraction (e.g., *Dann et al*. 2009; *Tetegan et al.* 2011), and the associated additional model parameters, are not necessary to characterize unsaturated flow in conglomeratic alluvial soil, particularly under natural recharge conditions and where saturation values are low.

Figure 3-13 also emphasizes the relationship between parameter predictability and the saturation range of the experiment. Final θ values from the experiment were only about half of estimated θ_S (50% saturation) in materials M1 and M4, and Figure 3-13 shows that more of the 2000 $\theta(\psi)$ and $K(\psi)$ curves diverge near saturation, with the most clear example coming from M1. Less agreement at high saturation implies poor resolution of parameters that influence that portion of the curve: mainly θ_S and K_s. When not constrained by the observed data, θ_S and K_s represent only end points of the curves and thus will be difficult to resolve without outside constraint (e.g., independent estimates), a conclusion also reached by *Scharnagl et al.* (2011). A similar case can be made for α, which relates to the bubbling pressure or the ψ value at which θ begins to decrease from saturation. If near-saturation is not reached, α may also be difficult to resolve, as is evident from the distributions shown in Figure 3-10. Had the experiment covered the full range of saturation, θ_S and α would become more resolved and, given the high correlation between θ_S and other parameters (especially K_s), many other parameters would likely be better resolved as well. Fortunately, saturated parameters like θ_S and K_S can be easily and accurately obtained from other methods or experiments, which can be used to constrain unsaturated models when full saturation is not reached.

The $\theta(\psi)$ and $K(\psi)$ curves shown in Figure 3-13 also indicate the insensitivity of the model to M2 – not only to individual M2 parameters, but to the shape of the full $\theta(\psi)$ and $K(\psi)$ functions. The wide distribution on the M2 $\theta(\psi)$ curves, but still low *NLL* values, shows that the forward model and calculated data are insensitive to M2 and that given the field experiment (and likely violation of 1D assumptions for M2 especially), the model will struggle to resolve M2 parameters in its current capacity. This is not

surprising given that θ measurements were not made within M2 and, according to installation depths of AT8, ψ measurements were made very near the top of the material zone (see Figure 3-9). Had the sensor been located lower in the material, $\psi(t)$ data observed would have been more influenced by M2 $\theta(\psi)$ and $K(\psi)$ functions, as water would have to flow through more of that material before reaching the sensor. Interestingly, if we were to look only at $\theta(\psi)$ and $K(\psi)$ curves produced from chain MH_2 (μ and σ of curves shown in Figure 3-13), which maintained a higher *Mo* for n_{M2} and $K_{S,M2}$ for much of the last $5x10^5$ runs, the $\theta(\psi)$ and $K(\psi)$ curves have much better agreement and have a shape more similar to typical soils (i.e., clearly defined curve and bubbling pressure). It is possible that the higher n and K_S values initially predicted by MH_2, because of the initial parameter set, were due to the sampling algorithm becoming temporarily trapped in a local minimum. As MH_2 progressed further, it began to approach the global minimum approached by the other chains. Had I stopped the algorithm too soon, or used only the results from MH_2, I would have predicted higher n and K_S values and more informative $\theta(\psi)$ and $K(\psi)$ curves, but would have overestimated the dependence of the model to parameters n_{M2} and $K_{S,M2}$ and underestimated parameter uncertainty.

In Figure 3-13, I show how the range of optimal parameters predicted by the MH sampling produced wide distributions of some parameters but that those parameters still work together to produce informative $\theta(\psi)$ and $K(\psi)$ relationships over the range of saturation achieved by the experiment (similar concept as *Stauffer and Lu* 2012). To show the model's ability to reproduce the observed $\psi(t)$ and $\theta(t)$ data from the experiment, I took a similar approach as in Figure 3-13 of using a random sample of

parameter sets from within the final distributions. In Figure 3-14, I show fits to observed $\psi(t)$ and $\theta(t)$ data for 2000 forward model runs using randomly chosen parameter sets. Figure 3-14 further emphasizes that uncertainty in input parameters does not necessarily correlate to uncertainty in the calculated data or negate the model's ability to capture observed behavior.

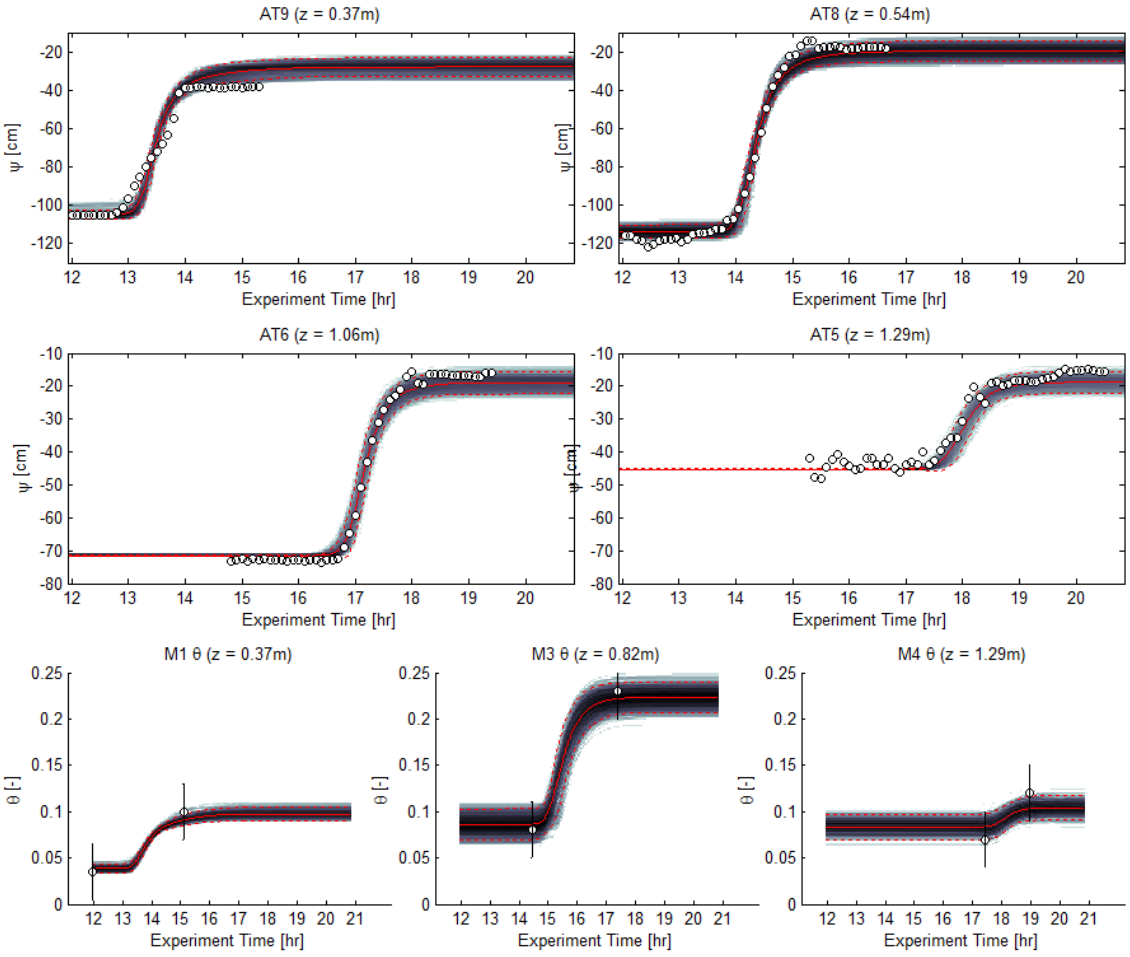

Figure 3-14: $\psi(t)$ and $\theta(t)$ intensity plots calculated from 2000 parameter sets taken from MH_{all} for the four observed AT and three moisture measurement depths; darker shades indicate where more of the curves overlap; solid lines are mean values and dashed lines are $\pm 2\sigma$. White circles are observed data.

3.6 Conclusions

Final parameter distributions from the last $5x10^5$ samples of the five MH chains produced similar mode values and 11 of the 16 parameter distributions converged, as measured by the *SR* factor. Marginal distributions and R^2 showed that some material parameters were very highly correlated ($R^2 > 0.9$), specifically θ_S-K_S and α-n. Despite the range of parameter values within individual and combined chains, $\theta(\psi)$ and $K(\psi)$ curves predicted by randomly chosen parameter sets were generally in agreement within the range of observed ψ, θ, and K produced by the experiment and diverged as the curves approached saturation, which was not reached by the experiment. Similarly, $\psi(t)$ and $\theta(t)$ predicted from the same randomly chosen sets were in very good agreement with each other and with the observed data despite wide distributions of some parameters, indicating parameter non-uniqueness.

The results of this chapter highlight the strong non-uniqueness of unsaturated hydraulic properties of coarse, conglomeratic material specifically, and unsaturated materials in general, and the difficulty involved in obtaining a single ideal set of parameter values for a given material under natural field conditions, especially when 1D assumptions are violated and optimal data are not collected for all materials. Gathering additional information, such as $\psi(t)$ and $\theta(t)$ in each material layer, covering the full range of saturation during the experiment (i.e., by applying precipitation at rates far exceeding natural conditions), or constraining parameters with prior information, would lead to tighter, more informative distributions of VGM functions but would likely still be burdened by parameter cross-correlation and non-uniqueness.

In conclusion, this chapter 1) presents the successful application of a field-based infiltration experiment to characterize in situ unsaturated hydraulic properties for a coarse (sand, gravel, and cobble), alluvial sediment sequence, 2) shows that high infiltration rates (i.e., greater than natural precipitation rates for longer periods) can be accommodated by conglomeratic soil despite relatively low porosities and high concentration of large cobbles, 3) highlights the difficulty in developing soil characteristic curves for coarse soil types under natural infiltration conditions, given that moisture levels may not reach saturation and thus certain parameters like θ_S and K_S will be difficult to resolve, and 4) suggests that soil characteristic functions developed for fine-grained agricultural soils, such as van Genuchten-Mualem relationships, can be successfully applied to predict in situ unsaturated flow behavior of coarse, conglomeratic alluvial soils.

In the next chapter, I extend the conceptual model of the infiltration test volume to a 2D model that incorporates the observed variation in material thickness and I use the full suite of $\psi(t)$ and $\theta(t)$ data to estimate VGM parameters. The additional complexity of the 2D distribution of materials, along with allowing for lateral flow, helps to further constrain parameter distributions and reduce uncertainty in parameter values.

CHAPTER 4: ESTIMATION OF 2D DISTRIBUTION OF UNSATURATED HYDRAULIC FUNCTIONS OF A COARSE STONY SEDIMENT SEQUENCE FROM A FIELD-SCALE INFILTRATION EXPERIMENT, BOISE HYDROGEOPHYSICAL RESEARCH SITE

Much of the work presented in this chapter has been developed into a research journal article to be submitted to Vadose Zone Journal with the following authors: Michael J. Thoma, Warren Barrash, John H. Bradford, and Michael M. Cardiff.

4.1 Introduction

Chapter 3 established that van Genuchten-Mualem (VGM) relationships could be used to accurately describe infiltration in coarse, conglomeratic sediments even with high uncertainty in individual parameters and high parameter cross-correlation. This is because, as shown in Chapter 3 (see Figure 3-13), the shape of the VGM curves (i.e., $\theta(\psi)$ and $K(\psi)$ functions) is what controls unsaturated flow, not individual parameters. The modeling and optimization in Chapter 3 failed to constrain VGM parameters to within an acceptable level of uncertainty, which was partially attributed correlation between parameters in Chapter 3, but is also due to the use of only partial $\theta(t)$ data and the inability of the 1D model to represent lateral variation in material distributions. The exclusion of the full $\theta(t)$ data set was due to significantly different percolation rates between TX5BS (where $\psi(t)$ data were measured) and NX5B (where $\theta(t)$ data were measured) (Figure 4-1 or see Figure 3-8).

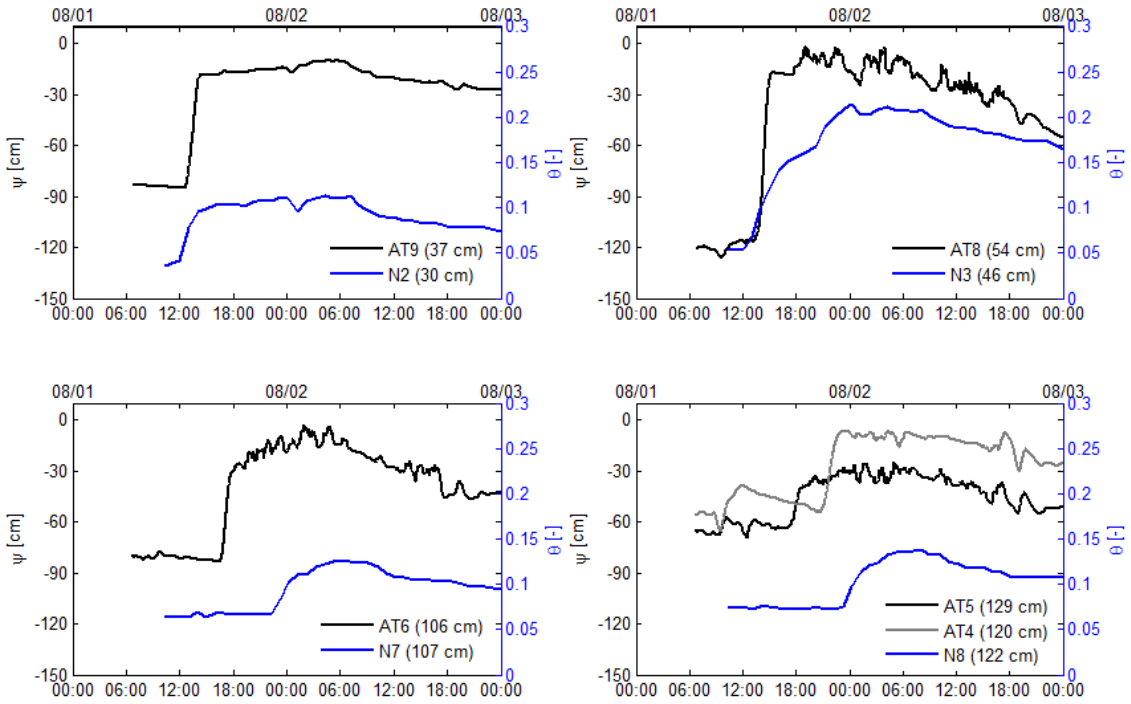

Figure 4-1: $\psi(t)$ and $\theta(t)$ responses for the full infiltration period and partial recovery period at selected depths (z [cm bls]).

In this chapter, I expand the 1D model presented in Chapter 3 to a 2D model that better represents our knowledge of the material structure within the infiltration test volume. The 2D model incorporates lateral variations in material thickness (measured from GPR data) and allows for lateral moisture flow. The 2D model also includes the full $\psi(t)$ and $\theta(t)$ data sets in parameter optimization. Optimization of the 2D model was done in three main stages. Stage 1 used direct sampling from within the final parameter distributions from Chapter 3 to determine if parameter values for the 2D model were within the range of the 1D model results. Stage 2 used multiple direct-search optimization chains to fit either $\theta(t)$, GPR reflection travel-time data (discussed below), or all data simultaneously ($\theta(t)$, $\psi(t)$, and GPR data). Stage 2 results show, among other things, that fitting both $\theta(t)$ and $\psi(t)$ data cannot be achieved with the current model despite parameter values that are similar and are from overlapping distributions. This is because

VGM curves (i.e., $\theta(\psi)$ and $K(\psi)$ functions) developed from optimal parameter values are not directly matched for material M3 which is shown to be caused by lateral heterogeneity within the M3 layer not previously identified from GPR data. In Stage 3 I separate M3 laterally into two materials creating a five-material model. A final direct search optimization with the five-material model was then used to estimate VGM parameters for all five materials, and Latin-hypercube Sampling was used to estimate uncertainty which was significantly reduced from the results in Chapter 3.

In this chapter I also develop a method from observed GPR data to use the changes in travel-time from a material reflection boundary (Δt_{bndry}) to track changes in θ across the full 2D model profile. The Δt_{bndry} data were used in parameter optimization but the current model failed to accurately fit the observed Δt_{bndry} data and so did not provide additional constraint of parameters. Near the end of this chapter I address some of the issues with this method and speculate why it failed to work with the current data.

4.2 Methods

4.2.1 Development of the 2D Model

The 2D model was built to include the variation in material thickness and to represent the vadose zone structure along the instrumentation axis (line of TX5BS-TX5BD- NX5B and GPR line in Figure 3-1) using HYDRUS 2D (*Simunek et al.* 1999). The 2D model (M2D) extended 1 m beyond the wetted area at each edge and to a depth of 3.0 m bls. Initial $\psi(x,z)$ was prescribed the same vertical distribution as the 1D model (M1D) of Chapter 3 and was homogeneous in the x direction. Model time started on August 1 at 000 MDT (11.5 hrs before precipitation started, to ensure that initial

conditions would not greatly affect results) and the model was run for 48 hrs to encompass the full wetting of the vadose zone. The lower boundary was set as a constant-head boundary with head = 124 cm referring to the constant water table depth during the infiltration experiment. From x = 1 m to x = 7 m, the upper model boundary was prescribed a variable-flux boundary equal to the mean precipitation rate (P = 0.84 cm hr^{-1}) for the time of preciptiation (t = 11.5 – 32 hr model time) and was prescribed to P = 0 for all other times.

Initial material structure was derived from the GPR profile data collected along the instrumentation axis prior to the infiltration test, but was later finalized using one of the GPR *x*-*t* profile images taken after steady-state had been reached but before the rain application ended. At this snapshot (t = 32 hr model time), the vadose zone possessed the highest θ of any time during the experiment (providing highest resolution of GPR data) and was at steady-state. Pre-stacked, depth migrated, multi-offset GPR data were used with reflection tomography (*Bradford* 2008) to determine a velocity structure and to accurately determine depths of material boundaries (Figure 4-2; see Figure 3-2 for GPR data). The velocity structure was also determined at each 1 hr interval and used with the CRIM equation (*Jol* 2009) to estimate $\theta(x,z,t)$ distributions. The full set of GPR-derived $\theta(x,z,t)$ data is not discussed here since it was used in this chapter only to provide semi-quantitative confirmation of model-predicted θ distribution. Two-way travel time to the M3-M4 boundary derived from the GPR data was used throughout the experiment to track changes in θ and is discussed later in this chapter.

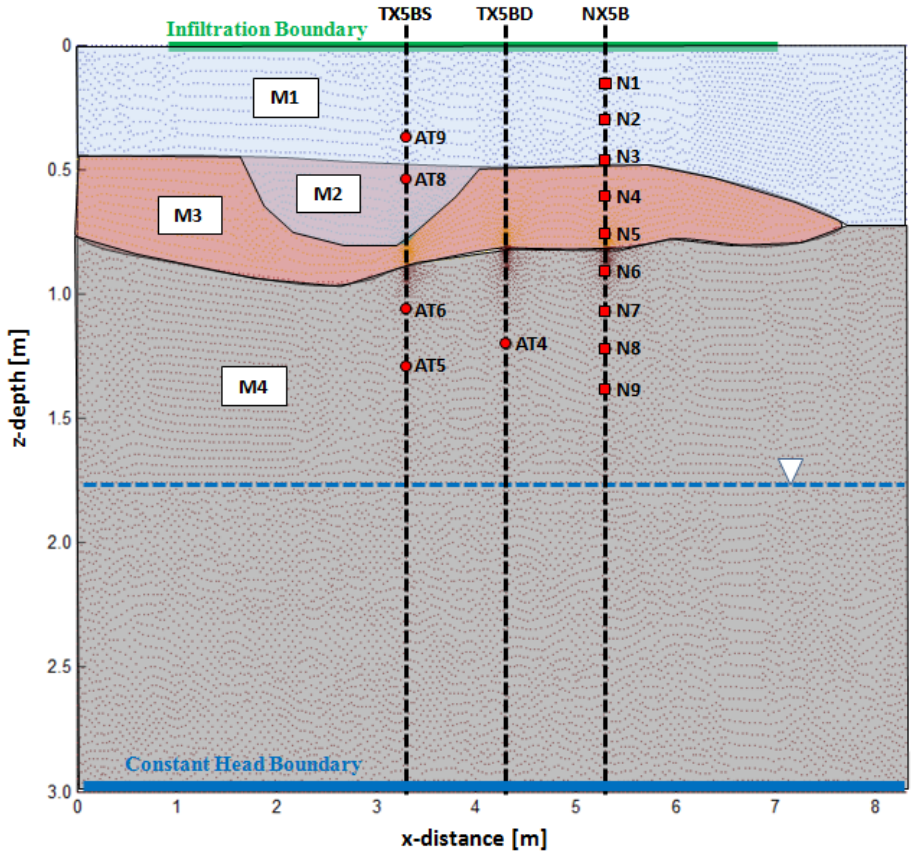

Figure 4-2: M2D material structure, boundary conditions, and observation nodes (● = ψ measurements, ■ = θ measurements).

HYDRUS 2D is a finite-element model where element size (distance between nodes) can either be determined automatically, or constrained by the user by setting refinement points (*Simunek et al.* 1999). As with all discretized models, a compromise must be made between run time (increases with finer discretization) and model accuracy (also increases with finer discretization). I chose to define element size between 0.005 m and 0.05 m in areas corresponding to material breaks and measurement locations, and as ≤ 0.1 m elsewhere in the model. The final model consisted of ~18,000 finite-element nodes and took between 4 and 8 min to run on a standard desktop computer.

Observation nodes were placed at element nodes corresponding to depth and lateral dimension of five ψ measurement locations (AT9, AT8, AT6, AT5, AT4) and nine θ measurement locations (N1 – N9 in Figure 4-2). $\psi(t)$ and $\theta(t)$ data were output from the model for these observation nodes at 6 min increments.

4.2.1.1 Volumetric Moisture Sampling

The neutron moisture probe used to measure θ during the experiment records an average θ over the full volume of influence and this volume is dependent on the average θ with the relationship

$$R = 15 \cdot \theta^{-1/3} \qquad (4\text{-}5)$$

where R [cm] is the radius of the spherical sampling volume (*IAEA 1970*). The effect of sampling volume on θ measurements in less severe in homogeneous soils, but where sharp breaks exist between soils of different composition (e.g., M1-M3 or M3-M4 boundaries), measurements taken near the boundary may be influenced by the nearby material even if the measurement depth is not within that material. To maintain the highest level of accuracy possible when using the θ data in the model, I use Equation 4-5 to calculate the average predicted θ at each observation node from all nodes within the sampling radius R, and assign that average θ value to the observation node. In Figure 4-3, I compare raw, model-output θ, and averaged θ using Equation 4-5 for observation nodes N3, N4, and N5 from the M2D model to show the importance of this correction.

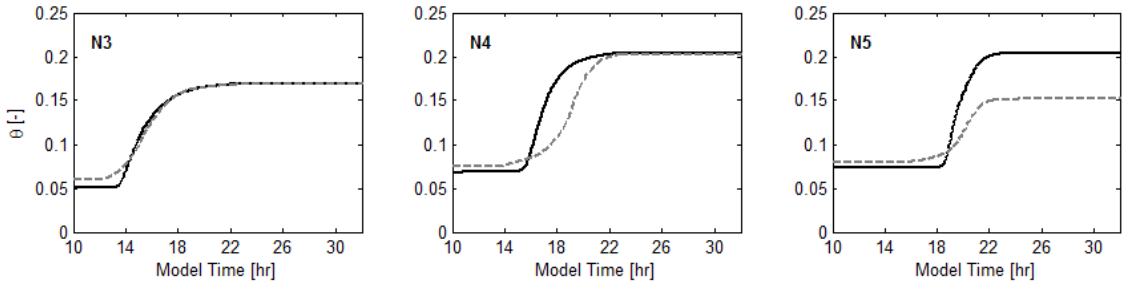

Figure 4-3: Comparison of raw (solid line) and averaged (dashed line) predicted θ at observation nodes N3, N4, and N5.

4.2.2 Incorporation of GPR Data

The GPR data collected during the infiltration test were used to estimate material depths by estimating the electromagnetic wave velocity (v_{EM}) and reflection times to various boundaries (t_{bndry}) to determine the depth of those boundaries (*Bradford* 2008). Figure 3-2 in Chapter 3 shows only a single GPR profile taken prior to infiltration to illustrate material depths because v_{EM} is a function of θ, and so the estimated v_{EM} and thus t_{bndry} will vary throughout the experiment as θ in the vadose zone increases. As water percolates through the vadose zone and the average θ increases between the land surface and a material boundary, v_{EM} decreases and the observed t_{bndry} increases. If t_{bndry} of a continuous reflector (i.e., material boundary) can be tracked through the time-lapse GPR images, the change in t_{bndry} (Δt_{bndry}) can be used to estimate the change in overall θ between the land surface and the reflector depth. In Figure 4-4 I show GPR profile data from four different times during infiltration to show the change in t_{bndry} of the M3-M4 reflection as θ increases.

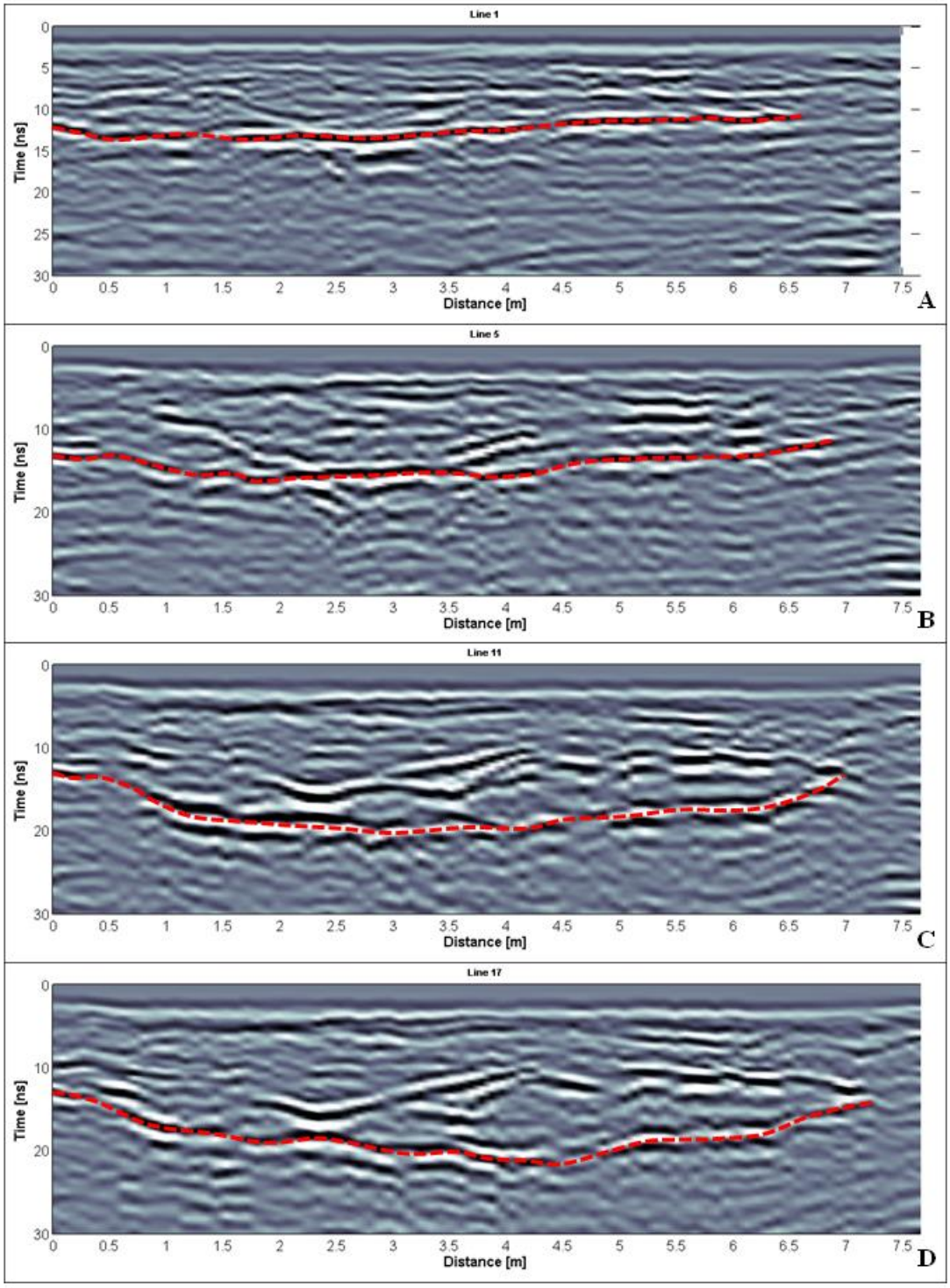

Figure 4-4: GPR profile data from four times during infiltration: A) prior to test (0 hrs), B) 4 hrs into infiltration, C) 10 hrs, D) 16 hrs; dashed lines highlight M3-M4 material boundary.

The 2D time-lapse GPR data were analyzed in the following way to provide the information described in the preceding paragraph: 1) a continuous reflector was identifed that corresponded to the M3-M4 material boundary (see Figure 4-2). This reflector was not only continuous across the profile but easily identified in nearly all of the time-lapse GPR images. 2) t_{bndry} for this reflector was picked along the profile for all of the time-lapse images by selecting the time of peak amplitude. For certain time-lapse images where the continuous reflector could not be readily picked, it was interpolated from either points surrounding it or from its location in previous or later time-lapse images. 3) Δt_{bndry} along the length of the 2D profile was determined over the time of infiltration by subtracting t_{bndry} of the current measurement time from the initial t_{bndry}. In Figure 4-5, I show Δt_{bndry} through the full experiment time (including partial recovery) extracted at 1.0 m intervals across the profile. The increase in Δt_{bndry} with increase in x is due to higher θ in the thicker M3 material in the right half of the model (see Figure 4-2).

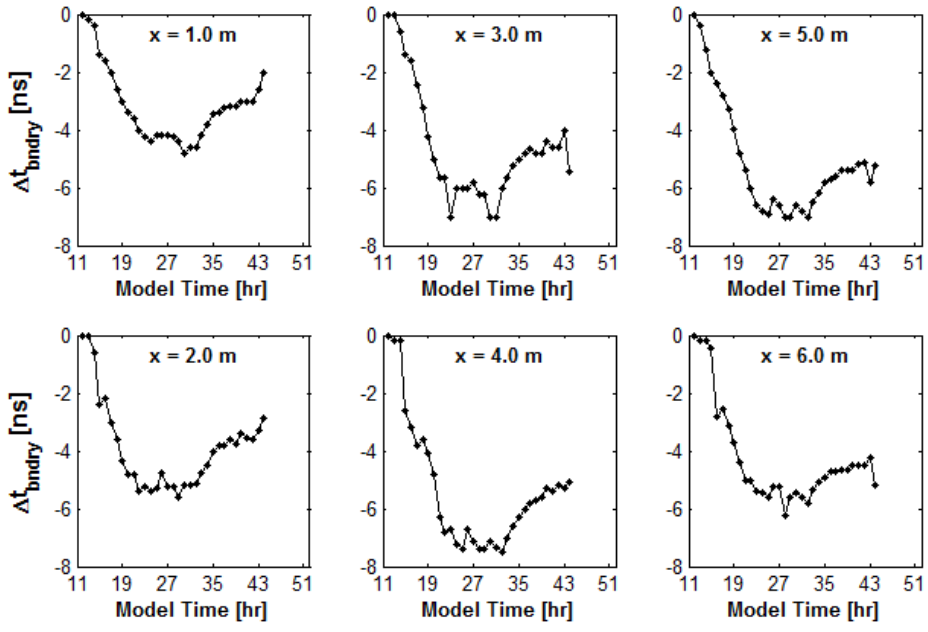

Figure 4-5: Observed Δt_{bndy} data at 1.0 m intervals across the GPR line.

The M2D model was used to predict Δt_{bndry} throughout the infiltration portion of the test (11.5 – 30 hr model time) using the time-derivative of the Complex Refractive Index Method (CRIM) equation (*Jol* 2009), which relates relative dielectric permittivity of the bulk soil (ε_{bulk}) to θ:

$$\sqrt{\varepsilon_{bulk}} = \left[\sqrt{\varepsilon_{matrix}}(1-\phi) + \sqrt{\varepsilon_{water}}(\theta) + \sqrt{\varepsilon_{air}}(\phi-\theta)\right] \tag{4-6}$$

where ε_{bulk}, ε_{matrix}, ε_{water}, and ε_{air} are the relative dielectric permittivities of the bulk soil, the soil solid matrix, water, and air, respectively and ϕ is the soil porosity. Using the relationships between ε_{bulk} and v_{EM} for non-magnetic, low-loss soil

$$v_{EM} = \frac{c}{\sqrt{\varepsilon_{bulk}}} \tag{4-7}$$

and

$$v_{EM} = \frac{2d_{M4}}{t_{bndry}} \tag{4-8}$$

where v_{EM} is discribed above, c is the speed of light (3×10^8 m s^{-1}), and d_{M4} is the depth of the reflector corresponding to the top of the M4 boundary. The multiplier of 2 corresponds to the two-way travel time recorded by the GPR equipment. Combining Equations 4-6 thru 4-8 and solving for time yields:

$$t = \frac{2d_{M4}}{c}\left[\sqrt{\varepsilon_{matrix}}(1-\phi) + \sqrt{\varepsilon_{water}}(\theta) + \sqrt{\varepsilon_{air}}(\phi-\theta)\right]. \tag{4-9}$$

Taking the derivative of Equation 4-9 with respect to θ I arrive at:

$$\Delta t_{bndry} = \frac{2d_{M4}}{c} \cdot \left(\sqrt{\varepsilon_w} - 1\right) \cdot \Delta\theta \qquad (4\text{-}10)$$

and see that Δt_{bndry} is a linear function with $\Delta\theta$ and the slope is only a function of constants ε_w (~80 for freshwater), c, and $2d_{M4}$.

At each model output time, the full 2D distribution of θ was interpolated into equally-spaced columns at 0.1 m intervals between the left and right model boundaries. Within each column the average θ between the surface and d_{M4} (i.e., M3-M4 material boundary) was determined and used with Equation 4-10 to estimate Δt_{bndry} of the M3-M4 boundary. In later optimization, the calculated Δt_{bndry} was compared to the observed Δt_{bndry} from the GPR data at 1 m intervals across the model every 3 hrs.

A quick check of the above equations was perfomed to ensure they accurately describe Δt_{bndry} by manually calculating Δt_{bndry} from $\Delta\theta$ measured in NX5B above the M3-M4 boundary between initial and steady-state times. This "true" value was then compared to the observed Δt_{bndry} from GPR data at the location of NX5B (x = 5 m). Average $\Delta\theta$ estimated at NX5B was 0.10 ± 0.03, and using Equation 4-10 and a value of 81 cm for d_{M4}, I arrive at a value for steady-state Δt_{bndry} of 4.2 ± 1.28 ns. Observed Δt_{bndry} at the location of NX5B is ~6.5 ± 0.5 ns, which is 2.3 ns error. If I invert Equation 4-10 and use the observed Δt_{bndry} as input, the required $\Delta\theta$ to produce a 6.5 ns Δt_{bndry} is 0.15 ± 0.01. Error between these manual calculations may be (a) the result of uncertainty in observed $\Delta\theta$ (particularly near the M3-M4 boundary where measured $\Delta\theta$ will be influenced by M4 material, likely with lower θ, while GPR-derived $\Delta\theta$ is not), (b) due to the coarse sampling of θ measurements, or (c) due to error in estimating d_{M4}. It is also possible that the additional θ required to accuratly fit Δt_{bndry} data can be found through

optimization below and still fit the observed $\psi(t)$ and $\theta(t)$ data, so I withhold my discussion until later in the chapter.

4.3 Parameter Optimization

This section describes the setup and results of a sequence of optimization methods to identify optimal material parameters for the M2D model. The first method is based on direct sampling (DSm) from within the M1D final distributions of Chapter 3 (see Figure 3-10) and was used to determine whether parameter distributions developed from the 1D modeling Chapter 3 can be used to successfully predict $\psi(t)$ and $\theta(t)$ with the M2D model. The second method uses multiple direct search (DSr) chains to identify optimal parameters for individual objective functions designed to minimize misfit of either $\theta(t)$, Δt_{bndry}, or all data combined ($\psi(t)$, $\theta(t)$, and Δt_{bndry}). The results of these first two methods imply that a four-material model is not sufficient to predict both $\psi(t)$ and $\theta(t)$ data simultaneously, and I later alter the M2D model by adding lateral variation in M3 and thereby increasing the number of materials to five. The five-material model (M2D-5L) is then used with a single DSr run and Latin-hypercube Sampling (LHS) to optimize parameters and estimate parameter uncertainty.

Optimization of the M2D model was based on the model's ability to accurately predict the observed $\psi(t)$, $\theta(t)$, or Δt_{bndry} data, which was quantified with the negative-log likelihood function (*NLL*)

$$NLL_i = \frac{1}{2}\left[d_{err,i}{}^{T} \cdot C_{d,i}{}^{-1} \cdot d_{err,i}\right] \tag{4-11}$$

where $d_{err,i}$ is a vector of the error between the observed and calculated data set, $C_{d,i}$ is the data covariance matrix, a diagonal matrix with elements equal to the estimated error, or

variance (σ^2), of the data, and *i* refers to the data set being measured with *i* corresponding to $\psi(t)$, $\theta(t)$, or Δt_{bndry} data. For $\psi(t)$ data, observed σ_ψ was set to 8 cm which incorporates measurement error along with additional uncertainty in measurement depths and AT offsets mentioned in Chapter 3. Observed σ_θ is 0.03 based on instrument precision (*Johnson et al.* 2013b) and I use this value in $C_{d,\theta}$. For Δt_{bndry} data I estimated $\sigma_{\Delta t}$ from the observed variance of t_{bndry} data at steady-state, which was ~0.5 ns.

The value of *NLL* depends on the length of the d_{err} vector, which depends on the data set. For $\psi(t)$, I included ~100 data points (300 min) for each of the five ATs with the data centered on t_{wf} at each sensor. For $\theta(t)$ data, I use 12 data points (12 hr) at each measurement depth, again centered on t_{wf}. For Δt_{bndry}, I chose to compare data at 3 hr intervals at 1 m spacing in the *x*-direction (35 points). The overall accuracy of the model (i.e., its ability to fit all data) is measured by the weighted-sum *NLL* value

$$\sum NLL = w_\psi NLL_\psi + w_\theta NLL_\theta + w_{\Delta t} NLL_{\Delta t} \tag{4-12}$$

where w_ψ, w_θ, *and* $w_{\Delta t}$ are individual weights used to adjust the influence of each objective function over ΣNLL. NLL_ψ was on average three times greater than NLL_θ so w_θ was set to a value of 3 to provide equal influence of each function. Because I was primarily interested in fitting $\psi(t)$ and $\theta(t)$ data, Δt_{bndry} data were treated as a secondary data set so $w_{\Delta t}$ was set to 1 to avoid over-influence from $NLL_{\Delta t}$.

4.3.1 Method 1: Direct Sampling

The Direct Sampling (DSm) method investigates the ability of the M1D final parameter distributions to predict the observed 2D data and involves direct use of complete parameter sets (all 16 parameters in a single MCMC step) in the M2D model. A

random selection of 2000 non-repeating sets was chosen from the M1D distributions and each set was run in the M2D model.

There was, however, one caveat with selection of the 2000 sample sets which introduced bias into the second half of the selected sets (sets 1001 – 2000). The MCMC algorithm searches for the minimum objective function value given the parameters and, once a minimum is found, tends to stay within that parameter space. Many of the final sets from the M1D model found optimal values of n in M2 (n_2) between the lower limit ($n_2 = 1$) and $n_2 = 1.1$ such that >60% of the first 1000 DSm sample sets had n_2 values between 1.0 and 1.1 (Figure 4-6). Sample sets were not nearly so constrained with respect to other parameters as they were with n_2 and most other parameters ranged through much of the a priori distributions. However, I wanted to avoid undersampling the full range of n_2 and so, for the second 1000 sample sets. I constrained sampling to a priori sets where $n_2 > 1.1$. Although this limited some other parameters, the second 1000 sets covered nearly the full range of the a priori distributions for all but four paramters: θ_{S2}, K_{S2}, α_3, and K_{S3}. The most extreme case was K_{S3} where σ for the n_2-constrained set is two orders of magnitude lower than when n_2 is unconstrained (Figure 4-6). It is important to note that the distribution of the M1D objective function values (i.e., how well the parameter sets fit the data in the 1D model) was not significantly different between the first and second 1000 parameter sets.

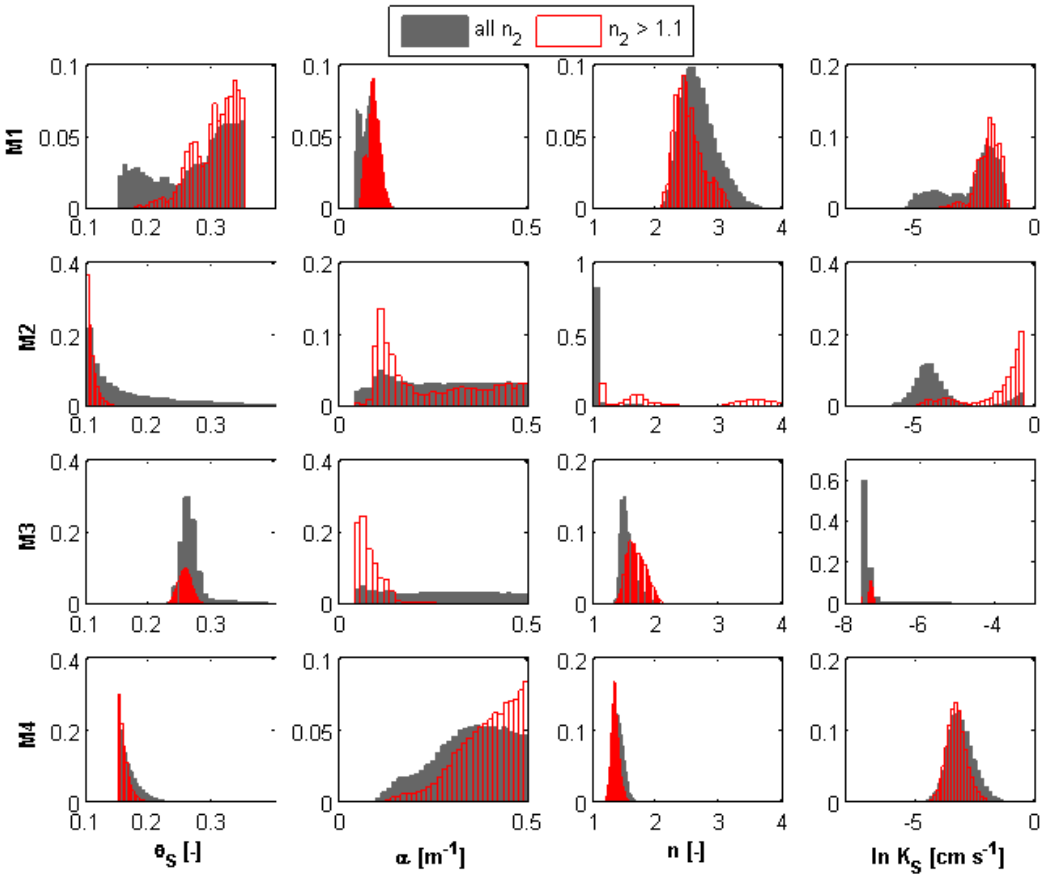

Figure 4-6: M1D parameter distributions of full sets (solid grey) and n_2-constrained sets (red outline).

Each of the 2000 DSm parameter sets were run in the M2D model and final distributions of NLL_ψ, NLL_θ, and $NLL_{\Delta t}$ are shown in Figure 4-7, separated into the first1000 samples and second1000 samples. When $n_2 > 1.1$ (n_2-constrained), the distributions of NLL_ψ, NLL_θ, and $NLL_{\Delta t}$ are more narrow and are shifted to lower values (i.e., better fits to the observed data), but cover the same range of *NLL* when n_2 is unconstrained. This implies that constraining n_2 is not significantly limiting the model's ability to fit the observed data while avoiding oversampling parameter space with high *NLL* values (i.e., poor-fitting parameters). Minimum values and NLL_ψ, NLL_θ, and $NLL_{\Delta t}$ were 159, 67, and 15.8, respectively and were found in the first, second, and first1000 sets (minimum value of NLL_θ from the second 1000 sets was 68.7). The M2D predicted

$\psi(t)$, $\theta(t)$, and Δt_{bndry} from each best-fit data set (i.e., minimum NLL_ψ, NLL_θ, and $NLL_{\Delta t}$) are shown in Figures 4-8 and 4-9. The success of the M2D model at predicting the observed $\psi(t)$ data provides validation of model consistency between the M1D and M2D models.

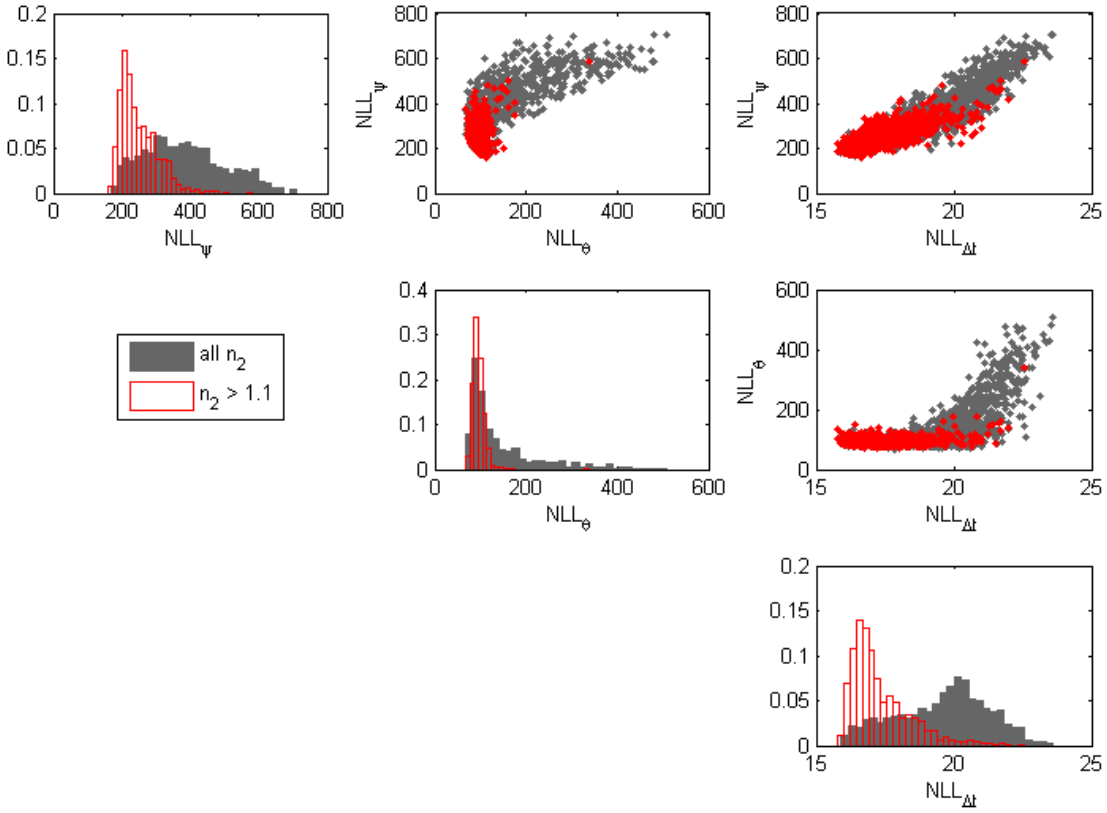

Figure 4-7: Distributions of NLL_ψ, NLL_θ, and $NLL_{\Delta t}$ from the direct sampling investigation separated by unconstrained sets (grey) and n_2-constrained sets (red).

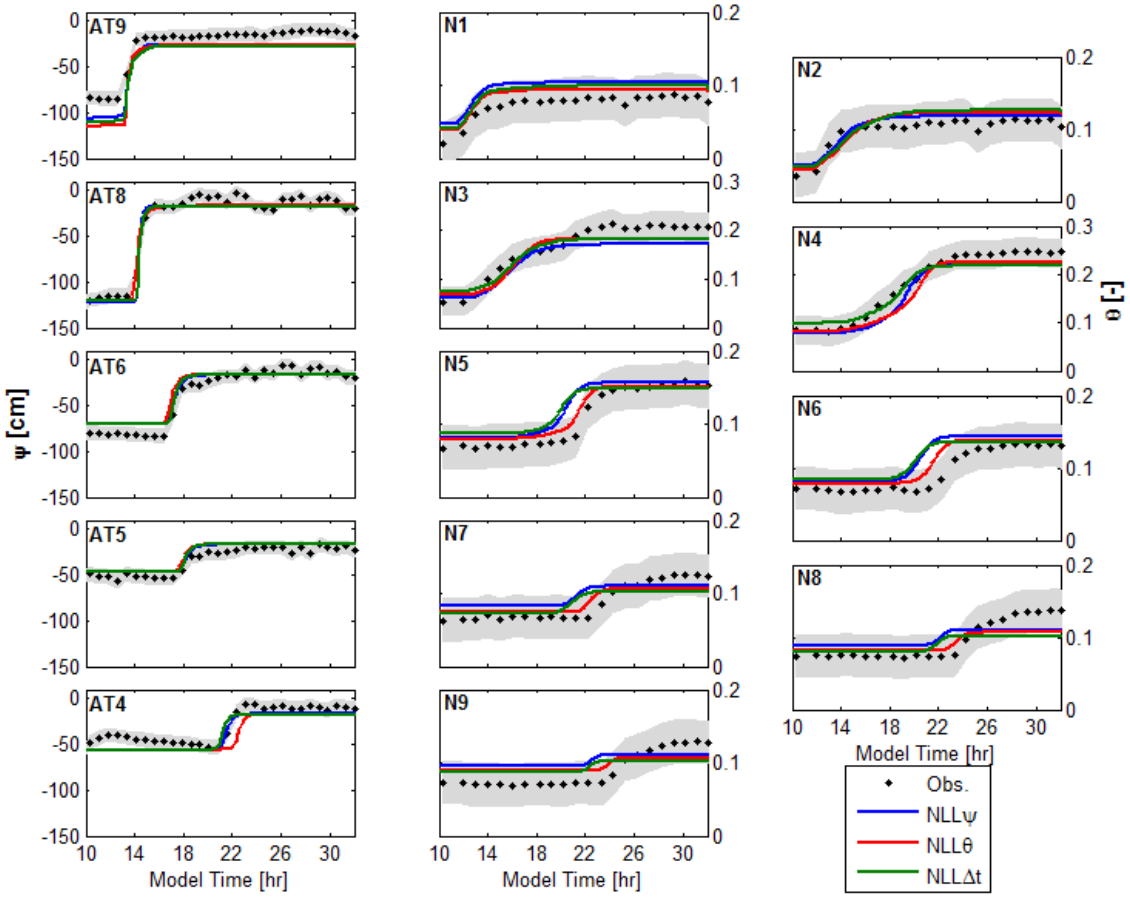

Figure 4-8: Optimal fits to $\psi(t)$ and $\theta(t)$ from minimum NLL_{ψ}, NLL_{θ}, and $NLL_{\Delta t}$ parameter sets of the DSm method (note different y-axis for N3 and N4); shaded regions show ±1σ data error.

From the $\psi(t)$ and $\theta(t)$ data fits (Figure 4-8) we see that minimum sets from NLL_{ψ} and $NLL_{\Delta t}$ fit the observed $\psi(t)$ and $\theta(t)$ data equally well, although neither set accurately predicts t_{wf} of $\theta(t)$ data below 60 cm and both predict earlier t_{wf} than what is observed. The minumum NLL_{θ} set accurately predicts $\theta(t)$ data and closely predicts $\psi(t)$ data for all sensors except AT4, where it is predicting much later t_{wf} than what is observed. The implications of improper fitting of AT4 will be discussed below.

In Figure 4-9 I show the observed and calculated Δt_{bndry} data for all three minumum DSm sets and we see that none of the direct sampling sets came close to fitting

the observed Δt_{bndry} data except near the beginning of the GPR line (left side of model). Near the end of the model time (t = 30 hr), after steady-state had been reached, differences between observed and calculated Δt_{bndry} are 2.2 – 3.3 ns, which is similar to error in manually-calculated Δt_{bndry} above. This is somewhat surprising given that $\psi(t)$ and $\theta(t)$ data are closely matched with the same parameter sets, specifically the initial and steady-state $\theta(t)$, which are responsible for $\Delta\theta$ and will have the greatest influence over Δt_{bndry}. I withhold further investigation of Δt_{bndry} fits until the next section where optimization is focused on, among other things, directly minimizing $NLL_{\Delta t}$.

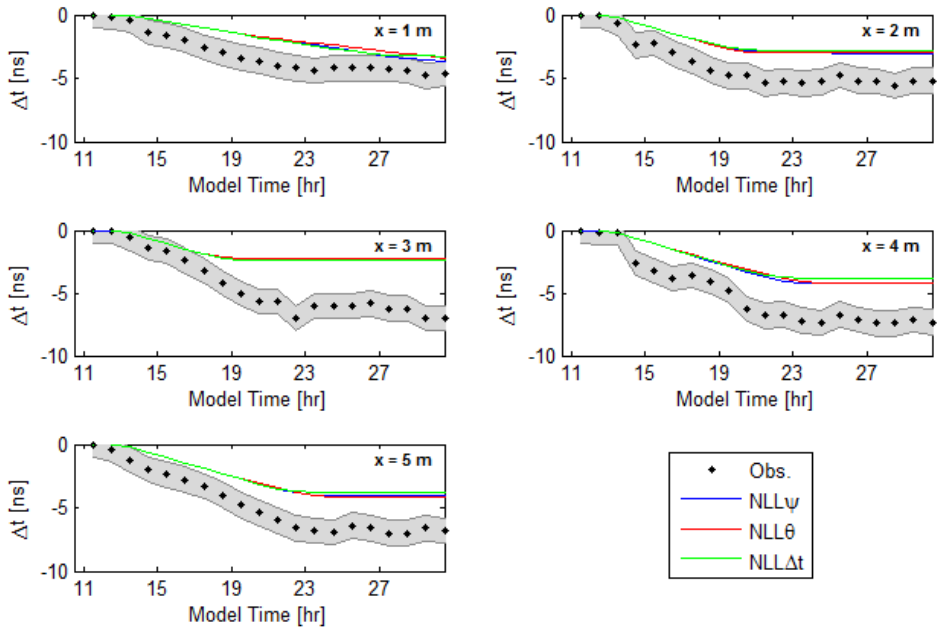

Figure 4-9: Optimal fits to Δt_{bndry} from minimum NLL_{ψ}, NLL_{θ}, and $NLL_{\Delta t}$ parameter sets of the DSm method; shaded regions show ±1σ data error.

From the results of the DSm investigation I make three conclusions about the ability of the M1D parameter distributions to predict M2D data: 1) constraining $n_2 > 1.1$ does not inhibit optimization of NLL_{ψ} or NLL_{θ} (i.e., the model's ability to predict $\psi(t)$ or θ(t) data) but instead appears to eliminate sampling much of the "bad" objective function

space, where more of the poor-fitting parameter sets are found. 2) Lack of abundant correlation between NLL_{ψ} and NLL_{θ} (Figure 4-7) suggests that there may not be an optimal data set that fits all $\psi(t)$ and $\theta(t)$ data equally well (especially when considering $\psi(t)$ in AT4). 3) The model-predicted $\psi(t)$ and $\theta(t)$ data show that the DSm sets more accurately predict $\psi(t)$ data than $\theta(t)$ or Δt_{bndry} data, which is expected given that the DSm sets were sampled from distributions that fit $\psi(t)$ data in the M1D model. In the next section, I attempt to directly minimize NLL_{θ}, $NLL_{\Delta t}$, ΣNLL using a multi-start direct search approach.

4.3.2 Method 2: Direct Search Inversion

The DSm method provided acurate fits to observed $\psi(t)$ and $\theta(t)$ data independently but fell short of accurately predicting both data sets simultaneously or predicting Δt_{bndry}. Since both $\psi(t)$ and $\theta(t)$ data could be closely predicted from parameter sets within the M1D distributions, I continue with optimization of the four-material model using the M1D distributions as the a priori sampling sets. In this section, however, I use a DSr algorithm to further optimize parameters and predict $\theta(t)$ and Δt_{bndry} data separately (i.e., minimizing NLL_{θ} or $NLL_{\Delta t}$), and all data simultaneously (minimizing ΣNLL). I do not apply the DSr algorithm exclusively to NLL_{ψ} since optimal parameter distributions were explored in the M1D sampling Chapter 3.

Nine independent DSr algorithms were run with the MATLAB function *fminsearch* using three starting parameter sets chosen from within the second 1000 DSm sets (n_2-constrained). The three starting sets were sampled randomly from within the first, second, and third terciles (range of 33% probability) of the NLL_{ψ} distribution to ensure unique starting values. For each of the three starting sets, the DSr algortihm was run three

times: once with the objective function set to NLL_θ, once with it set to $NLL_{\Delta t}$, and once with it set to ΣNLL. For the optimization using ΣNLL, w_θ was set to 3 to provide more balanced influence of NLL_ψ and NLL_θ on ΣNLL. Values of w_ψ and $w_{\Delta t}$ were both set to 1. Each DSr chain was run to 300 iterations and was constrained within original bounds of the MCMC sampling in Chapter 3 (see Table 3-2) to maintain realistic and reasonable parameters, maintain computational efficiency (e.g., avoid excessive run time), and provide reasonable model convergence rates (i.e., limit the number of runs that do not converge). Initial and final *NLL* values and percent reduction from each DSr run are presented in Table 4-1. In each case, the DSr run minimized its primary objective function and improved the fit to its assigned data set.

Table 4-1: Initial and Final *NLL* values and percent reduction from nine separate DSr runs; bold values highlight which objective functions were reduced for which runs.

		r1	**r2**	**r3**	**r4**	**r5**	**r6**	**r7**	**r8**	**r9**
NLL_ψ	Initial	314	207	242	314	208	243	315	208	243
	Final	703	581	659	1144	210	1002	134	128	158
	% red.	*-124%*	*-180%*	*-172%*	*-264%*	*-1%*	*-313%*	*58%*	*39%*	*35%*
NLL_θ	Initial	**78.0**	**94.0**	**82.2**	78.0	94.0	82.2	78.0	94.0	82.2
	Final	**38.3**	**41.3**	**38.4**	804	134	408	84.1	89.8	84.2
	% red.	*51%*	*56%*	*53%*	*-930%*	*-43%*	*-396%*	*-8%*	*4%*	*-2%*
$NLL_{\Delta t}$	Initial	18.7	17.0	18.3	**18.7**	**17.0**	**18.3**	18.7	17.0	18.3
	Final	22.7	20.7	22.9	**11.0**	**15.8**	**12.0**	15.5	14.9	17.9
	% red.	*-21%*	*-22%*	*-25%*	*41%*	*7%*	*34%*	*17%*	*13%*	*2%*
ΣNLL	Initial	411	319	343	411	319	343	**411**	**319**	**343**
	Final	764	643	721	1959	360	1422	**233**	**232**	**260**
	% red.	*-86%*	*-102%*	*-110%*	*-376%*	*-13%*	*-315%*	*43%*	*27%*	*24%*

Runs r1 – r3 (which minimized NLL_θ) very accurately predicted $\theta(t)$ data ($NLL_\theta <$ 42) but final parameter sets did not accurately capture t_{wf} of $\psi(t)$ data (Figure 4-10) or Δt_{bndry} (not shown). Optimal parameter values for runs r1 – r3 are fairly consistent between the three DSr runs (Table 4-2) for materials M1, M3, and M4 but optimal M2 parameter values, especially n_2, are drastically different between the three DSr runs. This corroborates the results of the DSm above where optimal n_2 values were either on the low end (e.g., 1.77) or high end (e.g., 3.84) of the sampling range. The optimization in Chapter 3 also identified large uncertainty of M2 parameters as well as $\theta(\psi)$ and $K(\psi)$ curves for M2, and attributed it to lack of direct sampling in M2 of $\psi(t)$ data (due to depth distribution of ATs) and $\theta(t)$ data (due to finite lateral dimension of M2).

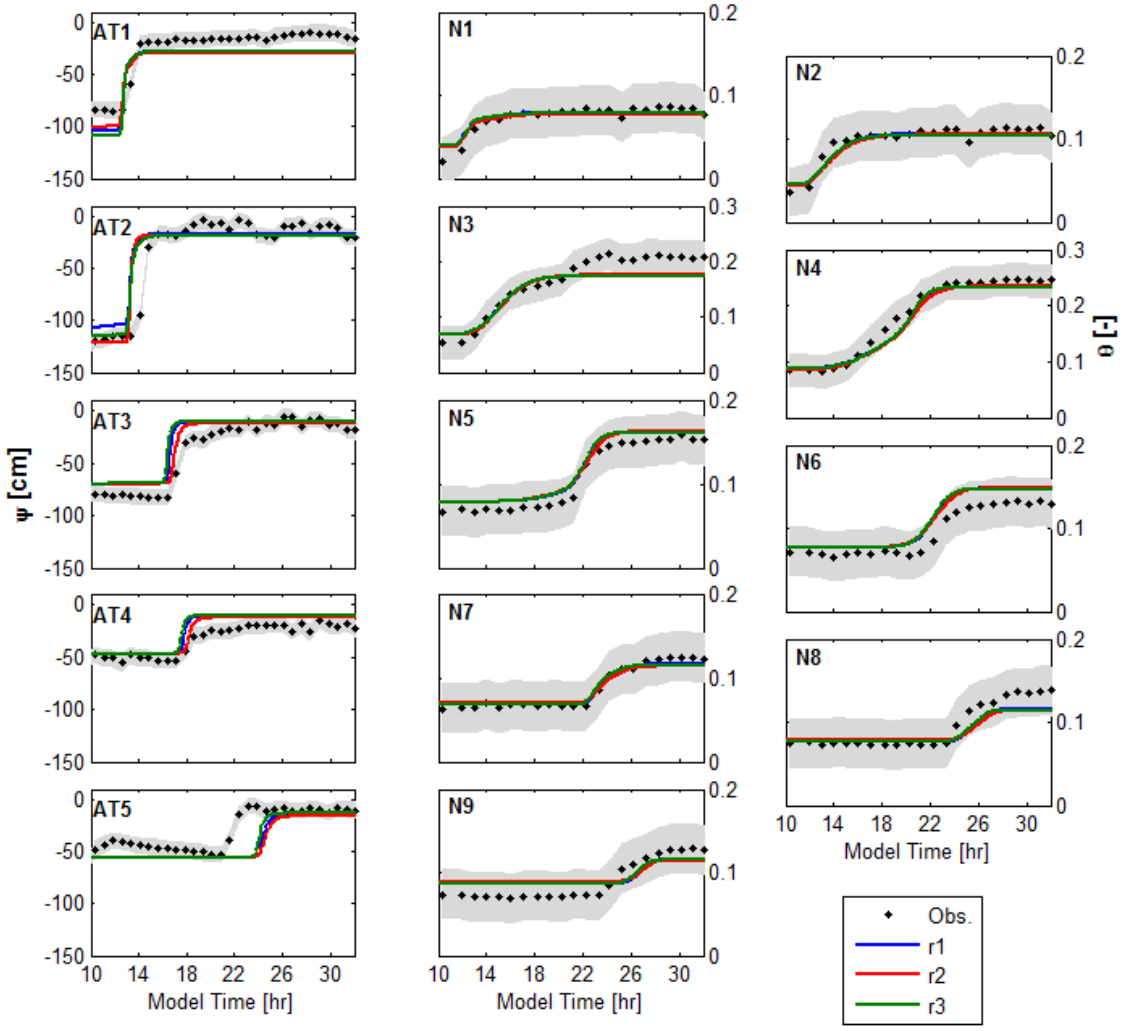

Figure 4-10: Observed and final predicted $\psi(t)$ and $\theta(t)$ data from runs r1 – r3 (note different y-axis for N3 and N4); shaded regions show ±1σ data error.

Table 4-2: Optimal material parameters from DSr minimization of NLL_θ.

	θ_S [-] [r1, r2, r3]	α [cm^{-1}] [r1, r2, r3]	n [-] [r1, r2, r3]	K_S [cm s^{-1}] [r1, r2, r3]
M1	[0.21, 0.24, 0.23]	[0.09, 0.07, 0.10]	[2.39, 2.65, 2.29]	[0.20, 0.27, 0.28]
M2	[0.10, 0.17, 0.10]	[0.38, 0.11, 0.50]	[1.77, 3.84, 1.21]	[0.23, 0.30, 0.038]
M3	[0.29, 0.29, 0.29]	[0.13, 0.08, 0.15]	[1.54, 1.71, 1.52]	[1.3, 0.5, 0.7]x10^{-3}
M4	[0.21, 0.20, 0.19]	[0.46, 0.35, 0.43]	[1.49, 1.47, 1.46]	[0.03, 0.025, 0.019]

Runs r4 – r6 had $NLL_{\Delta t}$ as the primary objective function but none of the runs were able to accurately predict Δt_{bndry} to within the the observed data error and final Δt_{bndry} errors were again between 2.6 and 3.7 ns (Figure 4-11). Run *r4*, which reduced $NLL_{\Delta t}$ to 11.0, not only underpredicted final Δt_{bndry} but also severely underfit $\psi(t)$ and $\theta(t)$ data (final NLL_{ψ} = 1002; final NLL_{θ} = 408). Of the three runs that minimzed $NLL_{\Delta t}$, only r5 did not result in drastically high NLL_{ψ} and NLL_{θ} values, but still r5 did not predict Δt_{bndry} with sufficient accuracy. Predicted $\theta(t)$ and $\psi(t)$ data from run r5 are shown later in Figure 4-12 and I do not show fits from runs r4 or r6 since they do not come close to the observed $\psi(t)$ or $\theta(t)$ data. Final parameter values for runs r4 – r6 are presented in Table 4-3 and are similar between runs for M3 and M4 but have higher disagreement for M1 and M2. Disagreement between these parameters is somewhat irrelevant since none of the parameter sets accurately predict the observed Δt_{bndry}.

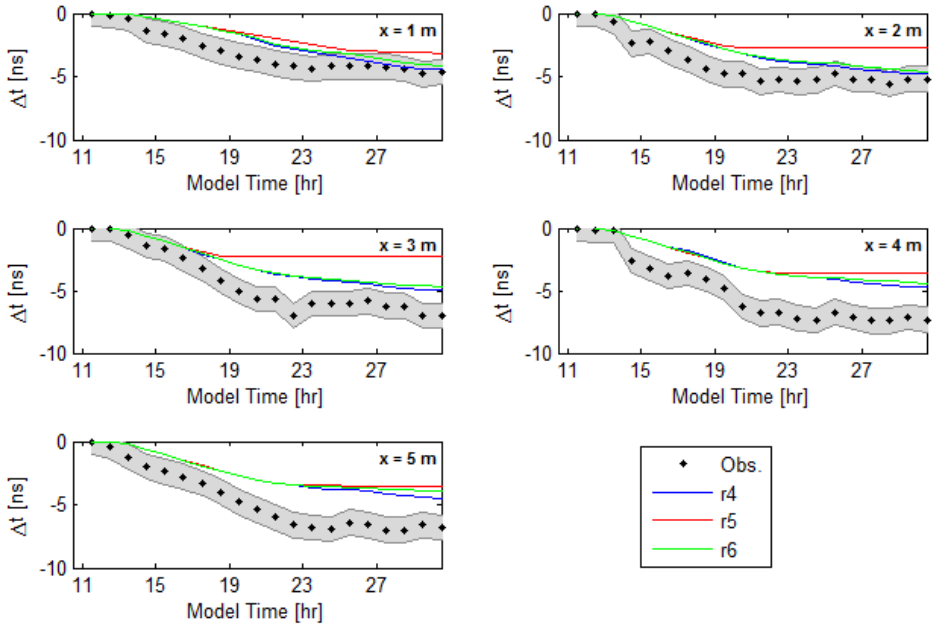

Figure 4-11: Observed and calculated Δt_{bndry} data from runs r4 – r6; shaded regions show ±1σ data error.

Table 4-3: Optimal material parameters from DSm minimization of $NLL_{\Delta t}$.

	θ_S [-] [r4, r5, r6]	α [cm^{-1}] [r4, r5, r6]	n [-] [r4, r5, r6]	K_S [cm s^{-1}] [r4, r5, r6]
M1	[0.22 0.34 0.28]	[0.10, 0.10, 0.12]	[1.91, 2.60, 2.02]	[0.019, 0.240, 0.080]
M2	[0.12, 0.17, 0.10]	[0.24, 0.11, 0.44]	[1.10, 3.78, 1.11]	[0.269, 0.273, 0.023]
M3	[0.26, 0.25, 0.27]	[0.14, 0.04, 0.10]	[1.84, 1.72, 1.87]	[0.4, 0.7, 0.4]x10^{-3}
M4	[0.17, 0.16, 0.16]	[0.43, 0.40, 0.40]	[1.52, 1.35, 1.10]	[0.054, 0.025, 0.026]

Runs r7 – r9 were set-up to minimize the misfit to all data and reduced ΣNLL by 43%, 27%, and 23%, respectively, but most of that came from reduction of NLL_{ψ} (reduced 58%, 38%, and 39%). Because of the negative correlation between NLL_{ψ} and NLL_{θ} observed from the DSm investigation discused above, each run led to an increase in NLL_{θ} of 4 – 8 %. Positive correlation between NLL_{ψ} and $NLL_{\Delta t}$ led to reduction in $NLL_{\Delta t}$ of 18%, 13%, and 2% for each run but, as discussed in the above paragraph, greater reduction of $NLL_{\Delta t}$ does not necessarily produce accurate fits to the observed Δt_{bndry} data. Final $\psi(t)$ and $\theta(t)$ data fits from runs r7 – r9 are shown in Figure 4-12 along with fits from run r5. Runs r7 – r9 fit $\psi(t)$ data much better than $\theta(t)$ data despite the unbalanced weighting applied in ΣNLL. In each of runs r7 – r9, as with the DSm results, accurate fits to $\psi(t)$ data lead to early prediction of t_{wf} for $\theta(t)$ data, particulary below 60 cm. Final parameter values for runs r7 – r9 are presented in Table 4-4 and are similar for M1, M3, and M4 between runs, and are also in the same range as parameters from runs r1 – r6.

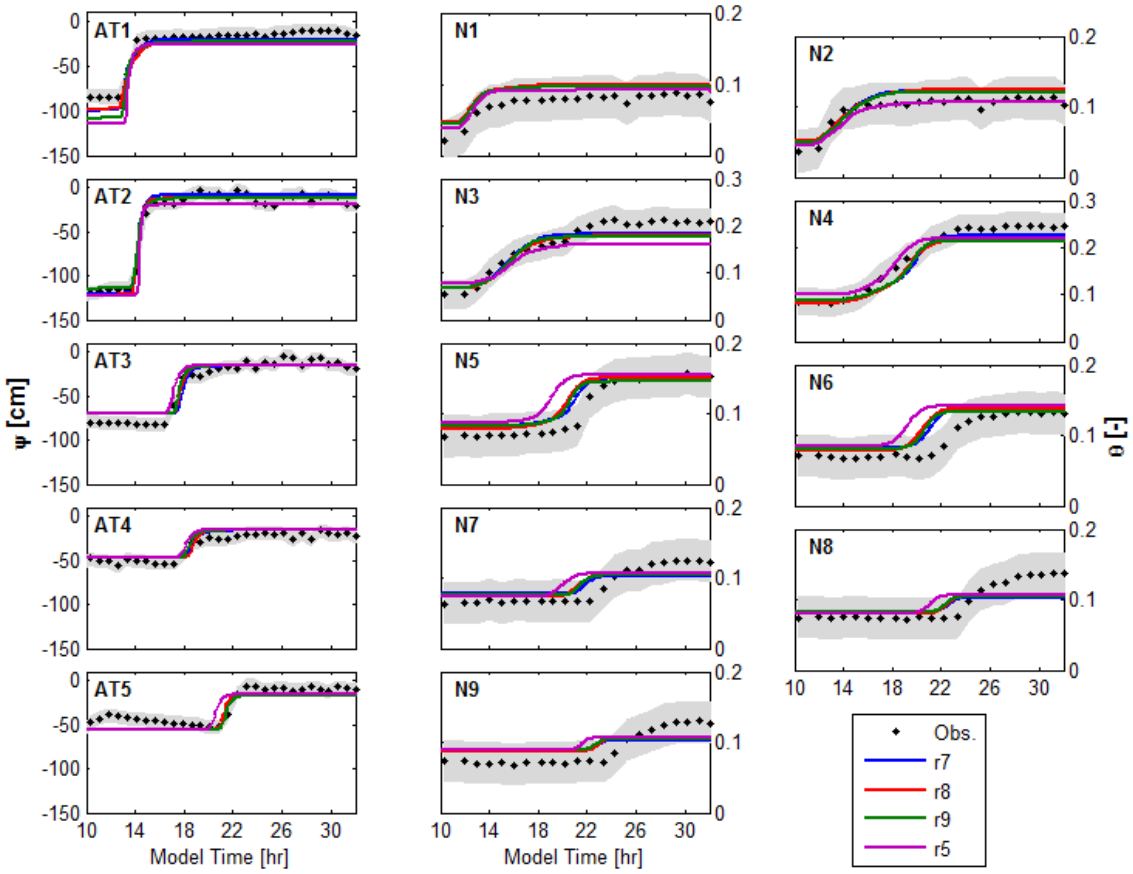

Figure 4-12: Observed and final predicted $\psi(t)$ and $\theta(t)$ data from runs r5 and r7 – r9 (note different y-axis for N3 and N4); shaded regions show ±1σ data error.

Table 4-4: Optimal material parameters from DSr minimization of Σ*NLL*.

	θ_S [-] [r7, r8, r9]	α [cm^{-1}] [r7, r8, r9]	n [-] [r7, r8, r9]	K_S [cm s^{-1}] [r7, r8, r9]
M1	[0.25, 0.32, 0.27]	[0.08, 0.08, 0.11]	[2.20, 2.29, 2.19]	[0.12, 0.26, 0.16]
M2	[0.13, 0.11, 0.12]	[0.46, 0.16, 0.48]	[2.45, 3.99, 1.35]	[0.22, 0.27, 0.019]
M3	[0.27, 0.25, 0.25]	[0.08, 0.06, 0.10]	[1.67, 1.82, 1.54]	[1.0, 1.2, 0.9]x10^{-3}
M4	[0.14, 0.16, 0.16]	[0.31, 0.43, 0.48]	[1.29, 1.35, 1.34]	[0.018, 0.026, 0.038]

Initial values of all parameters from the DSr inversion were within the range of n_2-constrained M1D distributions but minimum/maximum value bounds were taken from

the original MCMC bounds in Chapter 3 (see Table 3-2) to allow greater search of the parameter space. In Figure 4-13, I show the final DSr parameter values from runs r1 – r3 and r7 – r8 (runs r4 – r6 are excluded since they fail to fit any of the observed data) and optimal DSm values from sets that minimzed NLL_{ψ} and NLL_{θ} for each of the 16 parameters along with the minimum and maximum M1D values (i.e., range of final distributions calculated in Chapter 3). Each parameter is further separated by the objective function it minimized (i.e., NLL_{ψ}, NLL_{θ}, or ΣNLL). The distribution of these optimal parameters shows that final values for four of the 16 parameters (θ_{S2}, α_2, n_2, K_{S3}) are outside of the M1D distribution ranges, which negates the initial hypothesis that the M1D distributions can be used to accurately predict M2D data and implies that wider parameter distributions may be necessary to obtain proper fits to all M2D data. Figure 4-13 also shows the level of agreement between parameters when different objective functions are minimzed. Parameters such as θ_{S4}, α_1, n_3, n_4, K_{S1}, and K_{S4} have a narrow range despite fitting different data sets while α_2, α_3, n_2, and K_{S2} have much wider ranges for all objective functions and even between runs minimizing the same objective function.

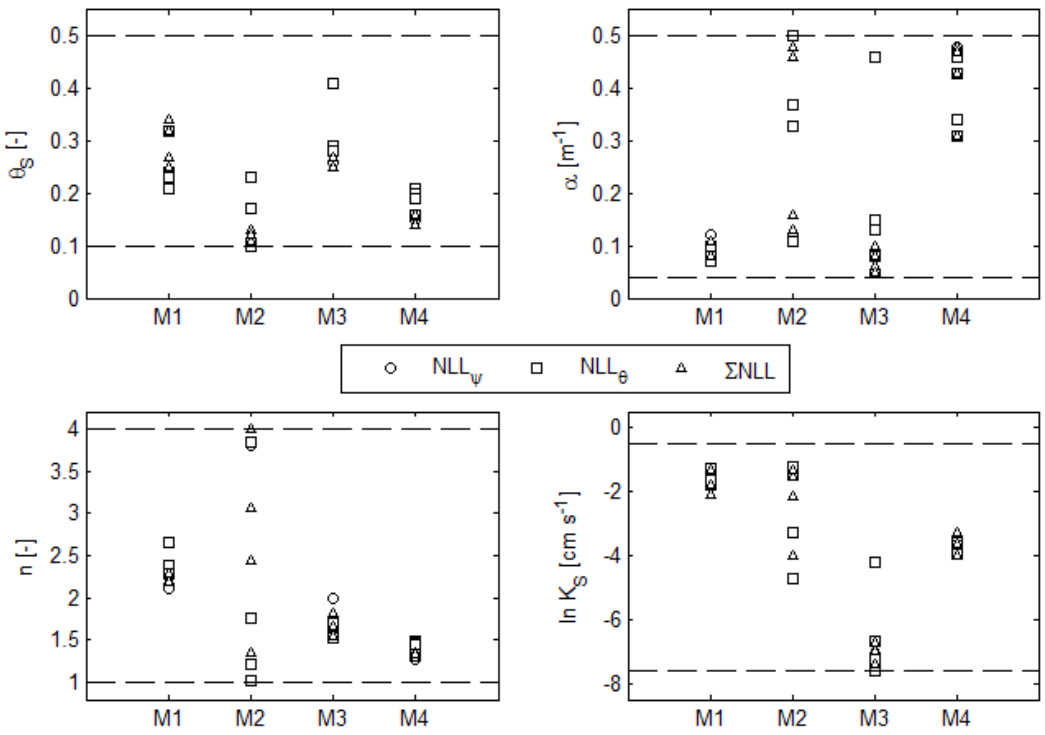

Figure 4-13: Optimal parameter values from DSm and DSr grouped by data set each minimized.

Four main conclusions can be drawn from the DSr optimization presented in this section that relate to the model's ability to predict the observed data. Each conclusion is described below and conclusions 3 and 4 are discussed in more detail in the following section as they relate to material heterogeneity and physical limitations of the model.

1) The model and optimization algorithms are struggling to find optimal parameters that fit the observed Δt_{bndry} data despite focusing on fitting those data exclusively, and parameters that come closest fail to fit $\psi(t)$ and $\theta(t)$ data. When taken with the error in manual calculation of Δt_{bndry}, this implies that there may be a fundemental error in the conceptual relationship between $\Delta\theta$ and Δt_{bndry} used in this method. I hypothesize that this error is the result of either uncertainty in θ distribution within the vadose zone (i.e., small-scale sand lenses or open pores that may be

holding high θ but not drastically affecting the flow of water) or improper use of the conceptual relationship between $\Delta\theta$ and Δt_{bndry} (i.e., CRIM equation may not be idealy suited for this relationship). Regardless, for the remainder of this study I focus only on fitting $\psi(t)$ and $\theta(t)$ data.

2) Optimal values of the M2D model are found that fit the observed $\theta(t)$ or $\psi(t)$ data (runs r1 – r3) within the associated error, but not all optimal parameter values are within the range of the M1D distributions. This implies that optimal values for $\theta(t)$ may not be within the range of optimal values for $\psi(t)$ found in the M1D model.

3) The model struggles to correctly match both $\psi(t)$ and $\theta(t)$ data simultaneously, particulary at AT4 and $\theta(t)$ depths below 60 cm. From comparison of Figure 4-10 and Figure 4-12, there appears to be a trade-off between fitting $\psi(t)$ and $\theta(t)$ data. When successful fits to the $\theta(t)$ data are achieved the model closely predicts $\psi(t)$ data in AT5 – AT9 but predicts later t_{wf} for AT4. When successful fits to $\psi(t)$ data are achieved, the model predicts early t_{wf} at $\theta(t)$ measurement depths below 60 cm. This depth is the approximate depth of the top of M3 and implies that the source of disagreement in t_{wf} is within M3.

4) Final parameter values found with runs r1 – r3 and r7 – r8 (which minimized NLL_θ and ΣNLL, respectively) are similar for materials M1, M3, and M4, which suggests that only small changes in parameters are necessary to fit $\psi(t)$ or $\theta(t)$ data.

5) Nearly all M2 parmeters show wide ranges for nearly all parameters from the nine different DSr inversions and, in some cases, cover nearly the full range of

parameter values. This supports the findings in Chapter 3 that the model is insensitive to M2 parameters. I suspect, as in Chapter 3, that this is related to the discontinuous distribution and lack of direct sampling in M2.

4.3.3 Comparison of $\theta(\psi)$ and $K(\psi)$ Functions

From comparison of parameter values in Figure 4-13 we see that some parameters occupy a narrow range (e.g., θ_{S4}, α_1, n_4, and K_{S1}), while others cover a wide range (e.g., α_2, n_2, and K_{S2}) for all three objective functions. This expresses the variability in model sensitivity to individual parameters. More importantly, I cannot identify any parameters that show clear distinction between value sets that minimize ΣNLL and those that minimize NLL_θ. This indicates that individual values that fit $\psi(t)$ data are not significantly different from values that fit $\theta(t)$ data, and this seems to confirm the DSm results that only minor changes in parameter values are necessary to fit either $\psi(t)$ or $\theta(t)$ data. Overall, the results from the previous section imply that the current four-material model is insufficent to fit both $\psi(t)$ and $\theta(t)$ data and the reason is not simply due to individual parameter values.

One of the conclusions in Chapter 3, as well as what was reached by *Stauffer and Lu* (2011), was that parameter values of the VGM functions are not as informative as the functions represented by those parameters (i.e., $\theta(\psi)$ and $K(\psi)$). This is primarily because unique relationships between individual parameters combine to produce specific $\theta(\psi)$ and $K(\psi)$ relationships. For each of the eight optimal parameter sets above (two from the DSm method and six from the DSr method), I used Equations 4-1 thru 4-4 to develop $\theta(\psi)$ and $K(\psi)$ curves for each of the four materials (assuming $\theta_R = 0.03$ and $l = 0.5$; see Chapter 2). In Figure 4-14 I show these curves classified by which objectve function the

curves optimized (either NLL_{ψ} or NLL_{θ}). The wide range of M2 parameter values produced large uncertainty in M2 curves and, as mentioned previously, implies insensitivity of the experiment and model to M2 material properties. Other material functions, however, show similar curve shapes from all parameter sets and only $\theta(\psi)$ in M4 and $K(\psi)$ in M3 appear to differ significantly between objective function sets. It is worth mentioning that comparison of Figure 4-14 to Figure 3-13 in Chapter 3 shows similar curve shapes predicted between the M2D and M1D models.

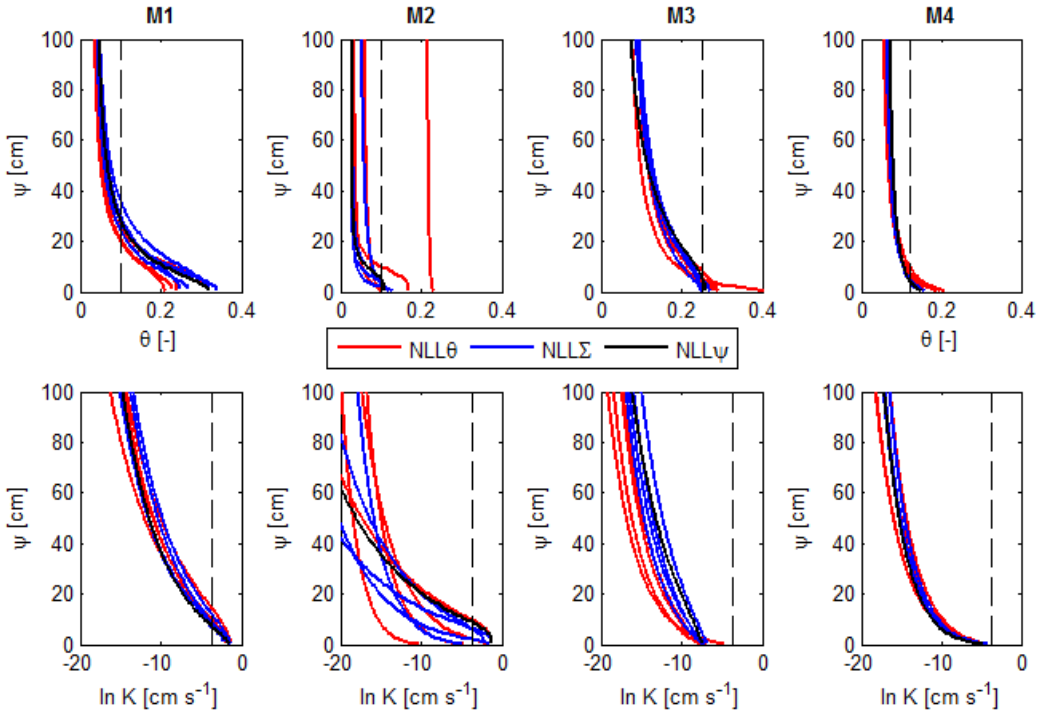

Figure 4-14: $\theta(\psi)$ and $K(\psi)$ relationships developed from optimal parameter values from the DSm and DSr methods for different objective function sets.

Divergence of $\theta(\psi)$ curves in M4 occurs only near saturation and beyond the maximum θ measured in M4 (maximum θ and K in each material are show in Figure 4-14). Because full saturation was not reached during the experiment, divergence at higher θ levels will not significantly influence percolation rates and moisture distribution as

much as curve shape below maximum θ, where curves from the different objective function sets agree.

Divergence of $K(\psi)$ in M3, however, is much more significant, especially when considering that $K(\psi)$ in Figure 4-14 is on a natural log scale. When NLL_θ is minimized, the model consistently predicts about an order-of-magnitude lower $K(\psi)$ than when NLL_ψ is minimized. The shift of the $K(\psi)$ curve has the effect of slowing percolation rates through M3 so that observed $\theta(t)$ data are correctly matched, but this also has the effect of slowing percolation rates at AT4, which is under approximately equal thickness of M3. Conversely, when fitting $\psi(t)$ data the model shifts $K(\psi)$ curves to produce faster percolation rates through M3 to fit $\psi(t)$ data, particularly in AT4, and this creates earlier t_{wf} at $\theta(t)$ measurement locations within and below M3. This shifting between higher and lower $K(\psi)$ curves is likely what is causing the model to struggle to fit both data sets simultaneously, and it would be better that material M3 be seperated into two materials between AT4 (TX5BD) and where $\theta(t)$ measurments are made (NX5B), which I do in the following section.

4.4 Five-Material Model

The results from the optimization and analysis above all point to the conclusion that there is sufficient heterogeneity within material layers, especially M3, such that a four-material model is not capable of reproducing the observed $\psi(t)$ and $\theta(t)$ data. Furthermore, from Figure 4-14 it appears that the most striking heterogeneity is within material M3 between AT4 and NX5BS. In the five-material model (M2D-5L) developed in this section, I separate material M3 into two materials (M3A and M3B) directly between TX5BD and NX5B (at x = 4.8 m from left model edge) and apply separate

parameter values of θ_S, α, n, and K_S to each sub-material (Figure 4-15). Initial parameter values for M3A (left-side material) were chosen from M3 values, which optimized ΣNLL (and also minimized NLL_ψ) in the DSr runs (run r6) and for M3B (right-side material) initial values were chosen from M3 of DSr run r1. For materials M1, M2, and M4, I used r1 values as well since they closely matched both $\psi(t)$ and $\theta(t)$ data.

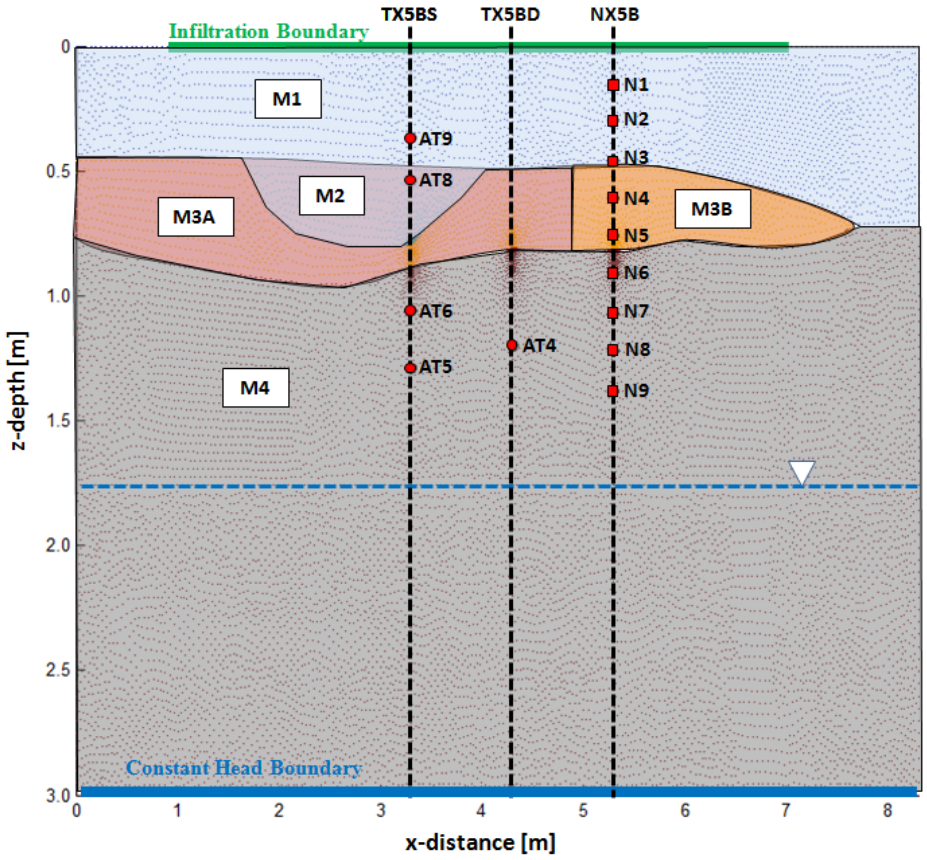

Figure 4-15: Material distribution of the M2D-5L model.

I then applied a final DSr optimization to the M2D-5L model by varying all 20 parameters and using the sum of weighted NLL_ψ and NLL_θ ($NLL_{\psi\theta} = w_\psi\, NLL_\psi + w_\theta\, NLL_\theta$ where $w_\psi = 1$ and $w_\theta = 3$) as the objective function to be minimized. After 300 runs, $NLL_{\psi\theta}$ reduced from 524 to 306 (41% reduction) and produced very good fits to both $\psi(t)$ and $\theta(t)$ data with $NLL_\psi = 171$ and $NLL_\theta = 45$. Final predicted $\psi(t)$ and $\theta(t)$ data from this

DSr run along with runs r1 and r8 (both from four-material model, for comparison) are shown in Figure 4-16, and final M2D-5L material parameters are presented in Table 4-5. As predicted above, it appears that significant difference in K_S between M3A and M3B was necessary to fit both $\psi(t)$ and $\theta(t)$ data simultaneously. The values presented in Table 4-5 represent the current optimal parameter values of the five materials of the M2D-5L model. Final optimization and uncertainty analysis of the M2D-5L model was achieved through LHS, as discussed in the next section.

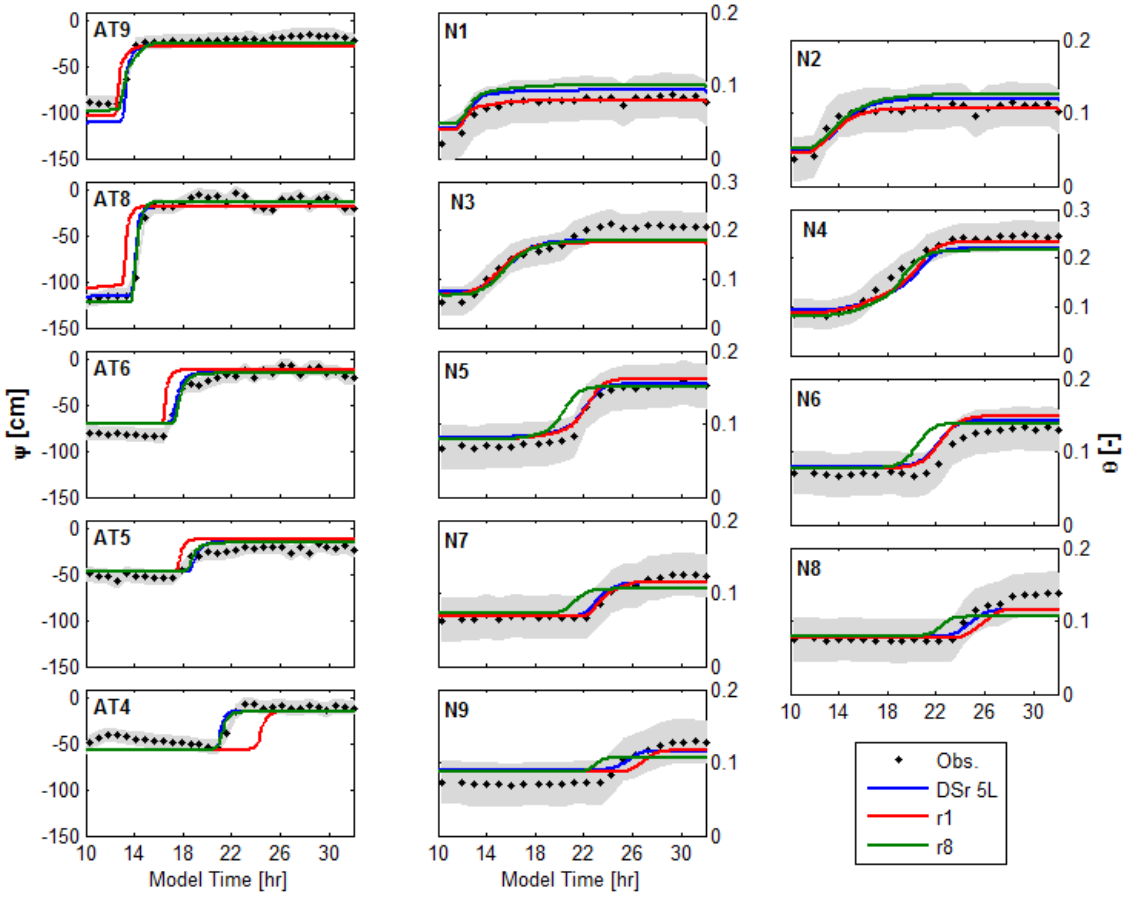

Figure 4-16: DSr optimal final fits to $\psi(t)$ and $\theta(t)$ data using the M2D-5L (five-material) model along with fits from r1 and r8 using the M2D (four-material) model (note different y-axis on N3 and N4); shaded regions show ±1σ data error.

Table 4-5: Optimal material parameters from DSr run of M2D-5L model.

	θ_S [-]	α [cm^{-1}]	n [-]	K_S [cm s^{-1}]
M1	0.28	0.10	2.41	0.162
M2	0.11	0.35	1.84	0.301
M3A	0.26	0.05	1.89	1.6×10^{-3}
M3B	0.27	0.14	1.48	1.3×10^{-3}
M4	0.21	0.35	1.50	0.032

4.4.1 Parameter Uncertainty of M2D-5L Model

The LHS method was developed to explore the parameter space of a model in an unbiased fashion and to ensure that each region of a parameter space is represented, regardless of its probability (*McKay et al.* 1979). The LHS method begins with discretizing the cumulative probability distributions of each parameter into a pre-determined number of bins, each with equal range of probability (p). The parameter values from each bin are then randomly mixed so that different combinations of probabilities are equally represented and each bin is sampled once and only once for each parameter (*Cheng and Druzdzel* 2000). I provide a brief example to illustrate this process below.

Consider two parameters each represented by a uniform distribution such that $0 < p(x_1) \leq 1$ and $0 < p(x_2) \leq 1$. First we divide each distribution into N bins and assign each bin a number 1:N where the number refers to the bin probability range of the cumulative distribution function (cdf) of x_1 or x_2. Figure 4-17 shows an example where $N = 5$. Next we permutate each parameter column to achieve a mixed sample set (Figure 4-17B). This ensures that parameters with mixed probabilities are represented in the final sample sets. Each row of the permutated matrix corresponds to a single parameter set used in a single model run.

$p(x_1,x_2)$	x_1	x_2
(0.2, 0.2)	1	1
(0.4, 0.4)	2	2
(0.6, 0.6)	3	3
(0.8, 0.8)	4	4
(1.0, 1.0)	5	5

A

$\Rightarrow$

$p(x_1, x_2)$	x_1	x_2
(0.2, 0.2)	1	1
(0.8, 0.4)	4	2
(0.4, 0.6)	2	3
(1.0, 0.8)	5	4
(0.6, 1.0)	3	5

B

Figure 4-17: Example of LHS with two parameters and *N* = 5; A) original set, B) after permutation.

The success of LHS to represent the entire parameter space with a relatively small number of samples (much smaller than full grid search methods require) lies in the value of *N*. When *N* is low (as in Figure 4-18A), there are gaps in the parameter space and ranges of parameter values that are unrepresented. As *N* is increased, each individual parameter set is still not used but zones of the full parameter space are more represented (Figures 4-18B – 4-18C). As *N* is increased indefinitely, the corresponding range between samples eventually diminishes to values below the sensitivity of the model.

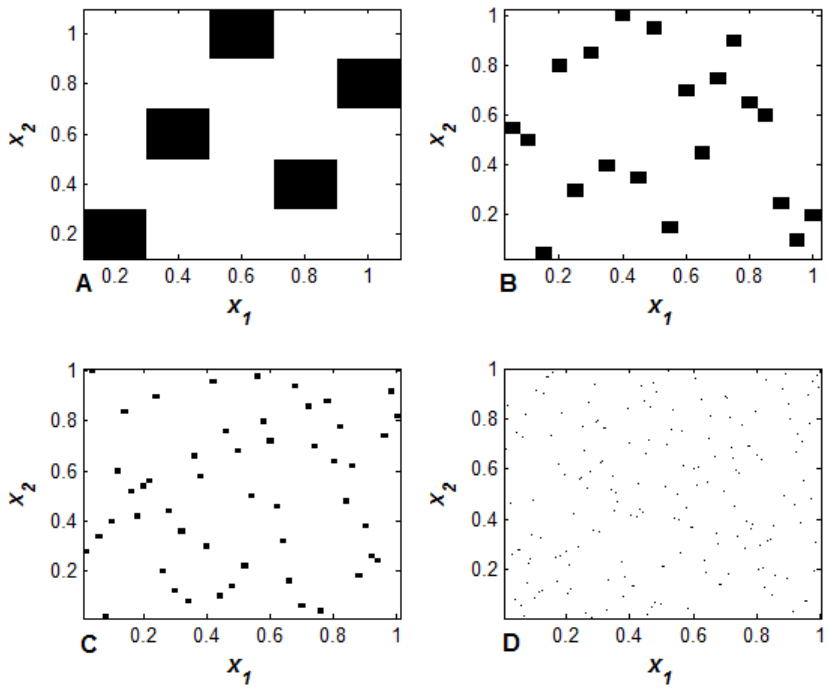

Figure 4-18: Examples of LHS matrix with different values of *N*: A) *N* = 5, B) *N* = 20, C) *N* = 50, D) *N* = 200.

For the M2D-5L model with five materials and four parameters per material (20 total parameters), a full grid search would require *N* to the power of 20 individual model runs. Even using a value as small as *N* = 5 would require ~$1x10^{14}$ individual model runs. By using LHS we can greatly reduce the number of model runs while still exploring the parameter space and mixed-probability parameter sets. The value of *N* is often chosen by a trade-off between run time and accurate representation of the parameter space. For the LHS of the M2D-5L model I chose *N* = 10000 which, at 4 – 7 min runtime per model, would require >34 d to complete. However, total runtime was reduced to < 5 days through the use of parallel processing.

Selection of the a priori sampling distribution (i.e., cdf(*x*)) is critical to the success of LHS. If it is too narrow, large portions of the parameter space will be under-sampled and optimal zones may be completely overlooked. If the distribution is too broad, the

value of N required to get a well-discretized parameter space would be proportionately large. Based on the results of the DSr optimization of the M2D model along with the final parameter values from the DSr optimization of the M2D-5L model, it is likely that optimal parameter values that accurately fit the observed data are near the final M2D-5L values presented in Table 4-5. I therefore limit our a priori distributions to be within normal distributions of θ_S, α, and n, and $\ln K_S$ for each material with mean (μ) equal to Table 4-5 values and standard deviation (σ) equal to 15% of mean values.

In Figure 4-19, I show the final LHS distributions of NLL_ψ, NLL_θ, and $NLL_{\psi\theta}$ and see that there is significant range of each NLL value despite only a σ = 15% range in parameter sampling distributions (σ = 139, 303, and 930 for NLL_ψ, NLL_θ, and $NLL_{\psi\theta}$, respectively). We see there is also very strong correlation between NLL_θ and $NLL_{\psi\theta}$ (R^2 = 0.98) implying that $NLL_{\psi\theta}$ is more sensitive to NLL_θ than NLL_ψ. This may be due to higher data error in $\theta(t)$ than $\psi(t)$, or weighting NLL_θ too heavily. Minimum values of NLL_ψ, NLL_θ, and $NLL_{\psi\theta}$ were 130, 43, and 332, respectively.

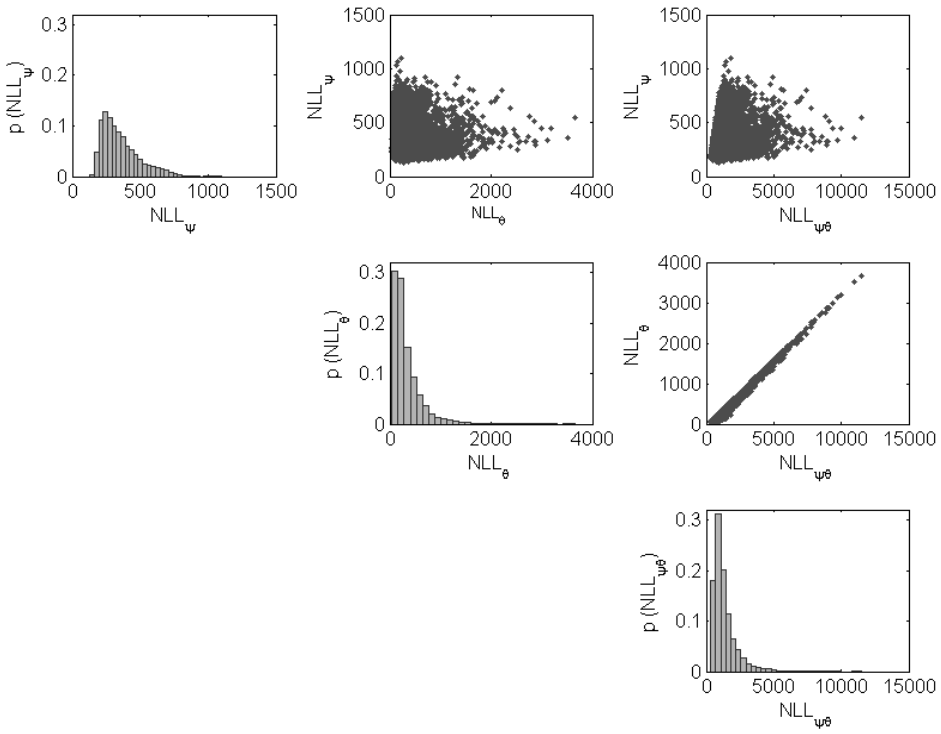

Figure 4-19: Distributions of NLL_{ψ}, NLL_{θ}, and $NLL_{\psi\theta}$ from the LHS of M2D-5L model.

To estimate uncertainty in final parameters, I calculated σ for each parameter from the set that included all LHS runs where $NLL_{\psi\theta}$ was within 150 % of the minimum value (i.e., where $NLL_{\psi\theta} < 499$, which included 292 samples). I will refer to this as the S150 set. Mean and σ values from the S150 set are presented in Table 4-6 and fits to $\psi(t)$ and $\theta(t)$ data from the set from S150 that produced the lowest $NLL_{\psi\theta}$ values (best-fitting set), the highest $NLL_{\psi\theta}$ value (worst-fitting set), and the optimal set from the direct search (Table 4-5), are shown together in Figure 4-20.

Table 4-6: Mean and σ (italic) values from LHS S150 sets.

	θ_S [-]	α [cm^{-1}]	n [-]	K_S [cm s^{-1}]
M1	0.284 *0.0287*	0.101 *0.0126*	2.496 *0.2698*	0.163 *0.0406*
M2	0.109 *0.0167*	0.355 *0.051*	1.892 *0.2291*	0.303 *0.0536*
M3A	0.262 *0.038*	0.046 *0.0065*	1.904 *0.2607*	$2.7\text{x}10^{-3}$ *0.0022*
M3B	0.281 *0.0329*	0.136 *0.0191*	1.534 *0.1124*	$1.7\text{x}10^{-3}$ *0.0011*
M4	0.209 *0.0246*	0.349 *0.0531*	1.537 *0.1073*	0.0359 *0.0186*

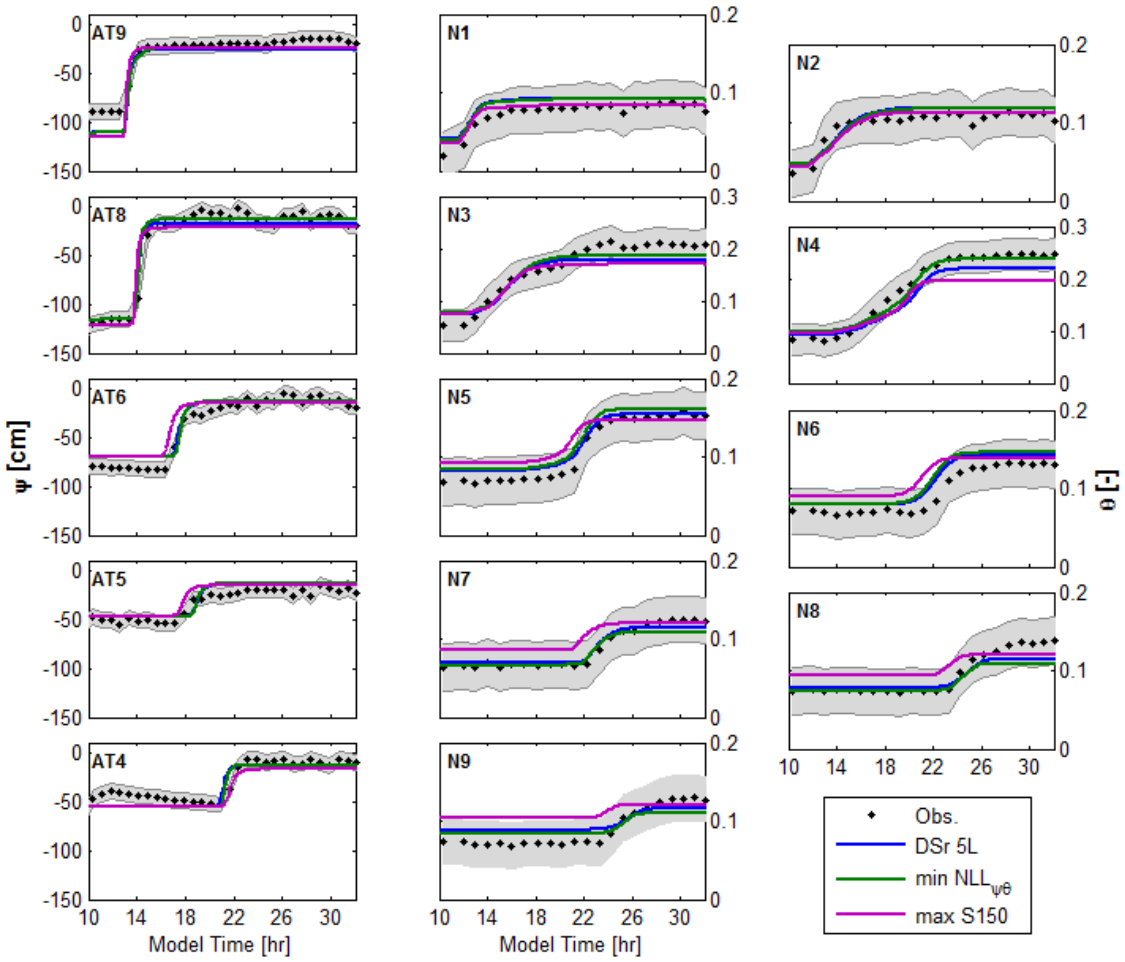

Figure 4-20: Fits to $\psi(t)$ and $\theta(t)$ data from selected LHS S150 sets and final DSr set of the M2D-5L model (note different y-axis on N3 and N4); shaded regions show $\pm 1\sigma$ data error.

Analysis of the LHS results implies that the optimal values from the DSr optimization of the M2D-5L model are from a very narrow, local minumum (narrow since *NLL* values increase rapidly outside of this minimum). Uncertainty of these optimal parameters can be estimated from the normalized standard deviation values (σ/μ), which are presented in Table 4-7 for θ_S, α, n and ln K_S for all materials. Calculation of σ/μ was not used in Chapter 3 but I use the final distributions from that chapter (Table 3-3) to calculate it, and I present it in Table 4-7 for comparison. With the additional complexity of the 2D model and using both the $\theta(t)$ and $\psi(t)$ data. we see that the M2D-5L model

considerably reduced the uncertainty (up to 36 %) in individual parameter values from the M1D model in Chapter 3.

Table 4-7: Estimated normalized standard deviation from the S150 sets and the final M1D distributions in Chapter 3.

M2D-5L σ/μ [%]					**M1D σ/μ [%]**				
	θ_S	α	n	K_S		θ_S	α	n	K_S
M1	10.1	12.5	10.8	13.2	**M1**	22.4	28.2	10.1	40.3
M2	15.2	14.4	12.1	14.4	**M2**	41.8	49.7	46.9	28.5
M3A	14.5	14.3	13.7	11.9	**M3**	13.7	50.6	7.8	11.3
M3B	11.7	14.1	7.3	8.4					
M4	11.8	15.2	7.0	13.6	**M4**	9.6	32.0	5.9	17.5

4.5 Discussion

4.5.1 Uncertainty in Δt_{bndry} Model

The failure of the M2D model to fit Δt_{bndry} data (despite focusing directly on minimizing $NLL_{\Delta t}$) together with the overall poor fit to the observed data imply there may be error in: (a) the conceptual understanding of the system; (b) the mathematical formulation of it (i.e., Equations 4-6 through 4-10); and/or (c) correctly picking the reflection from the GPR data. Conceptually, it is well established that changes in θ produce lower v_{EM} and increases in travel-time. The model certainly predicts this behavior but the overall observed Δt_{bndry} is not being achieved. The mathematical formulation (Equation 4-10) is a simple derivative of the CRIM equation (Equation 4-9) and the values of c and ε_w are very well established. The value of d_{M4} was based on GPR data collected during the infiltration test after steady-state had been reached. The high θ at this time produced the clearest image and best estimates of material depths. The depth estimates were also confirmed by core samples in TX5BS and TX5BD but may contain some error (likely < 10 %).

Likely the largest sources of uncertainty in the Δt_{bndry} data are in shifting the raw GPR data to the air wave arrival and picking the arrival time of the material reflection. Correction of the air wave is necessary to account for changes between the record time (time the GPR receiver antenna begin recording) and the pulse time (time when the transmitting antenna releases the electromagnetic pulse). When the top layer of the soil is very dry and the transmitter and receiver are close together, there may only be a small difference between the arrival times of the air wave and ground wave and it may be difficult to accurately pick the air wave. The raw GPR data show very good resolution of material layers in the initial profile (see Figure 4-4A) and better resolution at later times (see Figure 4-4D), but at times within a few hours of the start of infiltration there is considerable noise in the GPR profile data. The noise is likely caused by scattering due to differential wetting near the surface (finger flow). This noise leads to uncertainty in picking the material reflection in the first few profiles when the majority of Δt_{bndry} occurs (first few hours of data in Figure 4-5). Overall, great care was taken in picking the air wave and reflections from the raw data but this is currently the most likely source of error in the observed Δt_{bndry} data.

4.5.2 LHS Results

The LHS method was used to estimate uncertainty in final parameter values for the M2D-5L model because it provides a robust and relatively quick estimate of uncertainty surrounding mean parameter values. Metropolis-Hastings methods (similar to what was used in Chapter 3) would likely produce a better estimate of uncertainty and be more appropriate for comparison of the Chapter 4 results to the Chapter 3 results. However, this was not practical given the run time of the M2D-5L model. The M1D

model required 3 – 6 s to complete a forward model run and10^6 model runs could be achieved in a realistic amount of time (the overall run time was significantly reduced due to out-of-bound values). The M2D-5L model, however, required 4 – 7 min to complete a forward run so a similar Metropolis-Hastings type optimization was not practical. A detailed comparison of the uncertainty between the M1D model and M2D-5L model might best be achieved by having the same analysis methods applied to both models, but the results at the end of this chapter still provide a substantial, and practical, comparison.

In the preceding section I state that the LHS requires an a priori distribution within which to search. The provided distributions used in this chapter were normally distributed about the M2D-5L DSr results (providing the mean values) with σ = 15 % of those values. Some of the values presented in Table 4-7 are very close to 15 % (e.g., θ_{S2}) which implies that the distribution of values within the S150 sets has an equal width to the a priori distribution. This suggests that the LHS results may be underestimating the actual uncertainty for some parameters because the search distributions are constrained by the a priori distributions (i.e., the sampling range is smaller than what may actually fit the data). Several of the normalized σ values, however, are considerably < 15 % and greatly reduced from the M1D values, implying an overall improved uncertainty in the M2D-5L model.

4.6 Conclusions

In this chapter, I extended the four-material 1D model described in Chapter 3 to a four-material 2D model that incorporated the observed heterogeneity from GPR data, and ultimately to a five-material 2D model that included additional heterogeneity identified from parameter optimization. I also introduced a method using reflection travel-time data

from GPR profiles to estimate changes in θ. Using direct-search optimization methods. I estimated final VGM parameter values for the five-material model that accurately fit $\psi(t)$ and $\theta(t)$ data. I then used LHS to estimate parameter uncertainty (σ/μ), which was < 15 % for all parameters and signficantly reduced from results in Chapter 3. Optimal parameters could not be identified that successfully fit GPR reflection travel-time data.

This chapter concludes that incorporation of lateral variability in material thickness and hydraulic properties is necessary to accurately fit $\psi(t)$ and $\theta(t)$ data sets simultaneously and reduce parameter uncertainty. Additionally, this chapter shows that small changes in material parameters of < 20 % (i.e., changes that may be within the range of accepted parameter error) can lead to significant differences in $\theta(\psi)$ and $K(\psi)$ relationships. Under the particular conditions presented in this study, which cover the likely range of field θ for realistic infiltration rates in coarse conglomeratic soils, such differences in $\theta(\psi)$ and $K(\psi)$ functions can lead to considerable changes in predicted unsaturated flow rates.

CHAPTER 5: SUMMARY AND FUTURE WORK

5.1 Summary

The work presented in this dissertation was used to determine whether unsaturated flow relationships, specifically van Genuchten-Mualem relationships (VGM), can be applied to coarse, conglomeratic material without alteration and, if so, to estimate the range of VGM parameters for such materials. VGM relationships are well established for fine-grained sediment ($d < 2$ mm) but have seldom been applied directly to coarse material ($d > 2$ mm) or to conglomeratic sediment because measurement of unsaturated flow properties in these materials is difficult and the nature of unsaturated flow in coarse, conglomeratic material, specifically the effect of large cobbles, is not well understood.

Chapter 2 presented a brief overview of the BHRS in order to establish it as a natural, well-studied research site. Chapter 2 provided important information about installation and instrument calibration for measurements made in the vadose zone at the BHRS. It also showed seasonal trends in θ and ψ data and aquifer responses to natural precipitation (which highlights the high-conductivity nature of the BHRS material).

Chapter 3 described the details of the infiltration test including how preliminary data were used to identify structure, estimate initial material properties, and aid in test design. It presented $\theta(t)$ and $\psi(t)$ observations along with the design of a 1D model to fit $\psi(t)$ and partial $\theta(t)$ responses at different measurement depths and within different material layers. The purpose of the 1D model was to establish the appropriateness of

VGM relationships for describing unsaturated flow in layered, coarse, conglomeratic material and to provide an initial estimate of parameter distributions and uncertainty.

Chapter 4 extended the 1D modeling in Chapter 3 to a 2D model that incorporated observed lateral variations in material thickness. The purpose of the 2D modeling was to reduce uncertainty in VGM parameter values by increasing the level of complexity (by including both lateral flow and lateral heterogeneity in material thickness and properties) and constrain the VGM relationships by including the full $\psi(t)$ and $\theta(t)$ data sets in parameter optimization. Parameter optimization with the 2D model identified additional heterogeneity in one of the model materials between $\psi(t)$ and $\theta(t)$ measurement locations. A five-material, 2D model was then developed and used to fit the full $\psi(t)$ and $\theta(t)$ data sets, predict final VGM parameter values, and estimate parameter uncertainty (σ/μ), which was reduced up to 36 % from 1D model results. Chapter 4 also presented a method whereby travel-time data from GPR data are used to track changes in θ, but the results suggest substantial error in picking GPR reflections such that the method was unsuccessful with the current data.

The results of this project show that the VGM relationships can be applied directly to coarse, conglomeratic sediment and can accurately predict flow at low saturation (i.e., saturation levels likely experienced under natural conditions including high-intensity rain events). The direct application of VGM relationships implies that the same processes that control unsaturated flow in fine-grained sediment control flow in coarse sediment as well, and that the coarse gravel/cobble sized particles do not significantly inhibit unsaturated flow, at least at low saturation in such sediments with negligible silt or clay fractions. This may be counter-intuitive since most reasearch on

saturated flow in stony sediment concludes that cobbles increase tortuosity, and thus reduce conductivity but I theorize that, at low saturation, there is already high tortuosity caused by water forced to travel along thin films around soil grains, and the increased tortuosity caused by large cobbles is insignificant. That is, at low saturation, the hydraulic conductivity of the bulk sediment is dominated by the inter-cobble material. However, this theory was developed from the results of one test, in one type of material only and the effects/results may be different in materials with different inter-cobble material (i.e., with more silt or clay).

There are very few published values of VGM parameters for coarse material and even fewer that are based on in situ measurements. To my knowledge, this work is some of the first research that shows that typical $\theta(\psi)$ and $K(\psi)$ functions can be applied to coarse, conglomeratic sediment and presents some of the first measured values of in situ VGM parameters for this type of sediment. The advancements made in this dissertation can be applied to a host of hydrological situations where quantifying moisture flow and distribution in coarse sediment needs to be addressed. Such include, but are not limited to, issues with precipitation seepage in mine waste or cover material, estimating infiltration and drainage capacity of gravel roadbeds, modeling heat flow by advection in conglomeratic material (e.g., climate change impacts on glacial outwash or permafrost; ecohydrology applications), and remediation efforts at contaminated sites (e.g., Hanford Site in central Washington).

5.2 Future Work

Below I present examples where future work could advance the understanding of unsaturated flow in coarse, conglomeratic soil by building on the work presented in the preceding chapters.

Chapters 3 and 4 established that the VGM relationships (and likely similar relationships) that were developed for fine-grained soils can be successfully used to predict unsaturated flow in coarse, conglomeratic soil without correction or treatment of the fine-grained material separate from the bulk material. The overall implication of this is that cobbles do not significantly alter unsaturated flow, and that the relatively fine-grained material (inter-cobble matrix) is the primary influence on unsaturated flow properties. This hypothesis could be easily tested by estimating VGM parameters for the fine-grained matrix of a similar conglomeratic sediment and comparing the values to what is presented in Chapters 3 and 4, or what is estimated from the in situ material sample. Parameters α and n have the most control over $\theta(\psi)$ and $K(\psi)$ at low saturation levels (i.e., levels experienced during the test presented in Chapter 3) and should provide the most insight into this hypothesis.

This project only looked at one type of conglomeratic material, which was composed of coarse sand with gravel and cobble sized particles. I concluded that the cobbles do not significantly influence unsaturated flow under natural conditions because hydraulic conductivity is high enough in the inter-cobble matrix to support flow at the low-saturation levels. In finer-grained, conglomeratic sediment (i.e., sediment of a high fraction of silt or clay with gravel and cobbles), where conductivity is lower in the inter-cobble matrix, there may be a greater influence of the cobbles. The type of experiment

presented in Chapter 3 (or similar in situ experiments) could be applied to different sediments to develop a more thorough understanding of cobble influences over the full range of constituent grain size, from silt/clay to coarse sand.

Estimation of the VGM relationships was achieved using θ_S, α, n, and K_S as fitting parameters and I excluded θ_R and l. θ_R was excluded because previous studies, as well as my own sensitivity analysis, indicated the models were far less sensitive to this parameter than others. Additionally, the dry initial state of the infiltration test volume provided confident a priori estimates of θ_R. Parameter l was excluded because most studies on unsaturated flow consider it to have a constant value of 0.5 (*Simunek et al.* 2005). In the VGM relationships, l represents the tortuosity index and influences only the $K(\psi)$ relationship. Several studies that investigated the influence of cobbles in sediment infer that the cobbles act primarily to influence tortuosity (e.g., *Mehuys et al.* 1975; *Bouwer and Rice* 1984). Additionally, since the decision to move from a four-material to a five-material model in Chapter 4 was based on the shape of the $K(\psi)$ curve, it would be valuable to establish what role l plays in this or other experiments on coarse soil and whether a constant value of 0.5 is appropriate for coarse, conglomeratic sediment (without an appreciable silt or clay fraction) as it is for fine-grained sediment. Along these same lines, it would also be valuable to test other θ-ψ-K constitutive relationships (e.g., *Brooks and Corey* 1964) to see which parameters of those relationships have the greatest influence.

The high conductivity nature of coarse sediments in general, and BHRS material specifically, result in a well-drained vadose zone. In Chapter 3 I highlighted the rapid movement of infiltration through the vadose zone, and in Chapter 2 I showed examples of

natural precipitation producing measurable rises in the water table across the research site. The selection of precipitation rate for the infiltration test was limited to rates that would not saturate the fine-medium sand layer and thus would allow continuous flow through the full sediment sequence. However, the rate used was similar to high-intensity storms of the Boise area but the duration was significantly greater than such storms. During the test there was substantial wetting in the fine-medium sand layer but $\Delta\theta$ in other materials was only 6 – 15%, which is only approximately half of the full saturation. This implies that the model is only sensitive to the shape of VGM curves near the low-saturation, high tension range, and not sensitive to the full curve (see $\theta(\psi)$ relationship for M1 in Figure 3-13). This interpretation means that I can only realistically establish that the VGM functions apply to coarse, conglomeratic sediment at low saturation levels. Future efforts should be focused on making θ and ψ measurements at high saturation levels. This may be difficult with in situ tests due the high conductivity nature of these types of material, but may be reached through laboratory tests or high resolution measurements made during sediment drainage, such as during rapid drops in the water table caused by either natural conditions (e.g., changes in river stage) or artificial forcing (e.g., pumping). Unsaturated flow measurements at high saturation can be used to further constrain the shapes of $\theta(\psi)$ and $K(\psi)$ curves and will likely further reduce parameter uncertainty, specifically parameters that control the curves near high saturation (i.e., θ_S and K_S). Constraining the full $\theta(\psi)$ and $K(\psi)$ curves will likely improve models and aid in investigations involving water table elevation changes, inundation studies with overbank flooding, and canal or pond leakage.

A few additional areas where future work could be beneficial, which I will list here but not go into detail, include: making θ and ψ measurements in closer proximity so that $\theta(\psi)$ relationships can be established directly; performing a similar test in a homogeneous soil profile (i.e., one material type) in order to reduce uncertainty; making repeated measurements in the same material under identical conditions, but at different spatial locations, to establish the level and effect of heterogeneity within a single coarse sediment layer (i.e., effect of cobble distribution); and identifying and correcting the error in the GPR data so that Δt_{bndry} data can be used to constrain the 2D θ distribution. These provide only a few examples of future work but numerous other experiments could be derived from the work presented in this dissertation.

REFERENCES

Abbasi, F., D. Jacques, J. Simunek, J. Feyen, and M. T. van Genuchten. 2003. Inverse estimation of soil hydraulic and transport parameters from transient field experiments: Heterogeneous soil. Transactions of the ASEA 46(4): 1097–1111.

Aishlin, P., M. Thoma, and W. Barrash. in prep. Installation, maintenance, and offset calculation for tensiometers at the Boise Hydrogeophysical Research Site. CGISS Technical Report 13-02. Boise State University, Boise, ID.

Barrash, W., and E. Reboulet. 2004. Significance of porosity for stratigraphy and textural composition in subsurface coarse fluvial deposits, Boise Hydrogeophysical Resreach Site. Geological Society of America Bulletin 116: 1059–1073.

Barrash, W., and M. Cardiff. 2013. Hydraulic conductivity distribution from multi-level slug tests and multivariate facies associations in a conglomeratic fluvial aquifer, Boise Hydrogeophysical Research Site. CGISS Technical Report 13-03. Boise State University, Boise, ID. 71p.

Barrash, W., and T. Clemo. 2002. Hierarchical geostatistics and multifacies systems: Boise Hydrogeophysical Research Site, Boise, Idaho. Water Resources Research 38: 1196. doi: 10.1029/2002WR001436.

Barrash, W., T. Clemo, and M. Knoll. 1999. Boise Hydrogeophysical Research Site (BHRS): Objectives, design, initial geostatistical results: Proceeding of SAGEEP99. The Symposium on the Application of Geophysics to Engineering and Environmental Problems. March 14-18, 1999. Oakland, CA. 389–398.

Barrash, W., T. Clemo, J. J. Fox, and T.C. Johnson. 2006. Field, laboratory, and modeling investigation of the skin effect at wells with slotted casing, Boise Hydrogeophysical Research Site. Journal of Hydrology 326: 181–198.

Bouwer, H., and R. Rice. 1984. Hydraulic properties of stoney vadose zones. Ground Water 22: 696–705.

Bradford, J. 2008. Measuring water content heterogeneity using multi-fold GPR with reflection tomography. Vadose Zone Journal 7: 184–193. doi: 10.2136/vzj2006.0160.

Bradford, J., W. Clement, and W. Barrash. 2009. Estimating porosity with ground-penetrating radar reflection tomography: A controlled 3-D experiment at the

Boise Hydrogeophysical Research Site. Water Resources Research 45: W00D26, doi: 10.1029/2008WR006960.

Brooks, R. H., and A. T. Corey. 1964. Hydraulic properties of porous media. Hydrology Papers, Colorado State University, Ft. Collins. 27p.

Cardiff, M., W. Barrash, M. Thoma, and B. Malama. 2011. Information content of slug tests for estimating hydraulic properties in realistic, high-conductivity aquifer scenarios. Journal of Hydrology 403: 66–82.

Cardiff, M., W. Barrash, and P. Kitanidis. 2012. A field proof-of-concept of aquifer imaging using 3D transient hydraulic tomography with modular, temporarily-emplaced equipment. Water Resources Research 48: W05531, doi:10.1029/2011WR011704.

Carsel, R. F., and R. S. Parrish. 1988. Developing joint probability distributions of soil water retention characteristics. Water Resources Research 24: 755–769. doi:10.1029/WR024i005p00755.

Cassel, D., and A. Klute. 1986. Water Potential: Tensiometry, in Methods of Soil Analysis, Part 1. Physical and Mineralogical Methods. American Society of Agronomy 563–596. Madison, WI.

Cerda, A. 2001. Effects of rock fragment cover on soil infiltration, interrill runoff and erosion. European Journal of Soil Science 52: 59–68.

Cheng, J., and M. J. Druzdzel. 2000. Latin hypercube sampling in Bayesian networks. Proceedings of the 13th International Florida Artificial Intelligence Research Society Conference. May 22-24, 2000. pp 287–292.

Clement, W., and W. Barrash. 2006. Crosshole radar tomography in a fluvial aquifer near Boise, ID. Journal of Environmental and Engineering Geophysics 11: 171–184.

Clement, W., W. Barrash, and M. Knoll. 2006. Reflectivity modeling of a ground-penetrating-radar profile of a saturated fluvial formation. Geophysics 71: K59-K66.

Corwin, D., K. Loague, and T. Ellsworth. 1999. Assesment of Non-Point Source Pollution in the Vadose Zone. American Geophysical Union, Washington, DC.

Cousin, I., B. Nicoullaud, and C. Coutadeur. 2003. Influence of rock fragments on the water retention and water percolation in a calcareous soil. Catena 53: 97–114.

Dafflon, B., J. Irving, and W. Barrash. 2011. Inversion of multiple intersecting high-resolution crosshole GPR profiles for hydrological characterization at the Boise Hydrogeophysical Research Site. Journal of Applied Geophysics 73: 305–314.

Dann, R., M. Close, M. Flintoft, R. Hector, H. Barlow, S. Thomas, and G. Francis. 2009. Characterization and estimation of hydraulic properties in an alluvial gravel vadose zone. Vadose Zone Journal 8: 651–663.

Dingman, S. L. 2002. Physical Hydrology. Waveland Press. Long Grove, IL. 646p.

Dunn, A., and G. Mehuys. 1982. Relationship between gravel content of soils and saturated hydraulic conductivity in laboratory tests. pp. 55–63. In Nichols, J., P. Brown, and W. Grant (ed.). Erosion and Productivity of Soils Containing Rock Fragments. Soil Science Society of America, Madison, WI.

Edwards, W., P. Germann, L. Owens, and C. Amerman. 1984. Watershed studies of factors influencing infiltration, runoff, and erosion on stony and non-stony soils. pp. 45–54. In Nichols, J., P. Brown, and W. Grant (ed.). Erosion and Productivity of Soils Containing Rock Fragments. Soil Science Society of America, Madison, WI.

Evett, S. R., J. A. Tolk, and T. A. Howell. 2003. A depth control stand for improved accuracy with the neutron probe. Vadose Zone Journal 2: 642–649.

Gardner, W. R. 1958. Some steady state solutions of the unsaturated moisture flow equation with application to evaporation from a water table. Soil Sciences 85: 228–232.

Gelman, A., and D. B. Rubin. 1992. Inference from iterative simulation using multiple sequences. Statistical Science 7: 457–472.

Hendrickx, J., A. Khan, M. Bannink, D. Birch, and C. Kidd. 1991. Numerical analysis of groundwater recharge through stony soils using limited data. Journal of Hydrology 127: 173–192.

Hubbell, J., and J. Sisson. 1998. Advanced tensiometer for shallow or deep soil-water potential measurements. Soil Science 163: 271–277.

Inoue, M., J. Simunek, J. W. Hopmans, and V. Clausnitzer. 1998. In situ estimation of soil hydraulic functions using a multistep soil-water extraction technique. Water Resources Research 34(5): 1035–1050.

International Atomic Energy Agency (IAEA). 1970. Neutron moisture gauges. Technical Report No. 112. IAEA, Vienna.

Johnson, B. 2011. Evapotranspiration in the riparian zone of the lower Boise River with implications for groundwater flow. M.S. Thesis. Boise State University, 74 p.

Johnson, B., B. Malama, W. Barrash, and A. N. Flores. 2013a. Recognizing and modeling variable drawdown due to evapotranspiration in a semiarid riparian zone considering local differences in vegetation and distance from a river source.

Water Resources Research 49(2): 1030–1039. http://dx.doi.org/10.1002/wrcr.20122.

Johnson, B., M. Thoma, and W. Barrash. 2013b. Neutron probe installation, calibration, and data treatment at the BHRS. CGISS Technical Report 13-01. Boise State University, Boise, ID. 28p.

Jol, H. M. 2009. Ground Penetrating Radar: Theory and Applications. Elsevier Science. Amsterdam. 544p.

Kelleners, T. J., D. G. Chandler, J. P. McNamara, M. M. Gribb., and M. S. Seyfried. 2010. Modeling runoff generation in a small snow-dominated mountainous catchment. Vadose Zone Journal 9: 517–527.

Kosugi, K. 1994. Three-parameter lognormal distribution model for soil water retention. Water Resources Research 30: 891–901.

Laloy, E., M. Weynants, C. L. Bielders, M. Vanclooster, and M. Javaux. 2010. How efficient are one-dimensional models to reproduce the hydrodynamic behavior of structured soils subjected to multi-step outflow experiments? Journal of Hydrology 393: 37–52.

Lapalla, E. G., R. W. Healy, and E. P. Weeks. 1987. Documentation of computer program VS2D to solve the equations of fluid flow in variable saturated media. USGS Water-Resources Investigations Report 83-4009. Denver, CO. 131p.

Leij, F. J., W. J. Alves, M. T. van Genuchten, and J. R. Williams. 1996. Unsaturated soil hydraulic database. UNSODA 1.0 user's manual. Report EPA/600/R-96/095. U. S. EPA, Ada, OK.

Liu, X., M. A. Cardiff, and P. K. Kitanidis. 2010. Parameter estimation in nonlinear environmental problems. Stoch. Environ. Res. Risk Assess. 24: 1003–1022.

Lunt, I. A., J. S. Bridge, and R. S. Tye. 2004. A quantitative, three-dimensional deposition model of gravelly braided rivers. Sedimentology 51: 377–414.

Ma, D., M. Shao, J. Zhang, and Q. Wang. 2010. Validation of an analytical method for determining soil hydraulic properties of stony soils using experimental data. Geoderma 159: 262–269.

Malama, B., and B. Johnson. 2010. Analytical modeling of saturated zone head response to evapotranspiration and river stage fluctuations. Journal of Hydrology 382: 1–9.

Malama, B., W. Barrash, M. Cardiff, M. Thoma, and K. Kuhlman. 2011. Modeling slug tests in unconfined aquifers taking into account water table kinematics, wellbore skin, and inertial effects. Journal of Hydrology 408: 113–126.

McKay, M. D., R. J. Beckman, and W. J. Conover. 1979. A comparison of three methods for selecting values of input variable in the analysis of output from a computer code. Technometrics 21(2): 239–245.

McNamara, J. P., D. Chandler, M. Seyfried, and S. Achet. 2005. Soil moisture states, lateral flow, and streamflow generation in a semi-arid, snowmelt-driven catchment. Hydrological Processes 19: 4023–4038.

Mehuys, G., L. Stolzy, J. Letey, and L. Weeks. 1975. Effects of stones on the hydraulic conductivity of reatively dry desert soils. Soil Sci. Soc. of Am. Journal 39: 37–42.

Milczarek, M. A., D. Zyl, S. Peng, and R. Rice. 2006. Saturated and unsaturated hydraulic properties characterization at mine facilities: Are we doing it right? Int. Conf. on Acid Rock Drainage. American Society of Mining and Reclamation, Lexington, KY. pp. 1273–1286.

Miller, F. and R. Guthrie. 1984. Classification and distribution of soils containing rock fragments in the United States. pp. 1–6. In Nichols, J., P. Brown, and W. Grant (ed.). Erosion and Productivity of Soils Containing Rock Fragments. Soil Science Society of America, Madison, WI.

Moret, G., M. Knoll, W. Barrash, and W. Clement. 2006. Investigating the stratigraphy of an alluvial aquifer using crosswell seismic traveltime tomography. Geophysics 71: 863–873.

Mualem, Y. 1976. A new model for predicting the hydraulic conductivity of unsaturated porous media. Water Resources Research 12: 513–522.

Mwenifumbo, C., W. Barrash, and M. Knoll. 2009. Capacitive conductivity logging and electrical stratigraphy in a high-resistivity aquifer, Boise Hydrogeophysical Research Site. Geophysics 74: E125-E133.

Nelson, G. K. 2007. Deterministic modeling of bromide tracer transport during the tracer/time-lapse radar imaging test at the Boise Hydrogeophysical Research Site, August 2001. M.S. Thesis, Boise State University. Boise, ID.

Oostrom, M., T. W. Wietsma, J. H. Dane, M. J. Truex, and A. L. Ward. 2009. Desiccation of unsaturated porous media: Intermediate-scale experiments and numerical simulation. Vadose Zone Journal 8: 643–605.

Oostrom, M., G. D. Tartakovsky, T. W. Wietsma, M. J. Truex, and J. H. Dane. 2011. Determination of water saturation in relatively dry porous media using gas-phase tracer tests. Vadose Zone Journal 10: 634–641.

Peck, A., and J. Watson. 1979. Hydraulic conductivity and flow in non-uniform soil. In Workshop on Soil Physics and Field Heterogeneity, CSIRO Division of Environmental Mechanics. Canberra, Australia.

Rawls, W., D. Brakensiek, and K. Saxton. 1982. Estimation of soil water properties. Transactions of the ASAE 25: 1316–1320.

Reboulet, E. C., and W. Barrash. 2003. Core, grain size, and porosity data from the BHRS. CGISS Technical Report 03-02. Boise State University, Boise, ID.

Richards, L. A. 1931. Capillary conduction of liquids through porous mediums. Physics 1: 318–333.

Ritter, A., F. Hupet, R. Muñoz-Carpena, S. Lambot, and M. Vanclooster. 2003. Using inverse methods for estimating soil hydraulic properties from field data as an alternative to direct methods. Agricultural Water Management 59: 77–96.

Rosetta Neural Network Prediction Module. 1999. United States Department of Agriculture – Agricultural Research Service. http://www.ars.usda.gov/Services/docs.htm?docid=8953.

Sauer, T., and S. Logsdon. 2002. Hydraulic and physical properties of stony soils in a small watershed. Soil Sci. Soc. of Am. Journal 66: 1947–1956.

Scharnagl, B., J. A. Vrugt, H. Vereecken, and M. Herbst. 2011. Inverse modeling of in situ soil water dynamics: investigating the effect of different prior distributions of the soil hydraulic parameters. Hydrology and Earth Systems Sciences 15: 3043–3059.

Selker, J. S., C. K. Keller, and J. T. McCord. 1999. Vadose Zone Processes. Lewis Publishers. Boca Ratton, FL. 337p.

Simunek J., R. Angulo-Jaramillo, M. G. Schaap, J-P. Vandervaere, and M. T. van Genuchten. 1998. Using an inverse method to estimate the hydraulic properties of crusted soils from tension-disc infiltrometer data. Geoderma 86: 61–81.

Simunek, J., M. Senja, and M. T. van Genuchten. 1999. The HYDRUS-2D software packages for simulating two-dimensional movement of water, heat, and multiple solutes in variably-saturated media, version 2.0. U.S. Salinity Laboratory, USDA, ARS, Riverside, CA. 225p.

Simunek, J., M. T. van Genuchten, and M. Sejna. 2005. The HYDRUS-1D software package for simulating the one-dimensional movement of water, heat, and multiple solutes in variably-saturated media. Department of Environmental Sciences, University of California Riverside, Riverside, CA. 296p.

Sisson, J., G. Gee, J. Hubbell, W. Bratton, J. Ritter, A. Ward, and T. G. Caldwell. 2002. Advances in tensiometry for long-term monitoring of soil water pressures. Vadose Zone Journal 1: 310–315.

Slater, L., A. Binley, W. Barrash, J. Keery, J. Montrey, and M. Cardiff. 2011. An investigation of the ability of induced polarization to resolve aquifer heterogeneity in an unconsolidated sedimentary aquifer. Abstract, SAGEEP. Charleston, SC.

Smith, T. J., J. P. McNamara, A. N. Flores, M. M. Gribb, P. S. Aishlin, and S. G. Benner. 2011. Small soil storage capacity limits benefit of winter snowpack to upland vegetation. Hydrological Processes 25: 3858–3865.

Stauffer, P. H., and A. Lu. 2012. Quantifying transport uncertainty in unsaturated rock using Monte-Carlo sampling of retention curves. Vadose Zone Journal 11. doi: 10.2136/vzj2011.0171.

Straface, S., F. Chidichimo, M. Rizzo, W. Barrash, A. Revil, M. Cardiff, and A. Guadagini. 2011. Joint inversion of steady-state hydrologic and self-potential data for 3D hydraulic conductivity distribution at the Boise Hydrogeophysical Research Site. Journal of Hydrology 407: 115–128. doi: 10.1016/jhydrol.2011.07.013.

Tarantola, A. 2005. Inverse Problem Theory and Methods for Model Parameter Estimation. Society of Industrial and Applied Mathematics, Philadelphia, PA.

Tetegan, M., B. Nicoullaud, D. Baize, A. Bouthier, and I. Cousin. 2011. The contribution of rock fragments to the available water content of stony soils: Proposition of new pedotransfer functions. Geoderm 165: 40–49.

Thoma, M., and W. Barrash. 2012. Discharge-stage and discharge-inundation relationships for the Boise River at the Boise Hydrogeophysical Research Site. CGISS Technical Report 12-03. Boise State University, Boise, ID. 22p.

Thoma, M., W. Barrash, and J. H. Bradford. in prep. Quantifying flux across an inundated aquifer boundary in response to seasonal flooding at an intermediate-scale river-aquifer system. to be submitted to Journal of Hydrology.

Thoma, M., W. Barrash, M. Cardiff, J. H. Bradford, and J. Mead. in press. Estimation of in situ unsaturated hydraulic functions of a coarse stony sediment sequence from a field-scale infiltration experiment, Boise Hydrogeophysical Research Site. Vadose Zone Journal.

Thoma, M. J., J. P. McNamara, M. M. Gribb, and S. G. Benner. 2011. Seasonal recharge components in an urban/agricultural mountain front aquifer system using noble gas thermometry. Journal of Hydrology 409: 118–127. doi:10.1016/j.jhydrol.2011.08.003.

Tokunaga, T., K. Olson, and J. Wan. 2003. Moisture characteristics of Hanford gravels: bulk, grain-surface, and intragranular components. Vadose Zone Journal 2: 322–329.

van Genuchten, M. T. 1980. A closed form equation for predicting the hydraulic conductivity of unsaturated soils. Soil Sci. Soc. Am. Journal 44: 892–898.

Vrugt, J. A., and W. Bouten. 2002. Validity of first-order approximations to describe parameter uncertainty in soil hydrologic models. Soil Sci. Soc. of Am. Journal 66: 1740–1751.

Vrugt, J. A., W. Bouten, H. V. Gupta, and J. W. Hopmans. 2003a. Toward improved identifiability of soil hydraulic parameters: on the selection of a suitable parametric model. Vadose Zone Journal 2: 98–113.

Vrugt, J. S., H. V. Gupta, W. Bouten, and S. Sorooshian. 2003b. A shuffled complex evolution metropolis algorithm for optimization and uncertainty assessment of hydrologic model parameters. Water Resources Research 39, doi: 10.1029/2002WR001642.

Wohling T., and J. A. Vrugt. 2008. Combining multiobjective optimization and Bayesian model averaging to calibrate forecast ensembles of soil hydraulic models. Water Resources Research 44, doi: 10.1029/2008WR007154.

Wohling, T., and J. A. Vrugt. 2011. Multiresponse multilayer vadose zone model calibration using Markov chain Monte Carlo simulation and field water retention data. Water Resources Research 47: W04510, doi: 10.1029/2010WR009265.

Zhang, L., and Q. Chen. 2005. Predicting bimodal soil-water characteristic curves. Journal of Geotechnical and Geoenvironmental Engineering 133: 666–670.

Zhang, Z. F., A. L. Ward, and J. M. Keller. 2011. Determining the porosity and saturated hydraulic conductivity of binary mixtures. Vadose Zone Journal 10: 313–321.

Zou, Z., M. Young, and P. Wierenga. 2001. Estimation of depth averaged unsaturated soil hydraulic properties from infiltration experiments. Journal of Hydrology 242: 26–42.